DEVELOPMENT OF AN ADAPTIVE
FLAP/FLAPERON FLIGHT CONTROL SYSTEM
WITH SHAPE MEMORY ALLOY ACTUATION

BY

C2010
Thomas Sinn

Submitted to the graduate degree program in Aerospace Engineering
and the Graduate Faculty of the University of Kansas
in partial fulfillment of the requirements for the degree of
Master's of Science.

_____
Dr. Ronald M Barrett-Gonzalez,
Associate Professor of Aerospace Engineering
(Chairperson)

_____
Dr. Mark Stephan Ewing,
Associate Professor and
Chairman of Aerospace Engineering
(Committee Member)

_____
Dr. Ray Taghavi,
Professor of Aerospace Engineering
(Committee Member)

Date defended: _____

The Thesis Committee for Thomas Sinn certifies
that this is the approved Version of the following thesis:

DEVELOPMENT OF AN ADAPTIVE
FLAP/FLAPERON FLIGHT CONTROL SYSTEM
WITH SHAPE MEMORY ALLOY ACTUATION

Committee:

_____
Dr. Ronald M Barrett-Gonzalez,
Associate Professor of Aerospace Engineering
(Chairperson)

_____
Dr. Mark Stephan Ewing,
Associate Professor and
Chairman of Aerospace Engineering
(Committee Member)

_____
Dr. Ray Taghavi,
Professor of Aerospace Engineering
(Committee Member)

Date approved: _____

Abstract:

This thesis discusses the design, manufacturing and testing of a new kind of adaptive airfoil using Shape Memory Alloy (SMA) actuation. An antagonistic arrangement of SMA wires was used in a Post-Buckled Precompressed (PBP) kind of actuator that was employed in an adaptive flap system. The thesis opens with a short survey on the history of the PBP mechanism and a literature research on different flap systems actuated by adaptive materials. The conceptual design of the SMAPBP actuator and its evolution to the actuator employed in an adaptive aerostructure is discussed in the first chapters. Experiments showed that the SMAPBP actuator could obtain tip rotations up to 65°, which nearly quadrupled the levels achieved by piezoelectric PBP actuators. In the following, former developed theory for piezoelectric PBP actuators was modified to account for the trapezoidal shape of the SMAPBP actuator. The developed theory was then compared to experimental results. A FEM model was also developed and evaluated to prove the PBP concept for this actuator numerically. In the second section of the thesis the author gives a detailed explanation of the design concept and the manufacturing of the airfoil. A NACA0012 airfoil with a chord length of 150mm and a width of 100mm was used to prove the concept of the adaptive flap system. The thesis continues with a description of the test setup, the CFD model assumptions and the results of wind tunnel tests. The developed adaptive airfoil proved its capabilities during the numerical and experimental tests and showed that the employment and actuation of the SMAPBP actuator could more than doubled the lift coefficient of the airfoil. The architecture and employment of a closed loop position feedback system to overcome the nonlinear behavior of the SMA material and the PBP mechanism is also discussed. The thesis closes with an overview over the adaptive airfoil with SMAPBP actuator and gives recommendations for future work in this field.

Table of Contents Page#

List of Figures

Page#

List of Tables

List of Symbols

English Symbols	Definition	Units
[A]	Extensional Stiffness Matrix	N/m
[B]	Bending-Extension Stiffness Matrix	N
b_1	Width of Actuator at Root	m
b_2	Width of Actuator at Tip	m
b	Width of Actuator	m
b_s	Width of Actuator at any given s	m
b_ξ	Width of Actuator at any given ξ	m
c_a	Chord Length of Airfoil	m
c	Integrating Factor	-
C_l	Lift Coefficient	-
C_d	Drag Coefficient	-
C_p	Pressure Coefficient	-
D	Drag	N
[D]	Bending Stiffness Matrix	Nm
d_{SMA}	Diameter of SMA wire	m
E	Modulus of Elasticity	N/mm^2
F_a	Axial Buckling Force on Actuator	N
$F_{actuation}$	Force Developed by SMA Actuation	N
F_{Flap}	Force on Flap Area	N
F_{Tip}	Tip Force of Actuator	N
$F_{tip\ max}$	Maximum Force Acting at Actuator Tip due to Lift	N
$F_{TrailingEdge}$	Force at Trailing Edge	N
h_{displ}	Actuator Tip Displacement	m

I	Current	A
I	Moment of Inertia	$1/mm^4$
I_{out}	Output Current of Current Amplifier	A
L	Lift	N
L	Length of Actuator	m
M	Moment Acting on Lamina (CLPT)	Nm
N	Force Acting on Lamina (CLPT)	N
P_{cr}	Critical Buckling Load	N
P_t	Absolute/Operating Pressure	Pa
R	Imaginary Radius for Actuated Actuator	m
$R_1 - R_4$	Resistors/Strain Gages in Wheatstone Bridge	Ω
s	Control Variable along Curved Length of Actuator	m
S_G	Gage Factor of Strain Gage	-
t	Thickness of Actuator	m
t_a	Maximum Thickness as a Fraction of the Chord	-
T_t	Absolute/Operating Temperature	K
U	Voltage	V
U_{in}	Input Voltage of Wheatstone Bridge	V
U_{in}	Input Voltage of Current Amplifier	V
U_s	Voltage across Wheatstone Bridge	V
$v_{freestream}$	Fresstream / Air Speed Velocity	m/s
x	Deformation in x-direction	m
x_1	Horizontal Displacement Length 1	m
x_2	Horizontal Displacement Length 2	m
x_a	Position along the Chord of Airfoil from 0 to c_a	m
y	Deformation in y-direction	m

y_1	Vertical Displacement Length 1	m
y_2	Vertical Displacement Length 2	m
y_a	Half Thickness of Airfoil at a given value of x_a	m
z	Thickness of Laminate	m

Greek Symbols	**Definition**	**Units**
α	Angle of Attack	deg
δ	Actuator Tip Rotation Angle	deg
ε	Strain	m/m
η	Energy Efficiency	-
κ	Curvature of Actuator/Laminate	1/m
Λ	Strain Introduced from Adaptive Material	m/m
ν	Poisson's Ratio	-
ξ	Integrating Variable	rad
ρ_{air}	Air Density	kg/m^3
σ	Stress	N/mm^2

Acronyms

CAP	Conventionally Attached Piezoelectric
CFD	Computational Fluid Dynamics
CLPT	Classical Lamination Plate Theory
COTS	Commercial off the Shelf
DAQ	Data Acquisition System
DARPA	Defense Advanced Research Program Agency
DoD	United States Department of Defense

FEM	Finite Element Method
GPS	Global Positioning System
MIT	Massachusetts Institute of Technology
MUAV	Miniature/Micro Unmanned Aerial Vehicle
NACA	National Advisory Committee for Aeronautics
NASA	National Aeronautics and Space Administration
NGC	Northrop Grumman Corporation
NiTi	Nickel-Titanium Alloy
PBP	Post-Buckled Precompressed
PMN	Lead Magnesium Niobate (ceramic electrostrictor)
PVDF	Polyvinylideneflouride (polymer piezoelectric film)
PZT	Lead Zirconate Titanium (common piezoelectric material)
SMA	Shape Memory Alloy
SMAPBP	Shape Memory Alloy Post-Buckled Precompressed
SSL	Standard Sea Level
UAV	Unmanned Aerial Vehicle
UCAV	Uninhabited Combat Air Vehicle
USAF	United States Air Force
USB	Universal Serial Bus
VTOL	Vertical Take-Off and Landing

1 Introduction

The definition of the word adapt is given by the Oxford English Dictionary as "**verb 1** make suitable for a new use or purpose. **2** become adjusted to new conditions."[1] This states that an adaptive material or adaptive structure consists of a 'system' that can adjust itself to new conditions in order to perform better. Therefore, the development of adaptive systems began with the first self-replicating structures 3.8 Billion years ago. The first self-replicating structures were the first organisms that replicated and adapt themselves to environmental conditions. The first scientific discovery made on the field of adaptive materials from human kind was the discovery of the piezoelectric effect in Rochelle salt from Pierre & Jacques Curie in 1880.[2] With the ongoing research in the area of piezoelectricity in Germany and France, Voigt publishes "Lehrbuch der Kristallphysik"[3] in 1910, defining piezoelectric properties. Early in the 20th century, the development of quartz crystals for the use in oscillators and radios made the military and commercial world aware of the possibilities within these new kinds of materials. With the development of the NiTinol family of shape memory alloys from W.J. Buehler and R. Wiley at the Naval Ordinance Laboratory in 1961, a new kind of adaptive material with unique properties was discovered.[4] The employment of this new material could be envisioned in heat engines, relays, fuses, expansion plugs, space structures and many more. Shape memory alloys have the characteristic to remember a given shape. By applying heat to the material it can transform back into its original or trained shape as a function of temperature.

The application of adaptive materials in aerospace structures seems to be perfect because of their low weight and part count compared to conventional aerospace structures. Due to the fact that several different flight regimes occur during a typical aircraft flight, setting a single wing configuration to optimize the aerodynamic performance of the wing at any circumstance is nearly impossible. A common design strategy today is to identify a couple of dominant

flight regimes and design the wing according to these maximum circumstances. Flight control surfaces like ailerons, flaps and equilibrators are making the wing somehow adaptive to certain flight conditions like take off, cruising and landing. These control surfaces are normally designated to a specific part of the wing so that their actuation results in sharp form changes and therefore an increased structural weight.[5] The use of smart materials can simplify the complexity of the system compared to conservative technologies such as electromechanical or hydraulic actuators. Conventional control surface deployment mechanisms introduce more drag because of the inevitability of gaps and outstanding edges. Adaptive material like piezoelectric materials, shape memory alloys (SMAs) and electro active materials were applied into aerospace vehicles for more than 20 years into various kinds of structures and surfaces. Regardless of certification problems for commercial aircraft, smart materials give unique possibilities in Unmanned Arial Vehicle (UAV) purposes and opens new doors in design and performance areas. There are various different adaptive materials that can change their mechanical, thermal, optical, chemical, electrical or magnetic appearance. This thesis is centered on adaptive materials that can change their mechanical characteristics (stiffness, strain or damping for example). Commercially available mechanical adaptive materials are piezoceramic (e.g. PZT G-1195), piezo film (e.g. PVDF), electrostrictor (e.g. PMN), magnetostrictor (e.g. Terfenol DZ) and shape memory alloy (e.g. Nitinol) materials.[6] Piezoceramics and piezo film use the piezoelectric effect. To actuate the piezoelectric material, an applied electric field forces monopoles in the piezoelectric material into a desired direction and deforms the material therefore. Electostrictors are ceramics that expand in the presence of an electric field by a coupling effect between the applied electric field and the electric dipole of the material. Magnestostrictors work in a similar manner as electrostrictors but they are actuated by a magnetic field instead. The last material in the list of adaptive material is Shape Memory Alloys (SMA). Shape memory alloys are used in various fields today such as medical devices, actuators, composites and structures.

SMA materials are metallic alloys that can undergo martensitic transformations when subjected to applied thermo-mechanical loads.[7] The alloys are capable of recovering plastic strains when heated up above a certain temperature.[8-9] Other behaviors of SMA that must be considered for the proposed wing design are one-way shape memory effect, two way shape memory effect and material training.[10-11] SMAs can be activated by external heating (ambient temperature) or electrical heating (Joule heating with electrical current). Shape memory alloys seem very attractive for actuation purposes because of their large excitation forces and displacements.

1.1 Previous Work

1.1.1 Adaptive Materials and Actuators

The introduction of laminated materials simplified the incorporation of active elements in the structural form compared to large monolithic structures that needed to be machined.[6] The employment of adaptive materials in composite laminates allows the laminate to change its shape (elongation, bending and/or twisting) or stiffness to adjust to a desired form or shape. In the mid 1980s Ed Crawley and his colleges at MIT began their research in the field of adaptive materials and their application in aerospace structures.[12] With the intention of squeezing more performance out of an existing adaptive material the concept of "Post Buckled Precompressed" was discovered. The early discoveries from Lesieutre focused primary towards increasing the coupling coefficient exhibited by piezoelectric transducers.[13-14] The coupling coefficient is normally a measurement for the energy conversion of an adaptive material or active device. The electromechanical device coupling coefficient for example indicates the effectiveness of converting electrical to mechanical energy for a piezoelectric device. Experiments showed that by approaching an axial load close to the perfect column buckling load, the coupling coefficient was approaching a value of 100%. Lesieutre's approach for a beam subjected to an axial load P is shown in Figure 1.

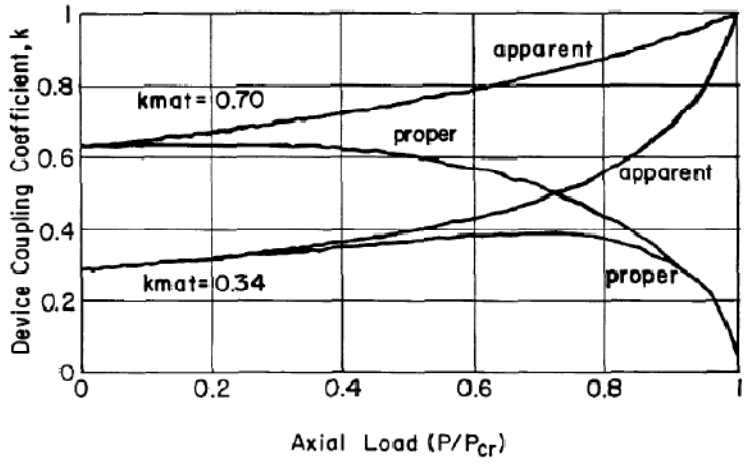

Figure 1: Coupling Coefficient Behavior of Axially Loaded Bending Beams [13-14]

The paradigm shift proposed by Lesieutre 1997 suggested that piezoelectric elements could feature a coupling coefficient higher than the basic material. Lestieutre applied these advanced concepts only to electric transformers but their implication for flight control actuation was clear. The researcher team from the University of Kansas and the University of Delft developed the PBP-principle in a number of high performance actuators.[15-19] The PBP actuators developed exhibit nearly 4 times higher deflection levels than without applied Post-Buckled Precompressed mechanism, while maintaining full blocked force and moment capabilities.

Piezoelectric PBP actuators are highly successful but they inherent some profound limitations. With dynamic elastic shifting and proper control, extremely high speeds and robust performance can be achieved but their capabilities are still limited.[15, 20] Piezoelectric materials are highly prone to tensile failure on convex faces and limited tensile stress levels to fracture. Caused by this limitation, piezoelectric PBP actuators can easily generate such high deflections that they will tear themselves apart. Because SMA actuators are far more tolerant to tensile stresses than piezoceramics, a switch of actuation material was a natural progression of technology. By using SMA instead, very high deformation levels can be achieved. Normally SMA actuators are fundamentally inefficient electrical-to-mechanical transducer mechanism, but employing the SMA actuator in a PBP configuration the efficiency often can be boosted by an order of magnitude. The PBP mechanism inherent another very advantageous characteristic: the power consumption to hold deflections can by reduced by one or two magnitudes. Normally conventional SMA actuators are essentially non-starters for being employed in a control surface on many aircraft, because of their high power consumption to hold the control surface at a specific position. With properly designed SMA actuators the PBP principle can balance air and structural loads and the steady state or trim load on the SMAs becomes almost negligible.

1.1.2 Adaptive Aerostructures

With the development of the first modern adaptive aerostructures by the MIT Research Team in the mid 1980s, a door was opened to apply these new kinds of materials to aerospace structures, a field with unique application areas and opportunities. The employment of adaptive structures in aerospace applications started with simple bending- and twist activated plates in the late 1980s.[21-23] In 1990, Ron Spanglers and Steve Hall's piezoelectric actuator was the first rudimentary flap-type device presented at a AIAA SDM conference.[24] The discovery of the principle of directional attachment of piezoelectric crystals[25] started the development of first adaptive rotors, missile fins, wings and actuators in the early 1990s [26-27] with a first patent issued in August 1995.[28] The developed structures showed great prospects and led to several aero elastic studies. These studies resulted in missile fins that could achieve nontrivial deflection levels, high rates and compact form factors.[29-39] Studies on helicopter rotors, that can be drawn back to the late 1980's, employed piezoelectric materials as rotor blade actuators and showed the advantages which led to the development of the smallest aircrafts commissioned by the DoD (Department of Defense).[26, 28, 40-42] In the following years several new discoveries in the field of developing smart aerostuctures were introduced. One of the largest programs was the DARPA/AFRL/NASA Smart Wing program.[43] The program was divided into two parts; the first part (January 1995 to February 1999) was focused on the development of a shape memory alloy based hinge less, smoothly contoured trailing edge control surface. Variable wing twist was investigated by using SMA torque twist tubes. The critical limitation of the structures developed in Phase I was the low bandwidth inherent with SMA actuation. In Phase II (January 1997 to November 2001) the research was focused on using different adaptive and conventional actuators to actuate the trailing edge of a Northrop Grumman Corporation (NGC) Uninhabited Combat Air Vehicle (UCAV). The actuator materials considered were antagonistically actuated SMA, TERFENOL-D linear wave motor, piezoelectric inchworm motor and piezoelectric hydraulic pump.

In the following section the focus lays on past approaches on integrating adaptive structures into flight control systems, especially for flap or morphing trailing edge devices. An interesting approach in flight control surface design was undertaken by Roelof Vos and Ron Barrett in their paper "Post-Buckled Precompressed (PBP) piezoelectric actuators for UAV flight control."[44] With the discovery of the PBP mechanism by Lesieutre in 1997 new techniques were sought to boost piezoelectric actuator mechanical energy and power densities.[13-14] With the PBP mechanism, ever-lower component count with ever higher performance was achieved. The former developed Post-Buckled Precompressed (PBP) [15-16, 19, 45-50] mechanism was applied to an actuator designed with conventionally attached piezoelectric (CAP) bender members. The actuators consisted of two identically poled PZT 5A sheets that were bonded on either side of a hardened Aluminum substrate. By using the curvature of the actuator, a morphing wing was able to being constructed with an elastomeric latex skin applying an axial buckling force on the actuators in order to use the PBP mechanism. Experiments showed good correlation between theory and experiment. The PBP mechanism nearly doubled the peak-to-peak end rotation to 13.6deg. The authors showed an increase of corner frequency of 10 times and a 60% mass reduction compared to electromechanical servos. As mentioned above the piezoelectric materials are limited in their capability of sustain tensile loads. In order to achieve higher tip rotation a change of the adaptive material was a natural process.

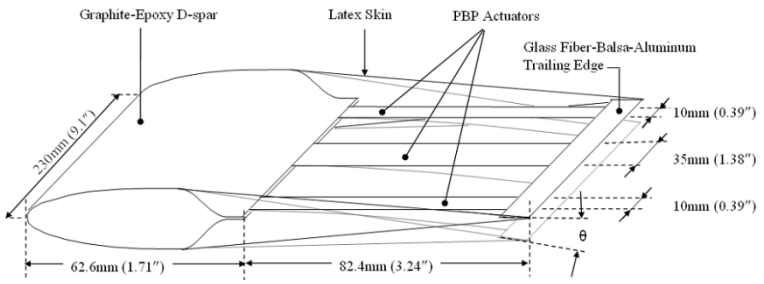

Figure 2: Piezoelectric Actuators for UAV Flight Control[44]

Considering the limitations of piezoelectric materials for actuators with high tip deflections, the decision was made to investigate in SMA actuation. Numerous studies were undertaken in the field of applying shape memory alloys into flap devices, the most unique approaches are outlined in the following. In the paper "Development of a smart wing"[51] Parsaoran Hutapea and his colleges of Temple University discussed the design of an adaptive trailing edge with SMA springs. The flaps were rigidly fixed to a rotating tube that was actuated by SMA springs fixed to the leading edge and the rotating tube (Figure 3) with mounted control surface. The SMA spring actuators were actuated by heat introduced by an applied current. The researchers from Temple University used a NACA2412 airfoil and obtained a maximum angle of flap deflection exceeding 20 deg in both directions. [51] A plain flap design was used in the paper; a shape adaptive airfoil would have increased the aerodynamic efficiency. One group of researchers embedded SMA wires into a NACA 0012 helicopter airfoil section[52] using the same principle as Pasaoran Hutapea. The researchers obtained a tip deflection of 29° with their 0.305 m chord length airfoil and a 2.16 per cent prestrained SMA wire.

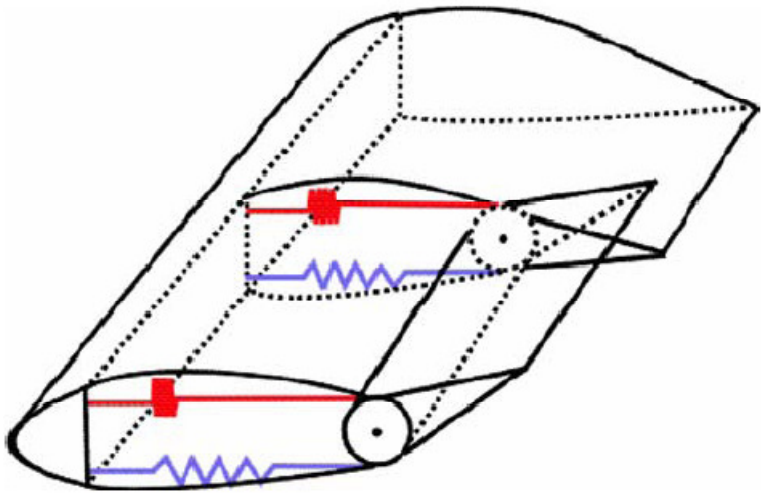

Figure 3: Airfoil with Rigid Flap Mounted on Rotating Cylinder [51]

Another approach was undertaken from Jin-Ho and his colleges from the Korea Aerospace University in their paper "Shape Adaptive Airfoil Actuated by a Shape Memory Alloy and its Aerodynamic Characteristics."[53] The researchers used a SMA thin film actuator embedded in

the skin of the trailing edge to show the improvement of a shape adaptive airfoil compared to a plain and a slotted flap. The airfoil used in this paper was a NACA 23012 airfoil with a chord length of 500 mm. Experiments showed that lift can be improved by 41% and that drag can be decreased by 57% for a shape adaptive airfoil compared to an airfoil with a plain flap. The flaps in their experiment were subjected to a deflection of 30 deg.

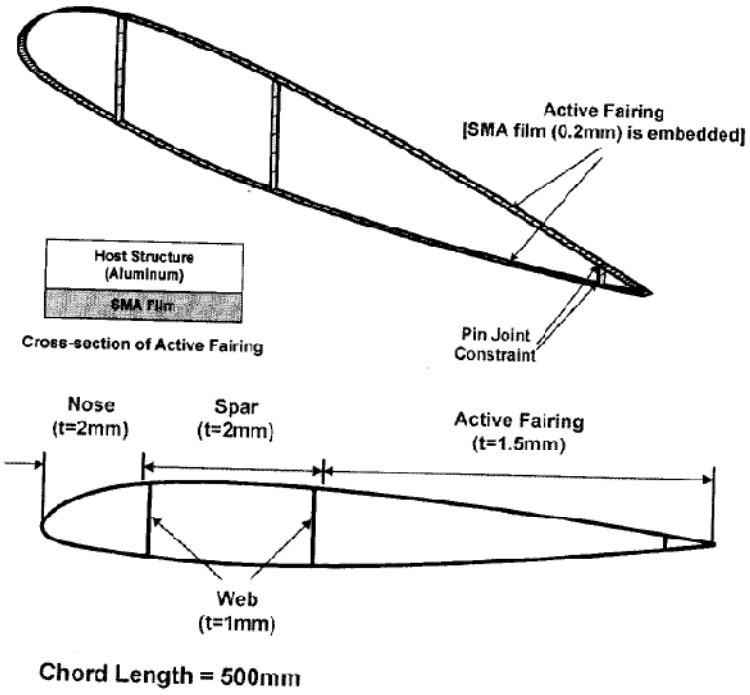

Figure 4: Airfoil with Active Fairing from the Korean Aerospace University [53]

A completely different approach of an adaptive flap system was laid out by S. Barbarino in his paper "A novel SMA-based Concept for Airfoil Structural Morphing."[54] The trailing edge skeleton of the rib consisted of five parts in order to provide the shape of the airfoil; this substructure was then connected by crossed laminates, which were working as structural springs. Actuation was introduced by SMA wires counteracting with the springs. Because of the eccentricity of the SMA wires with respect to the spring system, a relative angular movement could be introduced. Experiments showed tip rotation angles up to 32 deg without aerodynamic loads and 30 deg with aerodynamic loads. The researcher proved that the wire-based SMA actuator preformed best compared to ribbons and rod SMA actuators.

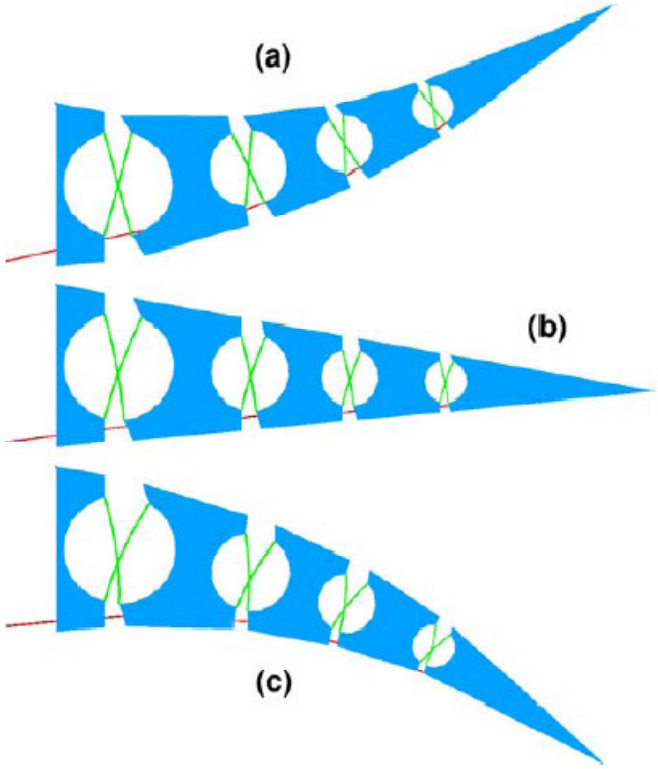

Figure 5: Rib Architecture of the Adaptive Trailing Edge with Hinges (green) and SMA wires (red) [54]

Another interesting approach was undertaken by O.K. Rediniotis and his colleges from Texas A&M University in their paper "Development of a Shape-Memory-Alloy Actuated Biomimetic Hydrofoil."[55] The researchers from Texas A&M used a NACA0009 profile with a chord length of 762 mm with seven ribs that are connected by hinges and actuated by an off center SMA wire. A restoring spring on the other side of the hinge was bringing the SMA wire back to its original position after actuation. This design made it achievable to command the whole airfoil into various shapes. For a better actuation performance and higher actuation frequencies the SMA wires were cooled by water. Experiments showed that frequencies up to 20 Hz were achievable with this setup. An application of the hydrofoil as an airfoil can be easily imagined and was even recommended by the author. Nevertheless the metallic sub and skin structure is too heavy for an aerospace application. For an application as an airfoil the water cooling proposed from O.K. Rediniotis needed to be changed to a lighter fluid to decrease the weight of the entire structure.

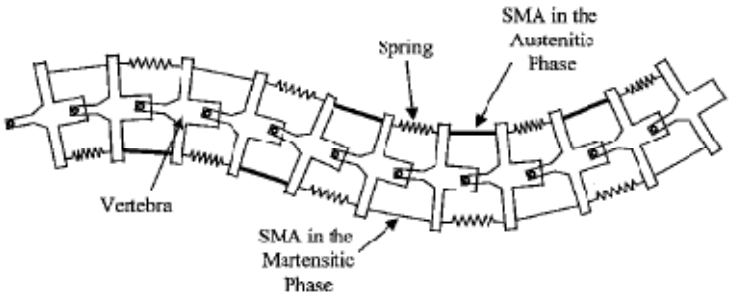

Figure 6: Schematic of Design Principles of Biomimetic Hydrofoil [55]

Figure 7: Maximum deflection of hydrofoil [55]

1.2 Problem Statement

The purpose of this thesis is to describe the development of an adaptive actuator and its employment as a control surface of an adaptive airfoil. The problem that needs to be solved is how to develop this new kind of actuator which brings the advantages of SMA materials and the former developed PBP principle together and prove the concept of a SMAPBP (Shape Memory Alloy Post-Buckled Precompressed) actuated airfoil. The actuator and airfoil need to be evaluated experimentally, analytically and numerically. Adaptive aero structures were chosen over conventional flap system designs because of their decrease in part count and power consumption and increase of work output. The employment of adaptive materials gives the structure the opportunity to adapt to every flight condition by changing the appearance of the airfoil and maximizing the aerodynamic performance. The decision to use Shape Memory Alloy material was made due to the profound limitations of piezoelectric materials. Piezoelectrics are prone to tensile failure on convex faces which makes them not suitable for high deformations and deflections.

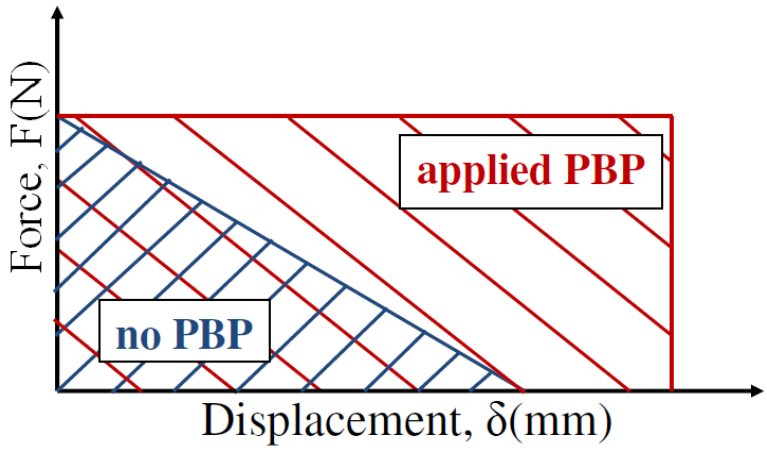

Figure 8: Improvement by Applying PBP-Principle

Conventional adaptive structures (blue area in Figure 8) have only a limited design space, a trade off between developed force and developed deformation is inescapable. These kinds of structures are typically operated at a midpoint in order to obtain force and deformation simultaneously. If maximum force is desired then the deformation will be close to zero, on the

other hand if maximum deformation is favored then the developed force will be almost nonexistent. By applying the PBP principle to these conventional adaptive structures, the design envelope can be increased significantly. The relationship between developed force and developed deformation doesn't have to be linear anymore. For example, the applied buckling force of the PBP mechanism can increase the deformation of the structure without increasing the applied force to the structure. The perfect actuation curve in Figure 8 would be a straight horizontal line. The graph shows that the work output and therefore the efficiency of the actuator can be increased by applying the PBP mechanism (red area: design space PBP mechanism).

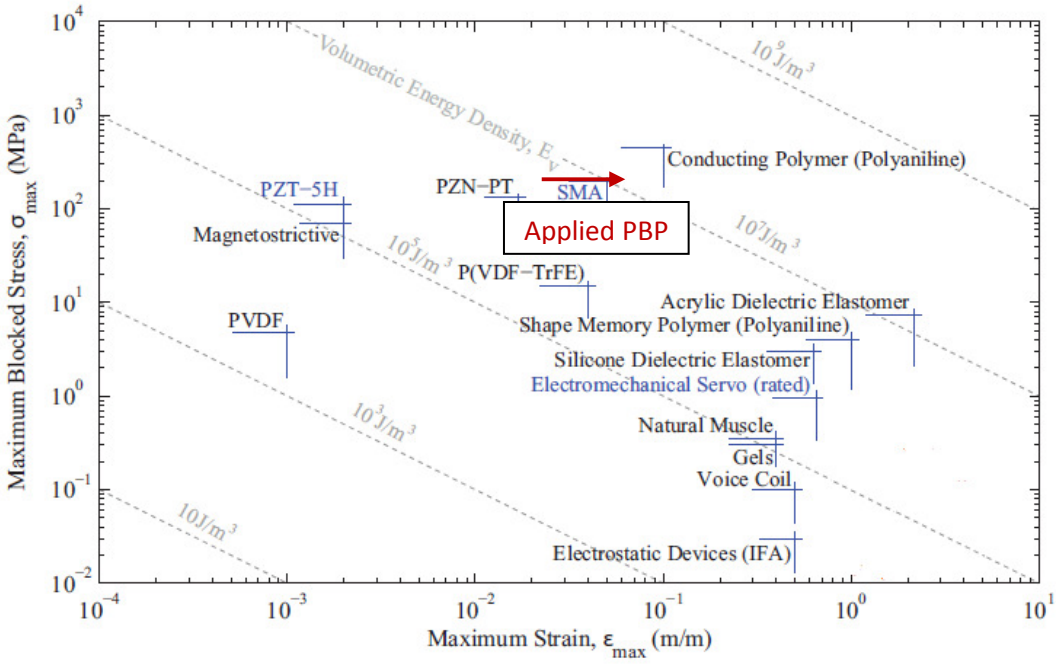

Figure 9: Comparison of state-of-the-art active materials (original from [56])

The PBP mechanism applied to conventional SMA actuators should boost the SMAs deformation output by two or three orders of magnitude. The improvements due to PBP are shown in Figure 8 and Figure 9. The low energy density of conventional SMA materials normally makes them now starters in applications where a certain position needs to be held for a long time. By applying the PBP mechanism to these SMA actuators the energy efficiency could reach a value close to $\eta=1$. Because if properly designed, the PBP

mechanism applied to the actuator can balance out air and structural loads. The steady state load on the SMA actuator becomes almost negligible (Figure 10).

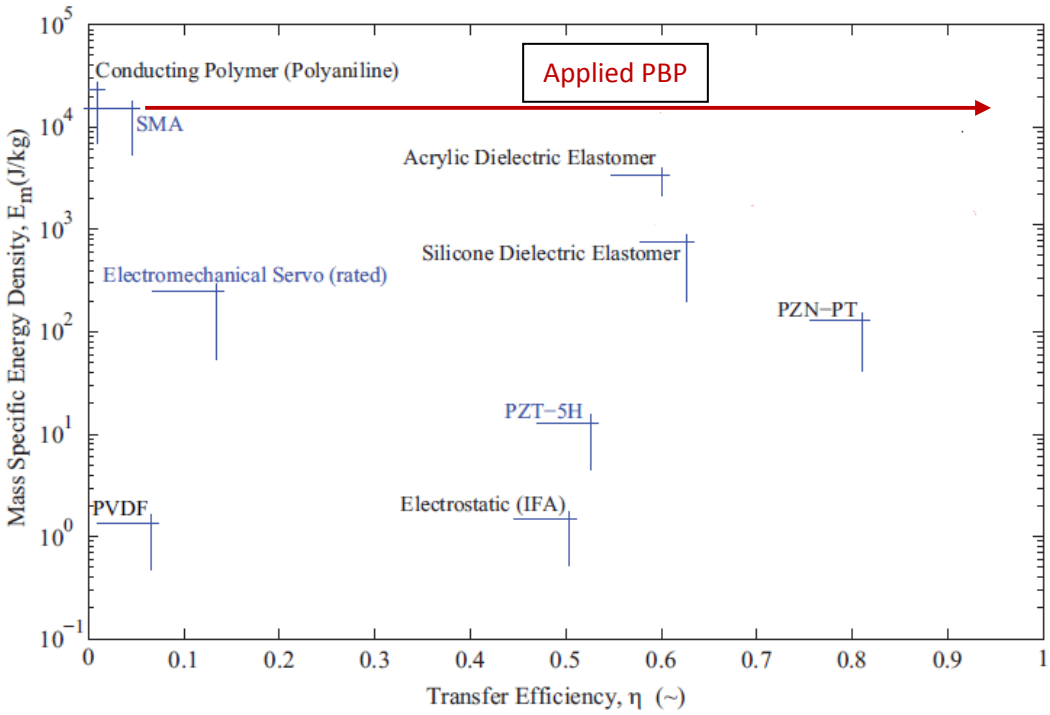

Figure 10: Comparison of mass-specific energy densities of state-of-the-art active materials (original from[56])

The behavior of SMA material is highly non-linear and hysteretic. An active position feedback loop for the actuator integrated in the airfoil should overcome these limitations and should obtain a precise tip displacement.

2 Adaptive Flap System Layout

In order to develop an adaptive flap system with adaptive shape control of the airfoil, it was necessary to integrate the SMAPBP (Shape Memory Alloy Post-buckled Precompressed) actuator into a completely new developed airfoil. The airfoil consisted of four different parts, the SMAPBP actuator, the leading edge, the trailing edge and the skin. The leading edge part had the purpose to give the airfoil the desired aerodynamic outline and stiffness for different flight regimes; it consisted of a simple D-spar configuration. The trailing edge was designed from a steel stock beam connecting the tips of the actuators in order to obtain a straight line for the trailing edge. The SMAPBP actuator itself was the active part of the airfoil and served also as a structural connection between the leading and the trailing edge. The SMAPBP actuator was actuated by contraction caused by an atomic structure change of a NiTi (nickel titanium) shape memory alloy wire when subjected to heat. A latex skin connected the leading and trailing edge and gave the airfoil the aerodynamic shape. The skin also had the purpose to apply a buckling load on the SMAPBP actuator in order to use the advantages of the PBP principle. A NACA0012 profile was used as a basis for the outline of the airfoil shape. The first step was to develop the SMAPBP actuator, optimize it and integrate into the airfoil substructure. Due to the hysteretic behavior of the SMA material it was also necessary to apply an active position feedback control system to the airfoil to accurately piloting a desired flap (trailing edge) displacement.

3 The SMAPBP Actuator

In order to implement the concept of an adaptive airfoil, an actuator with adaptive materials needed to be developed first. The SMAPBP actuator had the purpose of changing the aerodynamic shape of the airfoil and to develop a force big enough to overcome the aerodynamic forces acting on the airfoil. In the following chapters, the conceptual design, manufacturing, experimental and analytical evaluation of the SMAPBP actuator is conducted. The section begins with the basic principles and design ideas behind the actuator and gains into actuation theory. Three different actuator design approaches are discussed and evaluated until an optimum design for the application in the airfoil was selected.

3.1 Actuator Modeling and Design

The principle design of the actuator consisted of plate with constant thickness but tapered from root to tip to accommodate air loads. The actuator plate itself was a composite plate with variant layers for each of the three different actuator designs. The purpose of the three designs was the same; to maximize the tip displacement/rotation and the developed force at the tip. The actuator itself also had to withstand the buckling load applied to the actuator from the skin. The actuators were designed to function with an applied axial buckling load close to the perfect column buckling load of the actuator itself. The perfect column buckling load for the actuator is obtained in Chapter 3.1.5.1 and the force applied by the skin is introduced in Chapter 4.1.

3.1.1 Actuator Design I

In the first actuator design step it was important to prove the basic idea of the PBP concept. The first test specimen consisted of a tapered composite plate with a spring steel substrate and a 45° glass fiber epoxy composite layer on both sides. The actuator had an overall length of 150 mm with 120 mm of active structure that could be actuated by the SMA wire. Due to the fact that air loads result in high root stresses, the plate itself was tapered from 30 mm at the root to 10 mm at the tip. The spring steel substrate had a stiffness of 207 GPa and a thickness

of 0.127 mm. To actuate the steel composite plate, SMA filaments were attached to the top and bottom of the composite plate. An SMA wire with a 0.127 mm diameter, with a stiffness of 75 GPa in the austenitic and 28 GPa in the martensitic state, was selected. A SMA actuation wire of Dynalloy Flexinol[57] was used in these experiments. Another layer of 45° glass fiber epoxy was added to lock down the SMA wire in order to integrate the SMA wire into the composite. The glass fiber layers had the only purpose to create a non conductive layer between the spring steel substrate and the conductive SMA wire. The 45° orientation was chosen to minimize the impact of the glass fiber layer on the overall stiffness of the plate. The glass fiber cloth layers had a stiffness of 4.519 GPa and a thickness of 0.0635 mm for each of the four glass fiber layers.

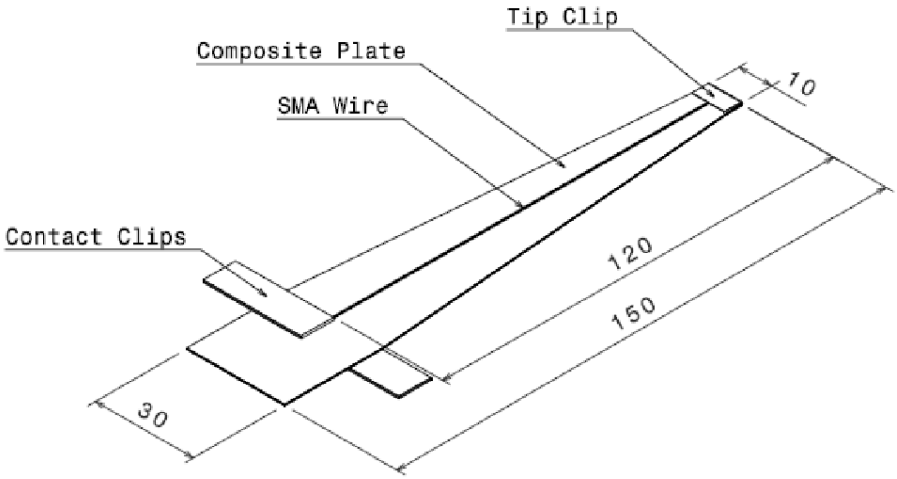

Figure 11: Actuator Design I: Left side is clamped into Test Fixture

Prior to the assembly of the actuator, the shape memory alloy wire was prestrained to 1500 μstrain plastic strain in tension. The atomic structure changes from martensite to austenite by applying heat to the SMA wire. This atomic structure change results in a contraction of the SMA wire and the plate starts to bend. Movement of the SMA wire was suppressed by a clamped steel plate (tip clip) at the tip and a welded steel clip (contact clip) at the root of the test specimen. One single SMA wire was used for actuation of both sides; it was threaded through a transfixion at the tip of the SMAPBP specimen and fixed by a clamped steel plate

close to the root of the specimen, the contact clips. The steel substrate served as an electrical conductor in order to produce a closed electrical loop. This arrangement made it possible to actuate both sides independently. For actuation of one side electric power was applied between one of the contact clips and the steel substrate. The steel substrate and the SMA wire were conductively connected by the tip clip (Figure 32).

3.1.1.1 Evaluation of Actuator Design I

To experimentally prove the SMAPBP concept, the actuator was clamped vertically into a test apparatus (more detailed explanation of the experimental set-up in Chapter 3.3.1). While being actuated, the tip was displaced and the actuator tip rotation angle δ was measured. The impact of the PBP principle was measured by increasing the axial buckling force F_a. The axial buckling force was increased by adding weights to an elastomeric line at the tip of the actuator.

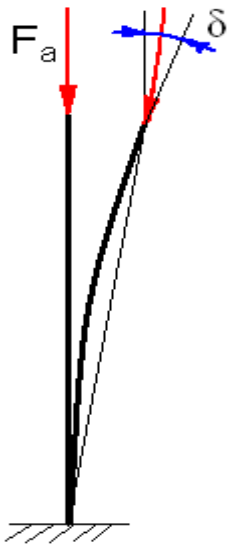

Figure 12: Nomenclature of Principle Experimental Set-Up

With the principle explained above and in Chapter 3.3.1, the tip rotation angle with and without actuation could be obtained and is shown in Figure 13.

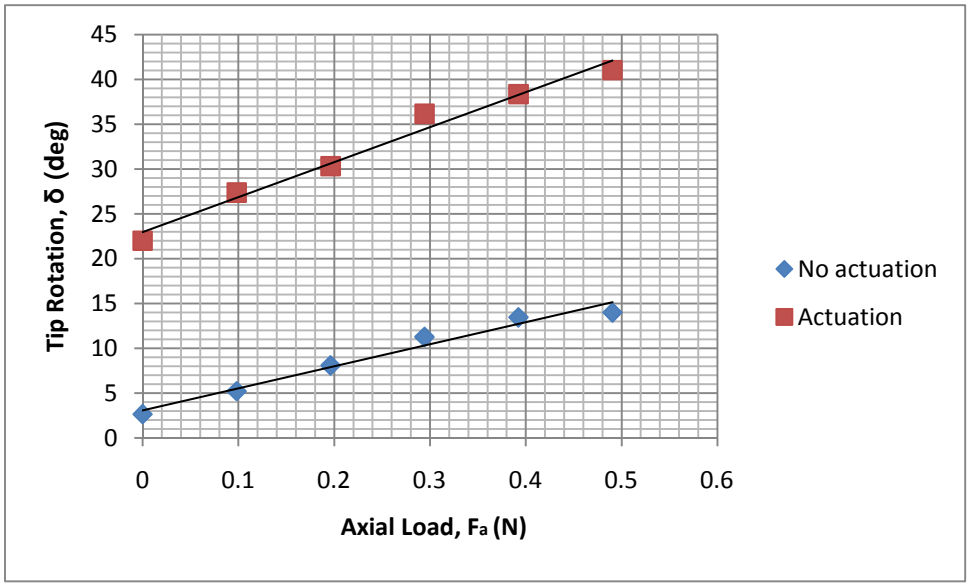

Figure 13: Experimental Results of Actuator Design I

Figure 13 shows a clear increase of the tip rotation angle over the applied axial buckling force. The tip rotation increased from 20° without any applied buckling force to 28° at 0.5 N buckling force. Nevertheless, the impact of the buckling force on the tip rotation of the actuator was too big; an axial buckling force of only 0.5 N led to a tip rotation of 15° without any actuation. Actuator Concept I proved the amplification of the PBP concept clearly, an investigation in a change of material and composite layout was the next step.

3.1.2 Actuator Design II

Because of the difficulties in predicting the correct impact of the composite on the performance of the actuators analytically, this design concept was focused on the impact of a change of composite composition and SMA wire thickness. This actuator was the first type of actuator designed to be integrated in the actual airfoil. This consideration made it necessary to change the location of the contact clips and the clamping area. In this design step different composite configurations and SMA wire thicknesses and their impact on actuation capabilities were investigated. Six new actuators were built, three with the springsteel-glass fiber composite introduced in design concept I and three with only a glass fiber composite with no spring steel substrate. All the actuators of design phase II had the same dimensions. The

actuators had an overall length of 135 mm with an actuated length of 90 mm and were tapered from 30 mm to 10 mm over 90 mm from the clamping position to the tip. The contact clips were moved to the end of the actuator to achieve a clamping area inside the leading edge. This design led to an actuated length of 135 mm with 90 mm active laminate outside the leading edge (see Figure 46 for leading edge specifications).

3.1.2.1 Springsteel-Glassfiber Composite

The composite layup for these three actuators was basically the same as for the actuator from design approach I. Three different diameters of SMA wires were used to capture their actuation capabilities with the spring steel-glass fiber epoxy composite composition. To capture the impact of the thickness of the SMA wire on the actuator, three different diameters of SMA wire (0.127 mm, 0.254 mm and 0.381 mm) were used. Again the spring steel substrate served as a conductor to actuate the top and bottom side separately. The fiber glass used in this design approach was thicker to increase the overall stiffness of the composite plate. The process of finding the right stiffness is a trade off between increasing the stiffness of the plate in order to take the buckling load from the skin versus the improved actuation performance of the SMA wire by using a substructure with less stiffness.

3.1.2.2 Glass fiber Composite

Three different stacking sequences were investigated for the glass fiber epoxy composite actuator. The first actuator in this group had one layer of 0° fiberglass epoxy, the second actuator had two layers and the third had three layers of 0° fiberglass epoxy. All three actuators were equipped with a 0.254 mm diameter SMA wire.

During the experiments the observation was made that with the absence of any conductive layer, the wiring of the actuator was difficult. The current needed to be applied directly to the tip of the actuator. Different approaches have been investigated but none of them led to a satisfactory result. For future design, without a conductive substrate, the best option would be to add a contact clip at the tip.

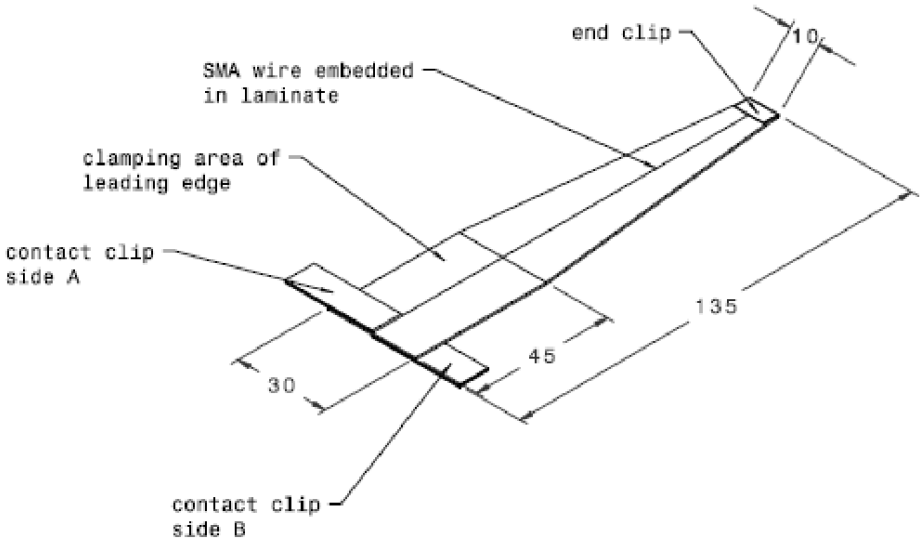

Figure 14: Actuator Design 2: Proposed Actuator for Application in Airfoil

3.1.2.3 Evaluation of Actuator Design II

The different actuator compositions were evaluated using techniques described in Chapter 3.3.1. Only the measurements of the tip rotation angles were used to evaluate the performance of the actuators for these preliminary design concepts.

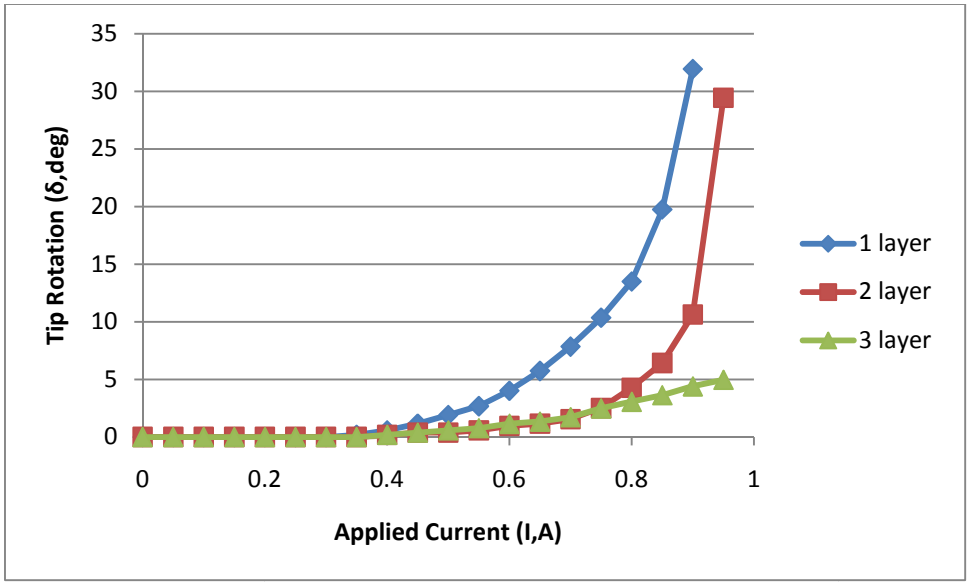

Figure 15: Performance of Glass fiber-Epoxy Actuators from Design II

Figure 15 clearly shows that the available work from the actuator decreases by increasing the number of layers. The one layer glass fiber seemed to obtain the highest performance but it

could never withstand the buckling force from the skin of the airfoil. The three ply specimen could withstand the buckling load from the skin but the work output was too small. Most of the work developed by the SMA wire went into fighting against secondary structure of the actuator.

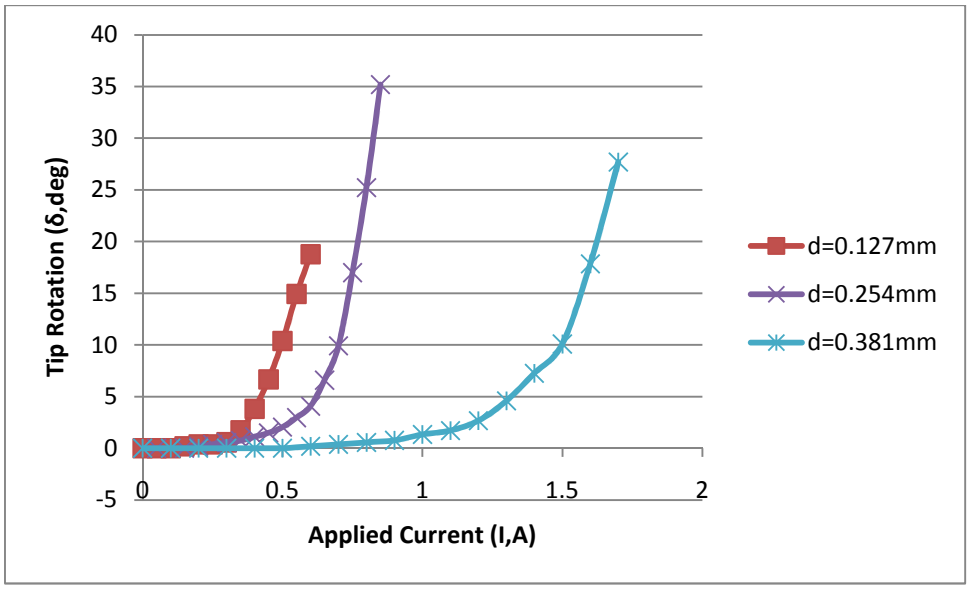

Figure 16: Performance of Springsteel-Glass Fiber Epoxy Actuators from Design II

It is obvious that SMA wires with bigger diameter needed a higher current to be actuated; Figure 16 shows this trend clearly. The current needed to actuate the 0.381 mm diameter was almost three times as high as the current needed for the 0.254 mm diameter. The decision was made to use the spring steel – glass fiber epoxy composite with 0.254 mm diameter SMA wire over the glass fiber approach. This decision was made because the ratio of buckling stiffness over bending stiffness for the glass fiber specimens was too high. The spring steel substrate in the spring steel-glass giber specimens made the whole composite more ductile, an important design criterion for this kind of actuator. The SMA wire's purpose was to bend the composite plate and achieve high tip displacements and tip rotations. The selection of the 0.254 mm SMA wire was based on its good ratio between applied power and developed tip rotation.

3.1.2.4 First Application in Airfoil

After the decision was made to use the spring steel-glass fiber epoxy actuator with the 0.254 mm SMA wire design concept, three actuators were built and integrated into the airfoil. After the skin was applied, all actuators were actuated to evaluate their performance and to prove the basic airfoil concept.

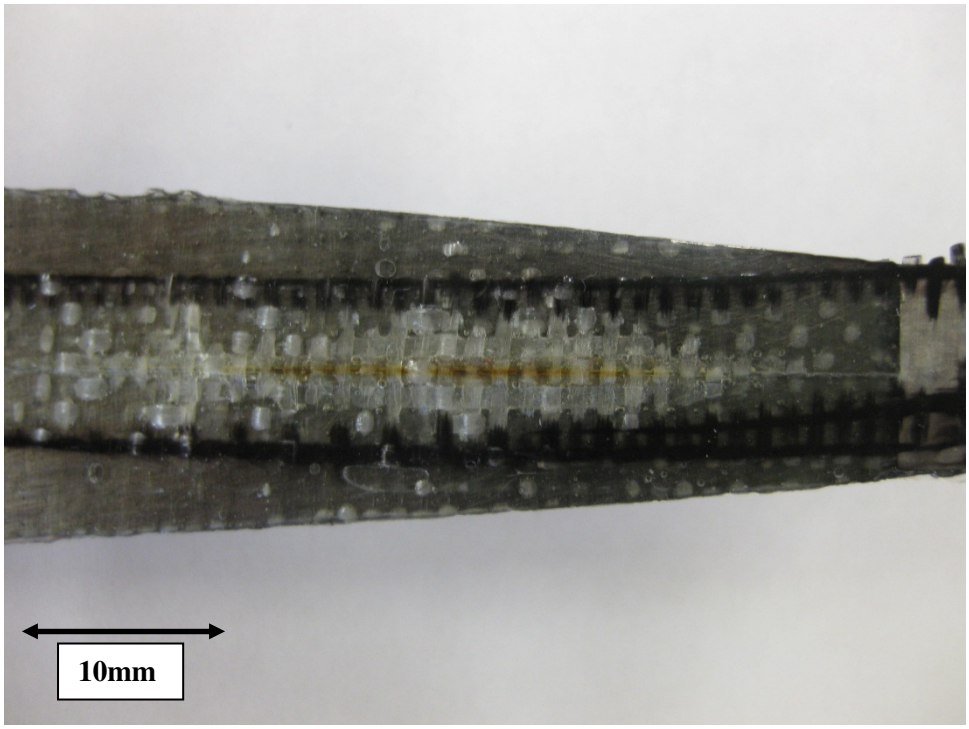

Figure 17: Delamination Caused by Actuation of SMA Wire Integrated in Composite

Experiments showed that the SMA wire embedded in the glass fiber laminate of the actuator needed to be heated up to high temperatures in order to achieve the desired displacement. The epoxy of the glass fiber layers seemed to melt at these temperatures and the laminate started to delaminate. It seemed that the SMA wire was trying to burn through the top layer of the glass fiber epoxy. Temperatures on the order of 110°C to 130°C were measured with a thermocouple attached on top of the glass fiber layer. The impact of this effect was most drastically shown when the actuator was integrated in the airfoil and the skin was applied to the substructure. While heating up the wire for actuation, the temperature increased in the laminate and it strongly degraded the stiffness of the whole laminate and tip rotations of over

90 deg were easily obtained. After turning off the power supply and therefore the heat source, the epoxy hardened again and the actuator got stuck with tip rotation between 70 deg and 80 deg with no chance of recovery to equilibrium condition. Even actuation of the opposite side didn't bring any improvement or recovery.

3.1.3 Actuator Design III

Due to the discoveries obtained in actuator design II, the step away from the SMA wire integrated in the composite was a natural enhancement. In this design the SMA wire was running on top of the composite outside the leading edge. To prevent the SMA wire from interfering with the bond line between actuator and leading edge, the SMA wire was integrated into the composite in the leading edge. This design change also had an impact on the actuation force distribution in the actuator.

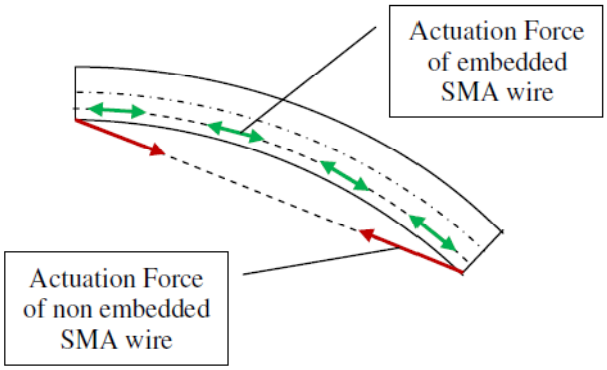

Figure 18: Force Distribution of SMA Wire embedded (green) and not embedded (red) in Composite

In the former design steps the SMA wire was integrated in the composite and the actuation force was modeled as a following force with constant distance to the neutral axis. With the exterior wire of actuator design III, the actuation force of the wire was only acting at the tip and the root. This design modification was adding a vertical component to the actuation force (see Figure 18).

This design also featured a steel spring substrate with two layers of 45° glass fiber epoxy cloth on each side. The SMA wire was embedded between two layers of glass fiber epoxy cloth at the clamping area. The whole actuator had an overall length of 135 mm with an active

tapered length of 90 mm. The 90 mm active length gave the airfoil an overall length of 150 mm with a 60 mm long leading edge (see Chapter 4.1).

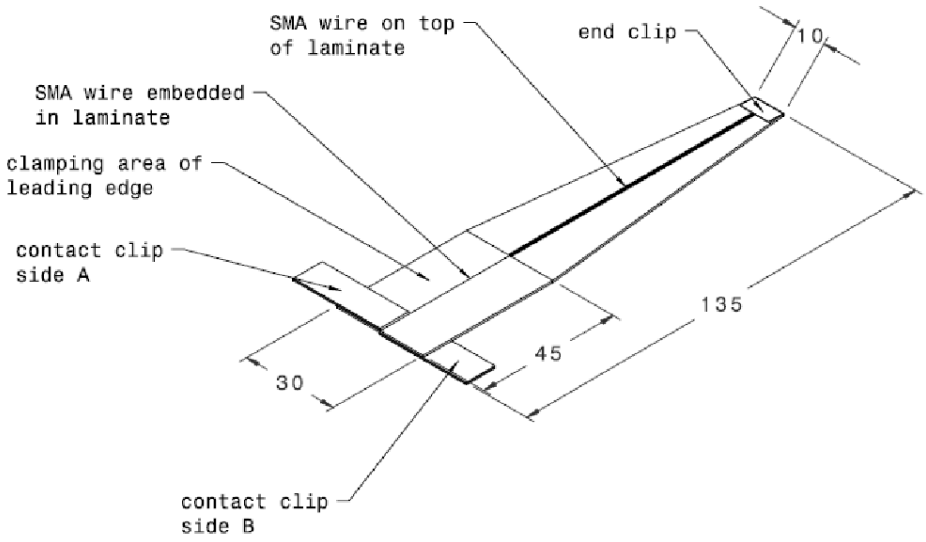

Figure 19: Actuator Design 3: Actual Actuator for Application in Airfoil

This actuator design showed the best performance and most repeatable result of all the actuator designs. This design was selected to be applied into the actual airfoil in order to develop an active position feedback loop and to carry out wind tunnel tests. In the following, this actuator will be referred as SMAPBP (Shape Memory Alloy Post-Buckled Precompressed) actuator.

3.1.4 Antagonistic Arrangement of SMA Wire

The SMA actuation wires in the actuator were arranged in an antagonistic arrangement. This means that the SMA wire that was actuated (e.g. top side) and the SMA wire that was not actuated (e.g. bottom side) needed to be considered in the calculation of the maximum available stroke of the actuator. The SMA wire used in the actuator was a single SMA wire for top and bottom side with a fixture at the tip clip. Before integration the SMA wire into the structure the SMA wire was prestrained to 5% plastic + elastic strain with the Bluehill Instron Tensile Testing Machine (see actuator fabrication chapter; Chapter 3.2). The SMA wire was prestrained over ten full loading/unloading cycles in order to improve its trainability and

performance. The SMA wire was integrated into the substructure without any pretension, only a plastic strain of 2.5% to 2.8% strain was considered for the following calculations. For the solution of the prestrain level of the whole actuator, a graphic solution involving stress-strain curves was chosen. The stress-strain curves were obtained from Tinel Alloy K, a SMA material with similar properties as the Dynalloy SMA wire used in the SMAPBP actuator.

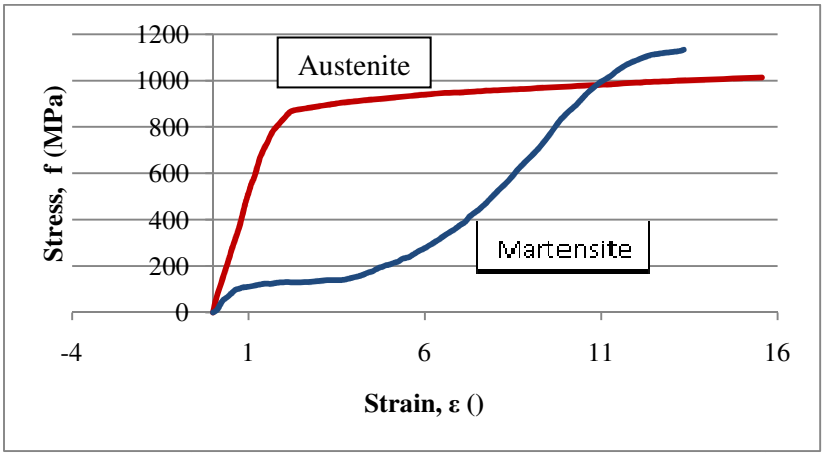

Figure 20: Stress-Strain Curve for Tinel Alloy K[57]

The top and bottom SMA wire can be assumed to be in an antagonistic arrangement with one side clamped with a root mount and the other side movable. The two wires can be assumed to be aligned in one line connected by a center effector. This assumption can be made without any compunction because the SMA wire in the SMAPBP actuator was basically setup in a very similar manner. If for example the top wire is getting actuated and therefore contracts, the SMA wire at the bottom will be subjected to tension and elongates therefore. The bottom wire's stiffness will have a direct impact on the maximum elongation of the top wire. Figure 21 shows the graphic solution for obtaining the maximum available stroke for a given prestrain level. With no prestraining of the SMA wire the structure can not generate any work. By increasing the prestrain level, the two stress-strain diagrams shift together and increase the maximum stroke that can be obtained by the system. The maximum stroke occurs between the cross sections of the curve of the austenitic phase of wire 1 and the curve of the martensitic phase of wire 2 and the other way around.

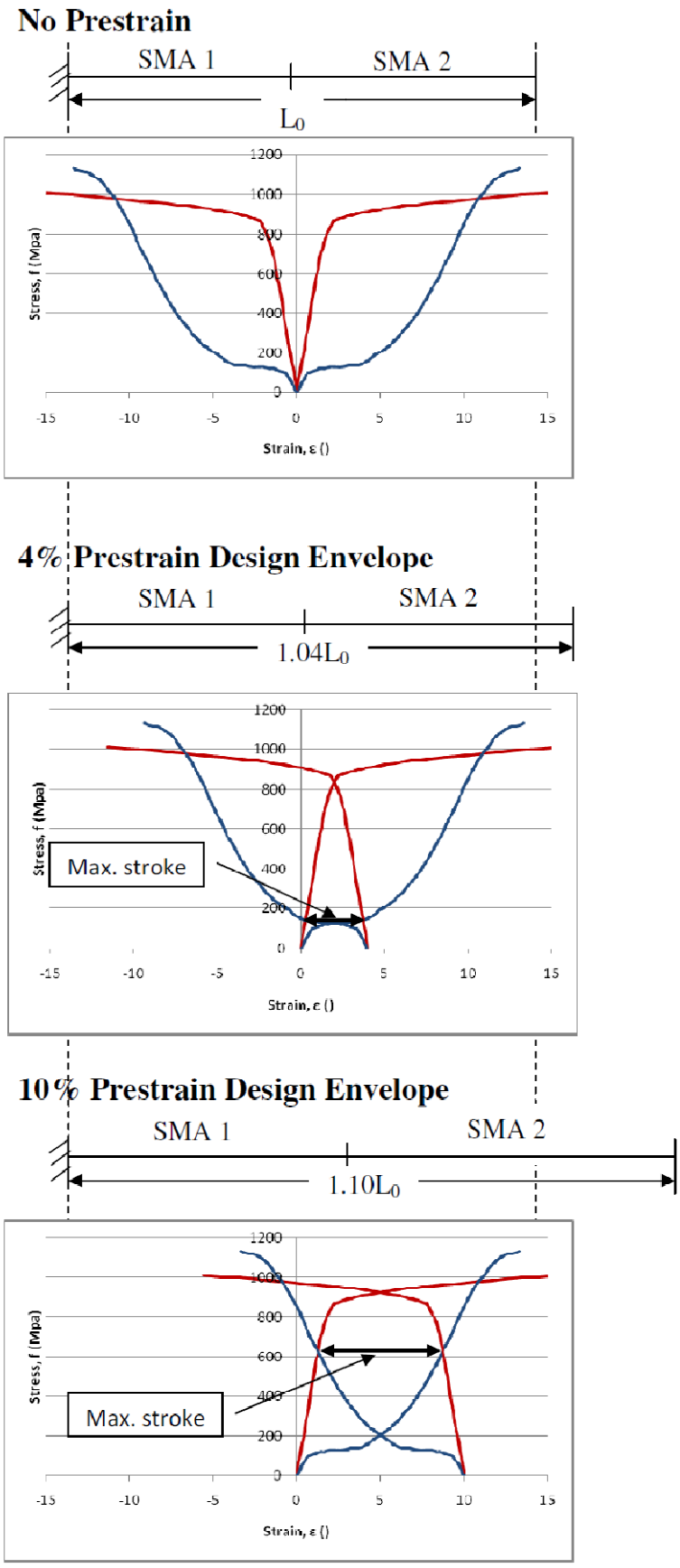

Figure 21: Max Stroke for Antagonistic SMA Arrangement

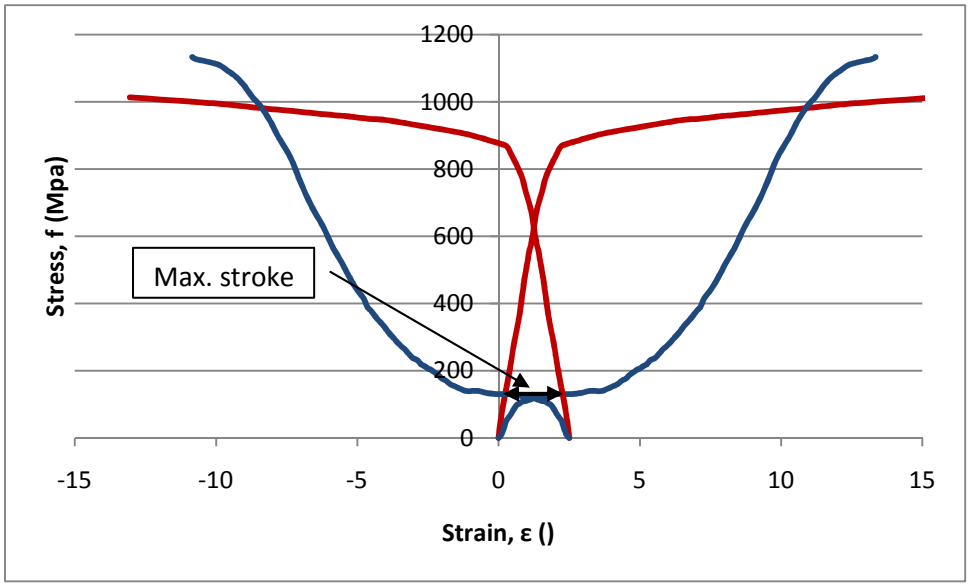

Figure 22: Stress-Strain Diagram for SMAPBP Actuator in Antagonistic Arrangement

Figure 22 shows the stress-strain diagram for the actual actuator with 2.5% elastic prestrain. The two curves leading to the right side of the chart are the austenitic and martensitic line of SMA wire 1 (top side) and the two curves leading to the left side are the austenitic and martensitic lines of SMA wire 2 (bottom side). The graphic solution method described above obtained a maximum stroke of 1.9% strain for the SMA wire in antagonistic arrangement. This maximum stroke was used in the following to calculate the tip rotation in the analytical model and the maximum tip deflection in the FEM model.

3.1.5 Analytical Theory

To capture the nonlinear behavior of the Post-buckled Precompressed (PBP) mechanism a high transverse deflection model developed in reference 50 with excellent correlation between theory and experiment for piezoelectric actuators, was used. The equation needed to be modified in order to capture the behavior of the trapezoidal outline of the specimen. The basics in development undertaken in reference 50 are explained in the following with the necessary modification at the end.

In order to analyze the shape memory alloy bending member a pin-pin configuration with an externally applied force, which is close to perfect column buckling load, is assumed. The static load of the SMAPBP bending element is easily captured by using classical laminated plate theory (CLPT) models. The actuator was made out of three primary components: a pair of shape memory alloy wires bonded with a 45° glass fiber epoxy composite to a structurally stiff substructure. As the shape memory alloy wires were commended to alternatively contract, the bending member deflected.

The applied forces and moments may be balanced by stress distributions which are distributed through the thickness of the element[58]:

$$N = \int \sigma dz \qquad M = \int \sigma z dz \tag{3.1-1}$$

The forces introduced by actuation can be expressed as external forces in the classical plate theory equation. These forces will generate in plane strains, ε and curvatures κ.

$$\begin{bmatrix} A & B \\ B & D \end{bmatrix}_l \begin{Bmatrix} \varepsilon \\ \kappa \end{Bmatrix}_l = \begin{bmatrix} A & B \\ B & D \end{bmatrix}_a \begin{Bmatrix} \Lambda \\ 0 \end{Bmatrix} \tag{3.1-2}$$

Equation 3.1-2 could easily be solved by assuming a balanced symmetric laminate with an introduced strain Λ of the SMA wire from antagonistic arrangement described above. The

curvature of the laminate with the SMA wire embedded in the composite can be calculated with the following equation:

$$\kappa = \frac{B_a}{D_1} \Lambda \qquad 3.1\text{-}3$$

By considering that the SMA wire lays on top of the composite for actuator design III, a new method needed to be developed to obtain the curvature of the specimen.

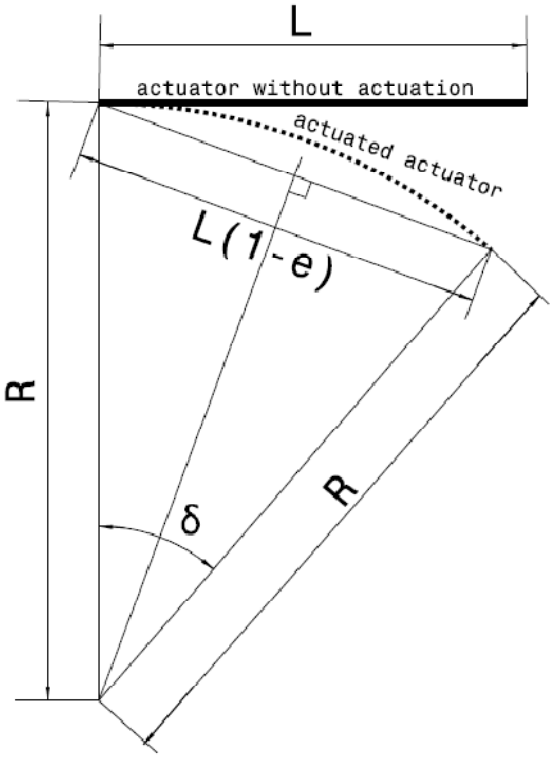

Figure 23: Nomenclature for Determination of Curvature for SMAPBP Actuator

By assuming that the curvature has the same value at each position of the actuator, a relation between the angle δ and the curvature κ could be obtained. By making the assumption that the curvature is constant over the whole length of the specimen an error was introduced. The actuator will have less curvature at the root and more curvature at the tip because of its trapezoidal shape. Nevertheless this approach should obtain an average curvature of the specimen. By using trigonometric and circle function the following equation, that relates curvature κ to induced strain ε, was obtained.

$$\frac{1}{\kappa}\sin\left(\frac{1}{2}L\kappa\right) = \frac{1}{2}(1-\varepsilon) \qquad 3.1\text{-}4$$

Through numerical methods the equation was solved for the curvature κ. By assuming an actuated length of L=90 mm and an induced strain of ε=1.9% a curvature of κ=0.007115 1/mm was calculated.

By using the unloaded laminate curvature,κ as a starting point, the problem can now be defined in terms of gross curvature with externally applied load F_a:

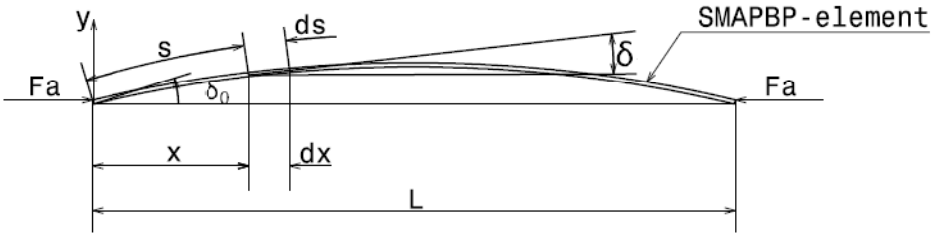

Figure 24: Nomenclature and Terminology for the SMAPBP Element

The angular coordinate, δ is maximized at the ends of the elements, δ_0 and is zero at the midpoint. The normal strain at any point in the SAPBP at a distance y axis through the thickness is therefore:

$$\varepsilon = \frac{y\mathrm{d}\delta}{\mathrm{ds}} = \frac{\sigma}{E} \qquad 3.1\text{-}5$$

By assuming pure bending in the beam element, then the following holds

$$\sigma = \frac{My}{I} \qquad 3.1\text{-}6$$

With classical laminated plate theory the equation 4 and 5 can be combined

$$\frac{yd\delta}{ds} = \frac{My}{Db} \qquad 3.1\text{-}7$$

The externally applied moment from the axial force, F_a can be described as

$$M = -F_a y \tag{3.1-8}$$

Substituting equation 3.1-8 to 3.1-7 yields to

$$\frac{d\delta}{ds} = -\frac{F_a y}{Db} \tag{3.1-9}$$

Differentiating equation 3.1-9 with respect to s

$$\frac{d^2\delta}{ds^2} = -\frac{F_a}{Db} sin\delta \tag{3.1-10}$$

Multiplying through by the integrating factors $2\frac{d\delta}{ds}$

$$s\frac{d\delta}{ds}\frac{d^2\delta}{ds^2} = -2\frac{F_a}{Db} sin\delta \frac{d\delta}{ds} \tag{3.1-11}$$

Integrating equation 3.1-11 yields to

$$\left(\frac{d\delta}{ds}\right)^2 = 2\frac{F_a}{Db} cos\delta + a \tag{3.1-12}$$

By considering the addition of an applied moment via shape memory alloy deformation generating an imperfection across the beam, then the unknown integrating factor, a, can be solved for ($at\ x = 0, \delta = \delta_0, \frac{d\delta}{ds} = \kappa$)

$$\left(\frac{d\delta}{ds}\right)^2 = 2\frac{F_a}{Db}(cos\delta - cos\delta_0) + \kappa^2 \tag{3.1-13}$$

With appropriate trigonometric substitutions and considering the negative root because dδ is always negative:

$$\frac{d\delta}{ds} = 2\sqrt{\frac{F_a}{Db}}\sqrt{(sin^2\frac{\delta_0}{2} - sin^2\frac{\delta}{2}) + \frac{\kappa^2 Db}{4F_a}} \tag{3.1-14}$$

For solution, a change of variable is as follows:

$$\sin\left(\frac{\delta}{2}\right) = csin\xi \qquad 3.1\text{-}15$$

Where ξ is a variable with the value π/2 for x=0 and 0 for x=L/2. Accordingly when y=0:

$$c = \sin\left(\frac{\delta_0}{2}\right) \qquad 3.1\text{-}16$$

Solving for δ and differentiating yields:

$$\delta = 2sin^{-1}\left(\sin\left(\frac{\delta_0}{2}\right)sin\xi\right) \qquad d\delta = \frac{2\sin\left(\frac{\delta_0}{2}\right)cos\xi}{\sqrt{1-\sin^2\left(\frac{\delta_0}{2}\right)sin^2\xi}}d\xi \qquad 3.1\text{-}17$$

Combining equations 3.1-14 through 3.1-17 with appropriate limits:

$$\sqrt{\frac{F_a}{Db}}\int_0^{L/2} ds = \frac{L}{2}\sqrt{\frac{F_a}{Db}} = \int_0^{L/2} \frac{2in\left(\frac{\delta_0}{2}\right)cos\xi}{\sqrt{sin^2\frac{\delta_0}{2}cos^2\xi+\frac{\kappa^2 Db}{4F_a}}\sqrt{1-\sin^2\left(\frac{\delta_0}{2}\right)sin^2\xi}}d\xi \qquad 3.1\text{-}18$$

Considering the trapezoidal outline of the specimen, the shape function of the width is written in equation 3.1-19. Equation 3.1-19.1 had to been solved in the borders 0<s<L and the equation 3.1-19.2 had to been solved in the borders 0<ξ<π/2. In the equations 3.1-19 b_1 stands for the width of the root of the specimen and b_2 is the width at the tip of the actuator.

$$b(s) = b_1 - \frac{s}{L}(b_1 - b_2) \qquad \text{and} \qquad b(\xi) = b_1 - 2\sin(\xi)(b_1 - b_2) \qquad 3.1\text{-}19$$

Combining the shape function (3.1-19) and the PBP equation (3.1-18), the displacement angle can be calculated by the following equation.

$$\frac{1}{2}\cdot\int_0^L \sqrt{\frac{F_a}{D\cdot b_s}}ds = \int_0^{\pi/2} \frac{2in\left(\frac{\delta_0}{2}\right)\cos\xi}{\sqrt{\sin^2\frac{\delta_0}{2}\cos^2\xi+\frac{\kappa^2 Db_\xi}{4F_a}}\sqrt{1-\sin^2\left(\frac{\delta_0}{2}\right)\sin^2\xi}}d\xi \qquad 3.1\text{-}20$$

Equation 3.1-20 was solved numerically to obtain the tip rotation angle δ_0.

3.1.5.1 Optimum Buckling Load for Actuator

To obtain the highest performance of the actuator it was important to design the actuator properly to the buckling load given by the elastic skin or properly choose the skin related to the actuator design. The approach chosen here was to obtain an axial load from the latex skin and properly design the actuator to match the stiffness to be close to the perfect buckling stiffness. This approach was chosen because of the limited availability of suitable off the shelf latex skins for this airfoil. To capture the effect of the trapezoidal shape of the actuator on the buckling load the basic trivial buckling equations cannot be used. A good approximation method for the critical buckling load was developed in the technical note "Analytical Solutions for Tapered Column Buckling" from W. Garth Smith.[59] For a fixed-free column subjected to a tip load with constant thickness and variable width the critical buckling load can be obtained by equation 3.1-21.

$$P_{cr} = Et^3(4(-b_2 + b_1) + \pi^2(b_2 + b_1))/(96L^2) \qquad 3.1\text{-}21$$

with

$$b = b_1 + zb_2L - zb_1/L \qquad 3.1\text{-}22$$

The stiffness of the specimen is E, t is the thickness, b_1 is the width at the root, b_2 is the width at the tip and the overall length of the specimen subjected to buckling is L.

By using the dimensions for Actuator Design III and the stiffness of the laminate obtained by the FEM analyses from chapter 3.1.6, the perfect column buckling load was obtained to be P_{cr}=3.96 N.

3.1.6 Finite Element Model

To prove that the PBP concept was working numerically, the SMAPBP specimen was modeled in the finite element program PATRAN and its solver NASTRAN. An ISO-mesh with Tet10 topology with 6500 elements was created for the SMAPBP actuator. The left end of the tapered part of the actuator was constrained with zero displacements and zero rotations, this constrain served as the clamping position.

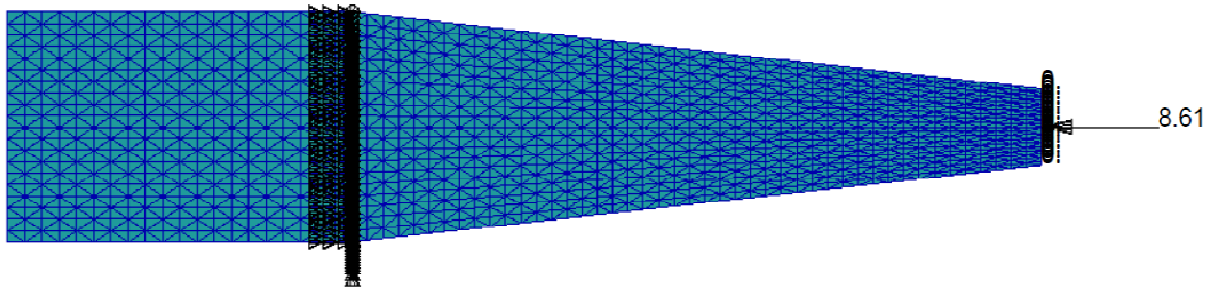

Figure 25: Mesh Generation on SMAPBP Actuator

The thickness of the actuator was measured to t=1.016 mm with a 0.127 mm thick steel substrate, 0.4445 mm thick glass fiber epoxy layers and a 0.254 mm diameter SMA wire. The overall stiffness of the actuator lamina was calculated to 29.9 GPa using PATRAN with a poisson's ratio υ=0.293. The actuation load of the actuator was calculated by using the stress obtained from Figure 21. The stress obtained from the diagram was σ=170 MPa which led to an actuation force $F_{actuation}$=8.614 N. Due to the fact that the wire was only fixed at the clamped area and the tip area, the actuation force was acting on the FEM-node in the middle of the tip top side. The actuation response of the SMA wire can be assumed as a force acting in the direction of the SMA wire.[60-62] To better observe the behavior of the SMAPBP actuator under buckling, the buckling force was increased in 1 N steps from zero buckling force to 5 N. The buckling force was acting on the whole tip area.

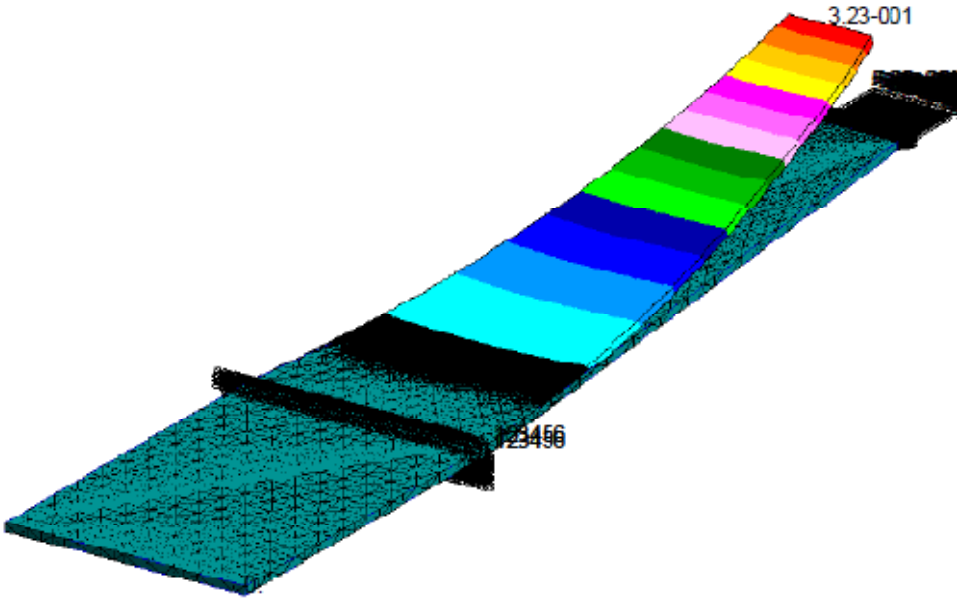

Figure 26: FEM Result for Actuated State and Buckling Force F_a=5 Newton

Figure 26 shows the PATRAN/NASTRAN result of the SMAPBP actuator fully actuated with an applied axial buckling load of F_a=5 N. In the following the results from the various axial buckling cases is outlined.

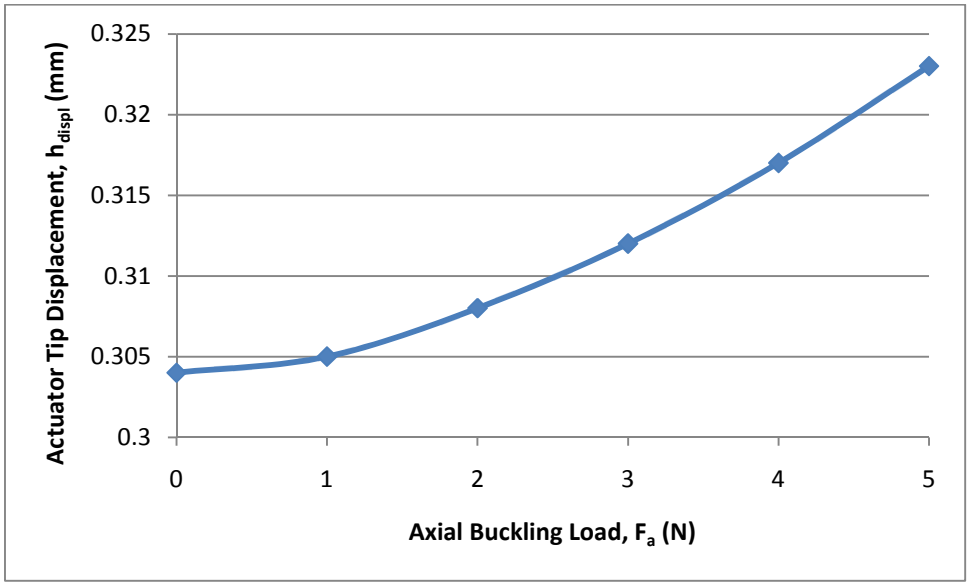

Figure 27: FEM Tip Displacements for various Buckling Load Cases

Table 1: FEM Tip Displacements for various Buckling Load Cases

	F_a=0 N	F_a=1 N	F_a=2 N	F_a=3 N	F_a=4 N	F_a=5 N
Tip Displacement	0.304mm	0.305mm	0.308mm	0.312mm	0.317mm	0.323mm

The results from Figure 27 and Table 1 show that an increase in buckling force results in an increase in tip displacement. Figure 27 even shows that the slope increases with higher buckling load values. The values obtained by this FEM analyses are two to three magnitudes lower than the displacement obtained by experiments, this may be caused by the highly nonlinear behavior of the PBP principle. The FEM model of the SMAPBP actuator had the only purpose to prove that the PBP concept (that tip displacement can be increased by applying an axial buckling force) is working by using Finite Element Models.

3.2 Actuator Fabrication

The actuators of the three different design concepts described above are basically manufactured similar to each other with only small differences (e.g. different composite materials or the embedment of the SMA wire into the laminate). This chapter focuses on the manufacturing of actuator design III, because this was the actuator actually employed in the airfoil. The SMAPBP actuator is manufactured in different steps that took several days because of the necessary curing time of the glass fiber laminates and the adhesives. It began with cutting the 0.127 mm thick spring steel substrate into a trapezoidal shape. The substrate was sanded down and cleaned with alcohol as follows:

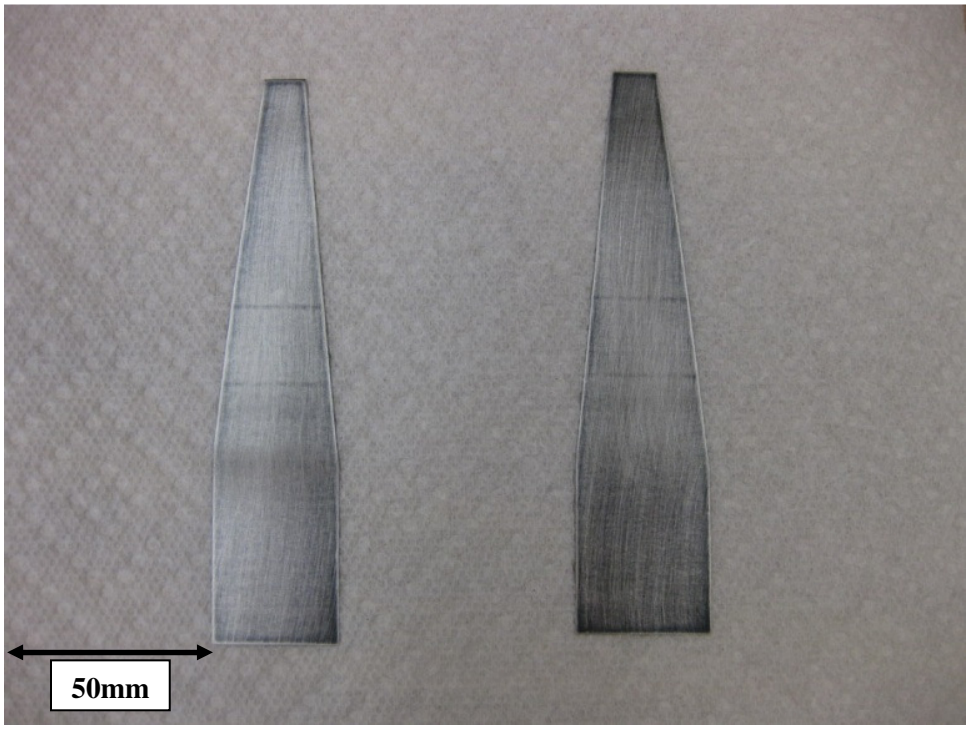

Figure 28: Sanded and Cleaned Spring Steel Substrate

In the next step of the process the spring steel substrate was laminated with glass fiber epoxy. Each side of the actuator was laminated with two layers of glass fiber epoxy; a laminating epoxy from pro-set was selected. The resin (125) and the hardener (229) were mixed by weight with a ratio of 100:30 with a curing time to B-stage of 5-10 hours. The first ply (starting from the substrate) was arranged in an angle of 0° and the second ply of each side

angled 45° in respect to the SMA wire. The second ply began at the end of the leading edge (shown as a black line in Figure 29) to obtain the necessary buckling stiffness of the actuator.

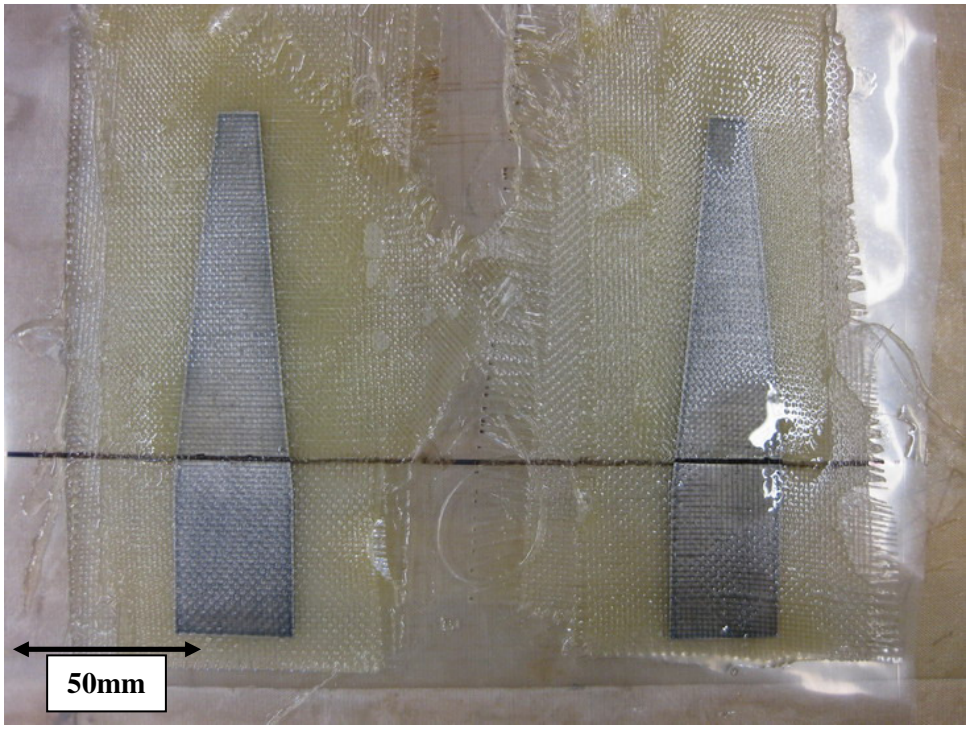

Figure 29: Substrate Laminated with Four Plies of Glass Fiber Epoxy

In the following the whole assembly was put under pressure between to even glass plates and cured under room temperature for 24 hours. After curing, the specimen's glass fiber overhang was cut into the trapezoidal shape of the spring steel substrate. In the next manufacturing step a SMA wire with a diameter of 0.254 mm was prestrained using the Bluehill Instrom Tensile Testing Machine (Figure 30). The wire was prestrained to 5% plastic and elastic strain combined over ten cycles in order to achieve a higher output plastic strain. After ten loading cycles to 5% strain and a load of approximately 50 N, a plastic strain of 2.5% - 2.8% strain could be obtained.

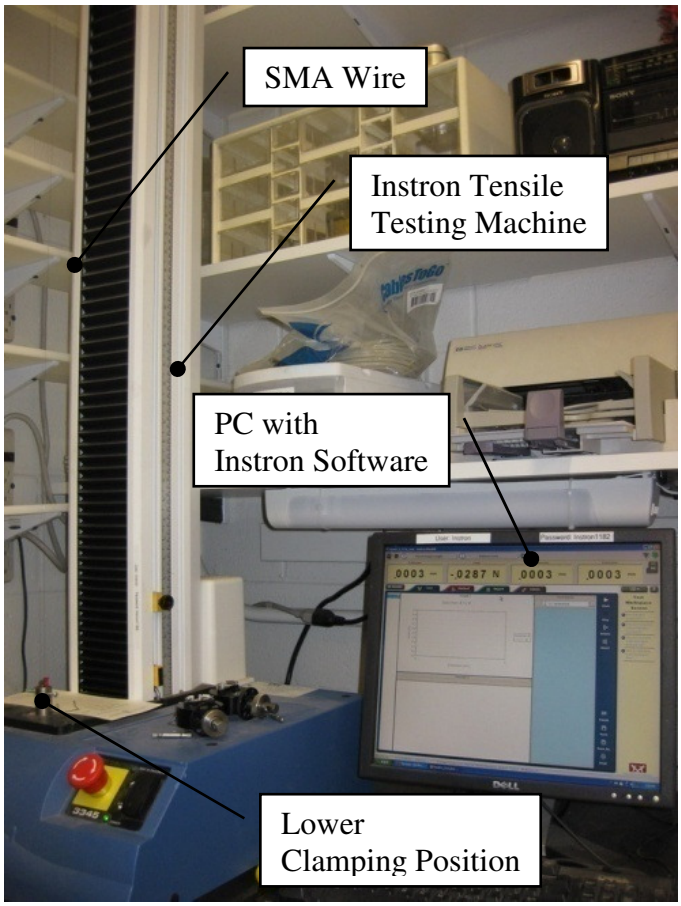

Figure 30: Prestraining of SMA Actuation Wire with Tensile Testing Machine

After prestraining the SMA wire, a fast integration of the SMA wire into the structure was of great importance in order to prevent the SMA from loosing its trained strain.

Figure 31 shows all the parts necessary to integrate the actuation wire into the specimen. The SMA wire was wounded around the steel metal contact clip and then clamped together (Figure 18; to the left and right of the specimen). This tight fit gave the SMA wire a good friction hold.

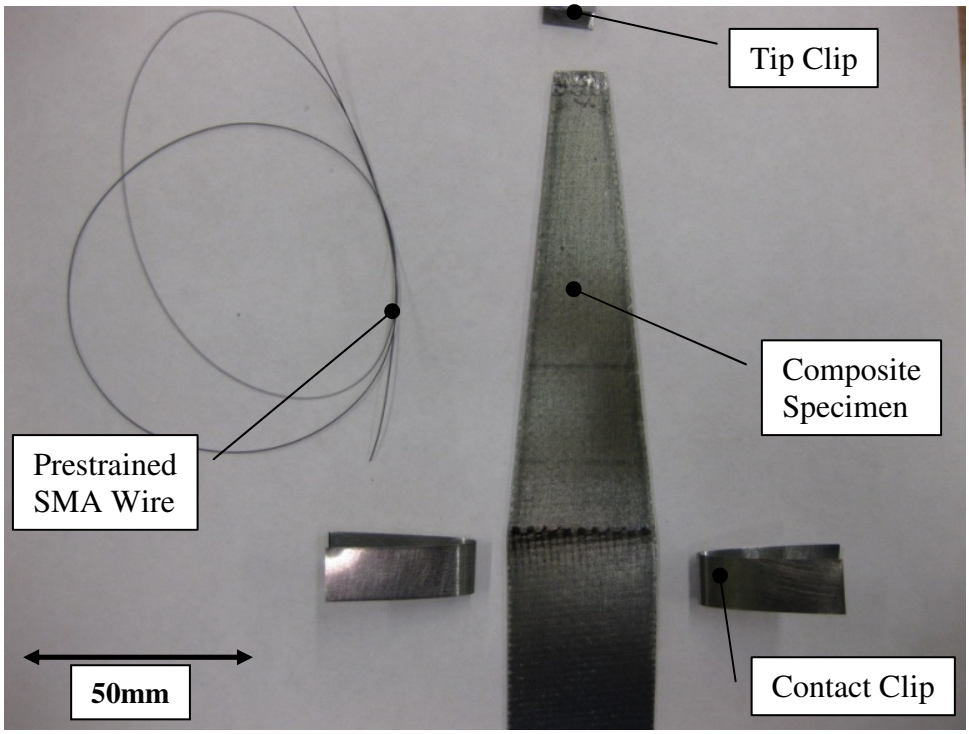

Figure 31: Attachment of Actuation Wire to Actuator with Contact Clips and Tip Clip

The contact clip was bonded to the specimen at the root with Hysool and guided along the top side of the specimen to the tip. The SMA wire was then threat to a small hole at the tip of the specimen for two times and clamped together with a steel tip clip (Figure 30, Figure 32; at top of specimen) to fixate the SMA wire. A small piece of style 120 glass fiber layer at the tip was removed to establish an electrical connection between the spring steel substrate and the SMA wire. The wire was then routed along the bottom side of the specimen and also wounded around a steel contact clip and afterwards bonded to the specimen at the root. The Hysool was cured under pressure for another 24 hours.

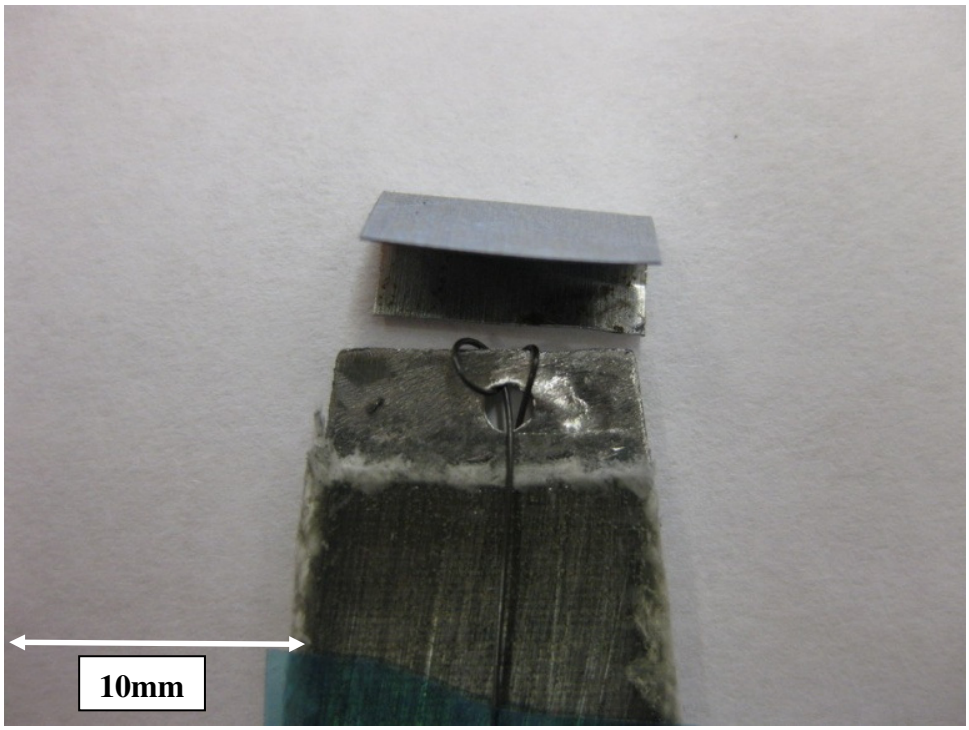

Figure 32: Fixation of SMA Wire with Tip Clip

Manufacturing and testing of the actuators of type I and type II showed that higher displacements and more predictable results can be obtained when the SMA wire is not integrated in the composite. Nevertheless, the specimen needed to be clamped into the leading edge of the specimen. In order to hold down the SMA wire at the clamped area of the actuator, another glass fiber epoxy layer was added over this region (Figure 33). The blue tape in Figure 33 had the only purpose to ensure that the SMA wire in the free region didn't get bonded to the specimen.

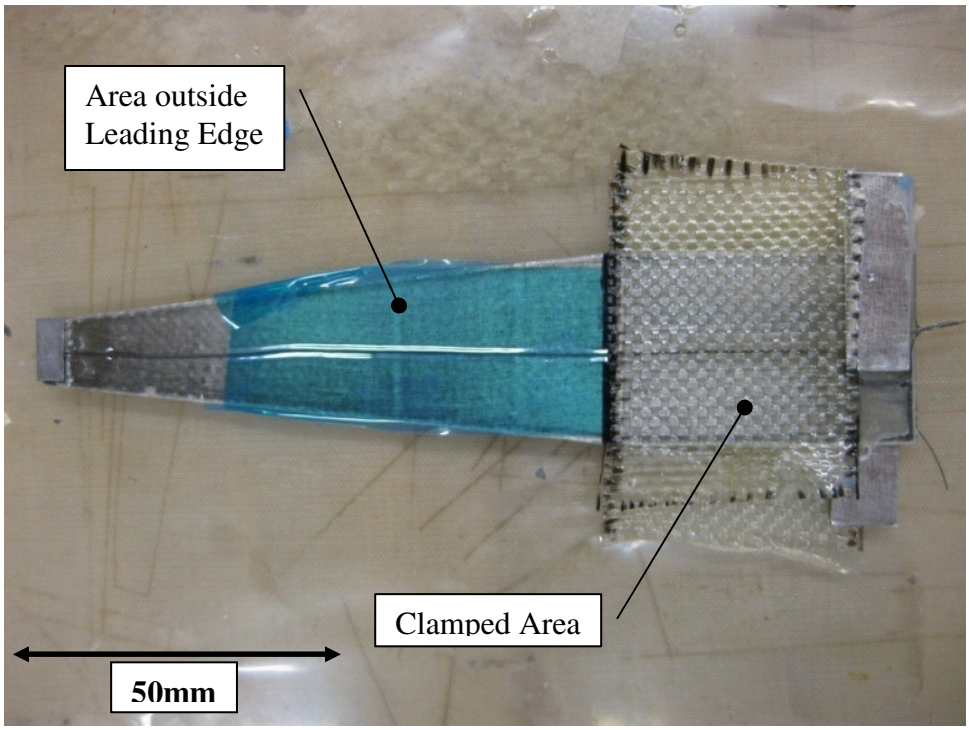

Figure 33: Actuator with Protective Glass Fiber Epoxy Layer over Clamping Position

After 24 hours of curing under pressure, the protective glass fiber layer was cut into shape and three contact cables were soldered to the actuator. For the attachment of the contact wire of the neutral conductor the glass fiber layer needed to be sanded down to the steel substrate.

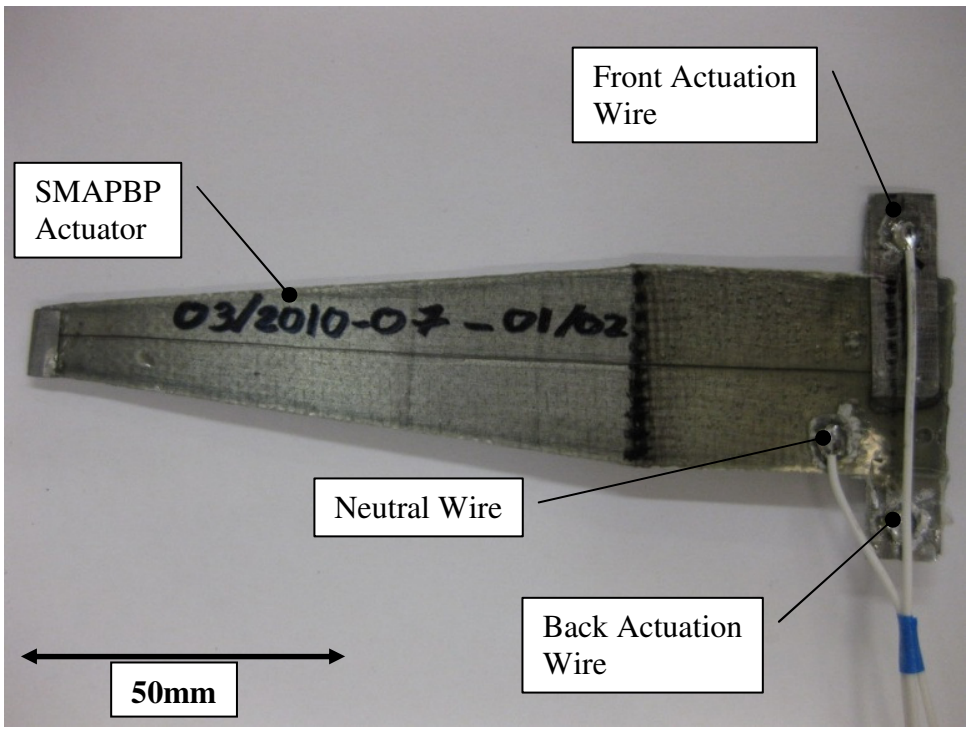

Figure 34: Finished Actuator with Soldered Cables

The finished actuator had three different actuation wires; Neutral Conductor, Positive for Front Actuation and Positive for Back Actuation (Figure 34). The last step in verifying the working capability was to measure the resistance of the SMA wire between the three cables and a test run. The actuators obtained resistance levels in the magnitude of 3 Ω to 4 Ω for each side.

3.3 Actuator Experimental Setup

3.3.1 Tip Rotation

The test specimen was clamped into the test apparatus in a vertical position. To simulate the axial buckling force F_a, a rubber band with weights was attached to the tip of the test specimen. The rubber band ran along the whole length of the specimen, weights could easily be added under the test specimen (see Figure 35).

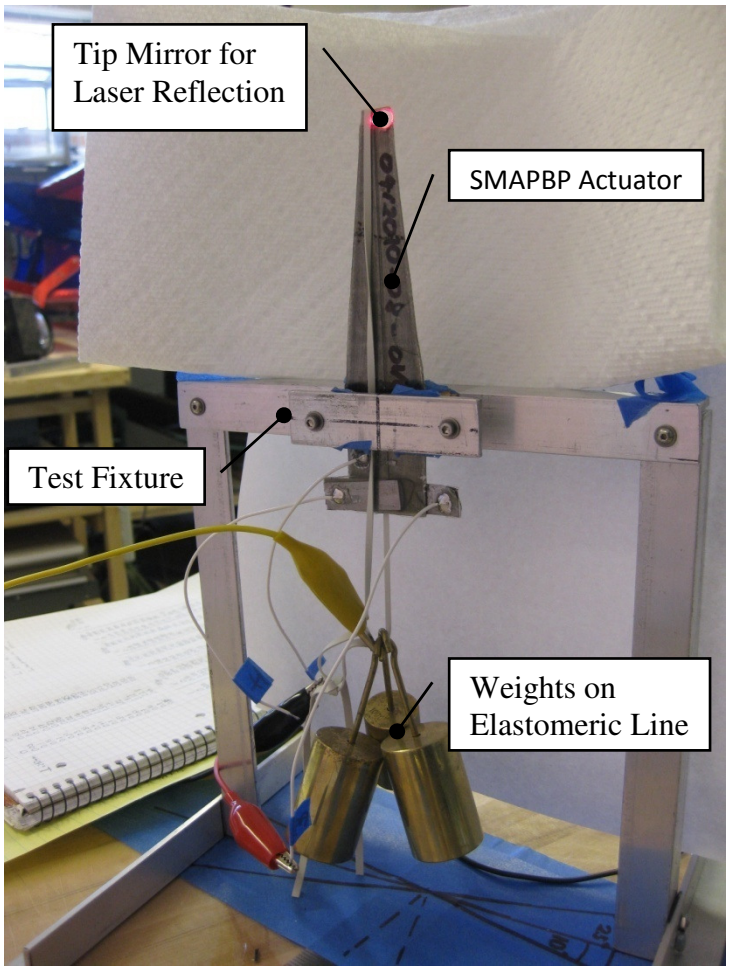

Figure 35: SMAPBP Actuator Clamped in Test Fixture to Measure Tip Rotation

The axial force on the specimen could be increased by adding weights to the rubber band.

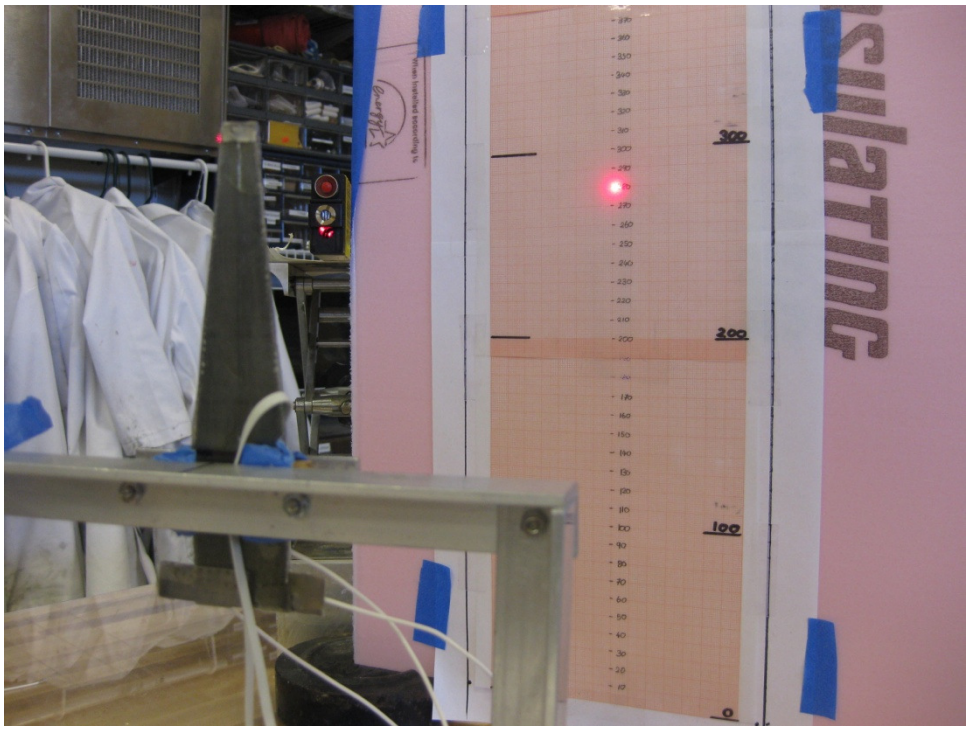

Figure 36: Laser Reflection Method to Measure Tip Rotation Angle

The specimen was loaded in 100 g steps which led to axial force steps of approximately 1 N. A mirror at the tip of the actuator was used to measure the tip rotation of the specimen. A laser beam from a laser leveled to the height of the tip was reflected to a displacement measuring device in the distance (Figure 36). This test setup made it possible to measure the tip rotation angle accurately. By applying an electric current on either the top or the bottom SMA wire, the SMA wire started to heat up and therefore contract. The resistance of the SMA wire was used to heat up the SMA directly without the need of an external heat source. The SMA wire was heated up until the martenitic structure of the actuator wire completely transformed to the austenitic structure. The magnitude of the voltage and current needed for this transition was on the order of 3 V and 0.7 A.

3.3.2 Tip Force

In order to evaluate the performance of the actuator in the actual airfoil, it was of special importance to know the force developed at the tip during actuation. The tip force had to be high enough to overcome the pressure applied to the trailing edge and the skin by the airflow

around the airfoil. The pressure distribution was obtained by a CFD-model developed and described in Chapter 4.3.5.

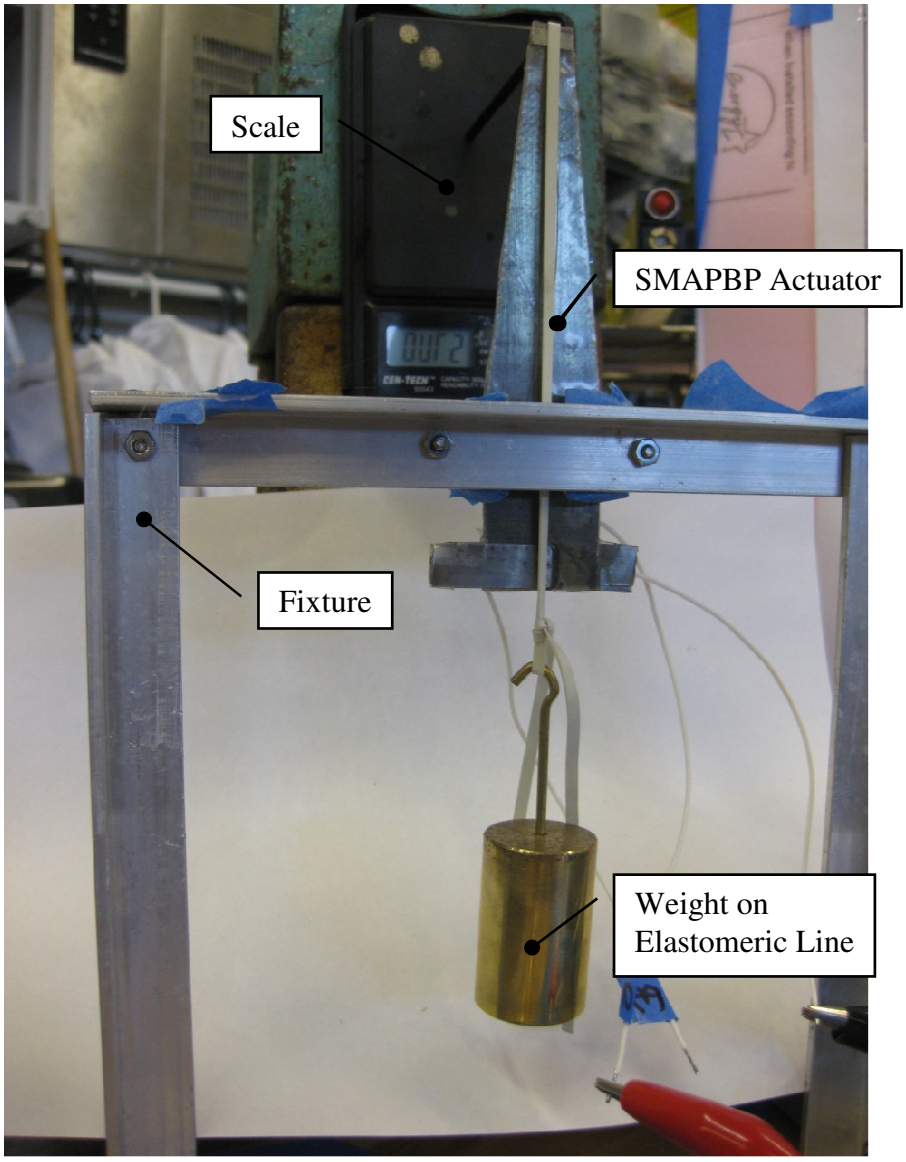

Figure 37: Actuator in Test Fixture to Measure Blocked Tip Force

To measure the tip force, the test specimen was again clamped vertically in the same test apparatus that was used during the tip rotation measurements. The test apparatus itself was looked into place by applying heavy weight to its stand. A weight scale was mounted vertically on some heavy weights to ensure no slipping; it was ensured that the center of the scale and the tip of the test specimen were horizontally aligned. A circular carbon rod was

attached horizontally between the test specimen and the weight scale; it was ensured that there was only a minimum force applied to the system at the beginning of the experiments.

3.4 Actuator Experimental Testing and Theoretical Results

3.4.1 Actuator Tip Rotation Angle

As a first step it was important to ensure that the actuator had the same performance (tip rotation angle) on both sides. Without any applied buckling force the actuator was fixed in the test apparatus described in Chapter 3.3.1. Figure 38 shows the performance of the actuator for this case. The applied negative current served the only purpose to clarify that the opposite side of the actuator is actuated. The polarity of the applied current is in general inconsequential for the actuation of the SMA wire.

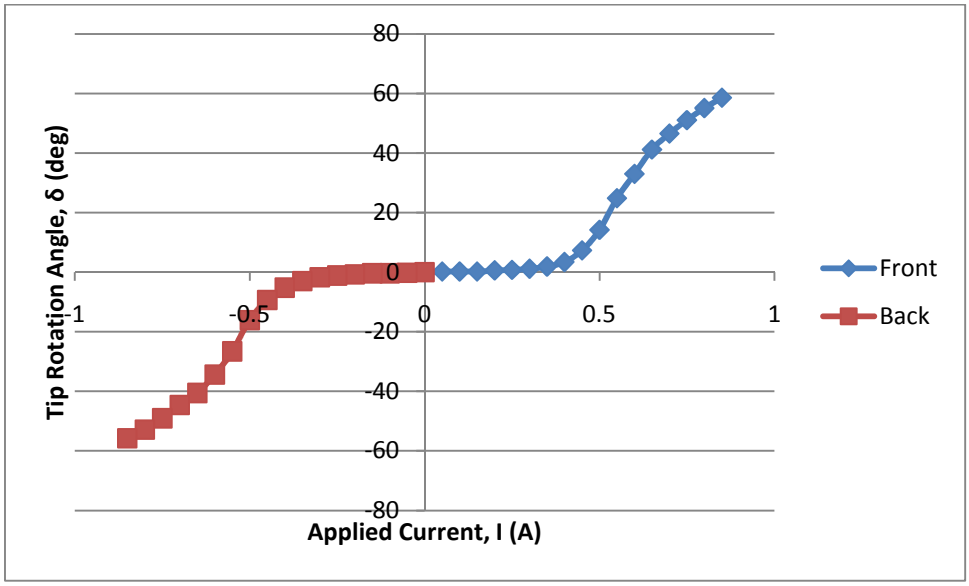

Figure 38: Actuation of Both Actuator Sides

The curves from Figure 38 are standardized and corrected to zero tip rotation in order to validate the similarity of the two curves more accurately; a zero tip rotation angle of 4.57 deg was measured at the beginning. The two curves show similar results and similar maximum values, with δ=58.59 deg for front side actuation and δ=-55.72 deg for back side actuation. These results gave the fundamentals to apply the actuator in the actual airfoil. Both side actuation gives the airfoil the opportunity to be employed as an aileron or elevator (based on

the similar tip rotation angles and not based on the reaction time necessary for such kind of control surfaces).

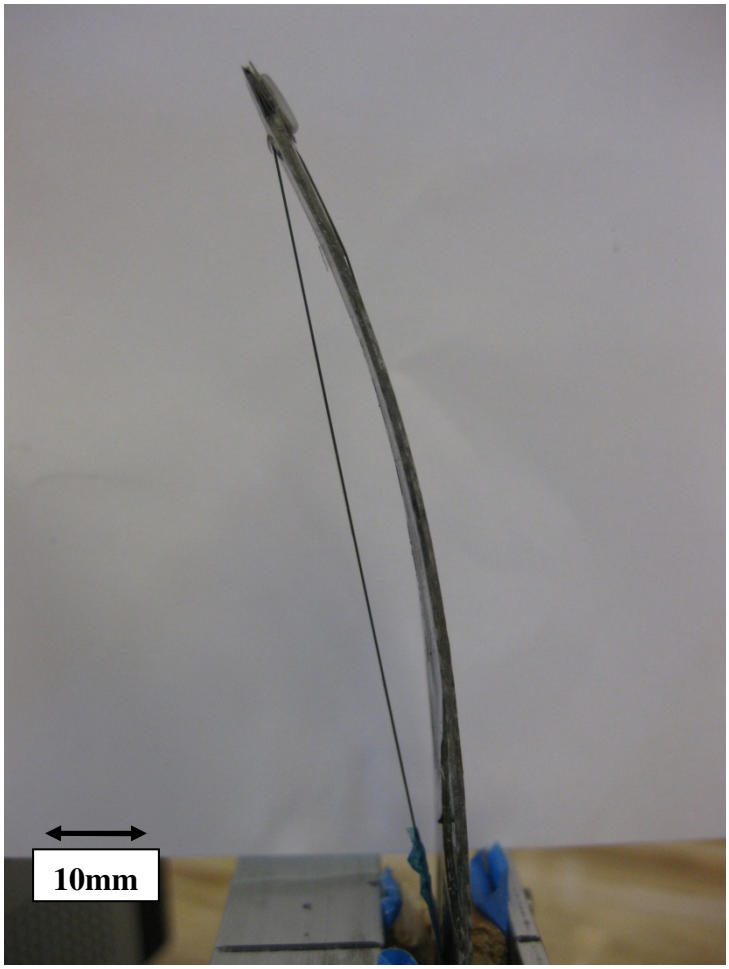

Figure 39: Actuated Actuator in Test Fixture at Maximum Current

With the test set-up described in chapter 3.3.1 the tip rotation angle over applied current for various axial buckling load cases was obtained next. All measurements were taken in a small time span to ensure the comparability of the result to each other and eliminate any environmental influences.

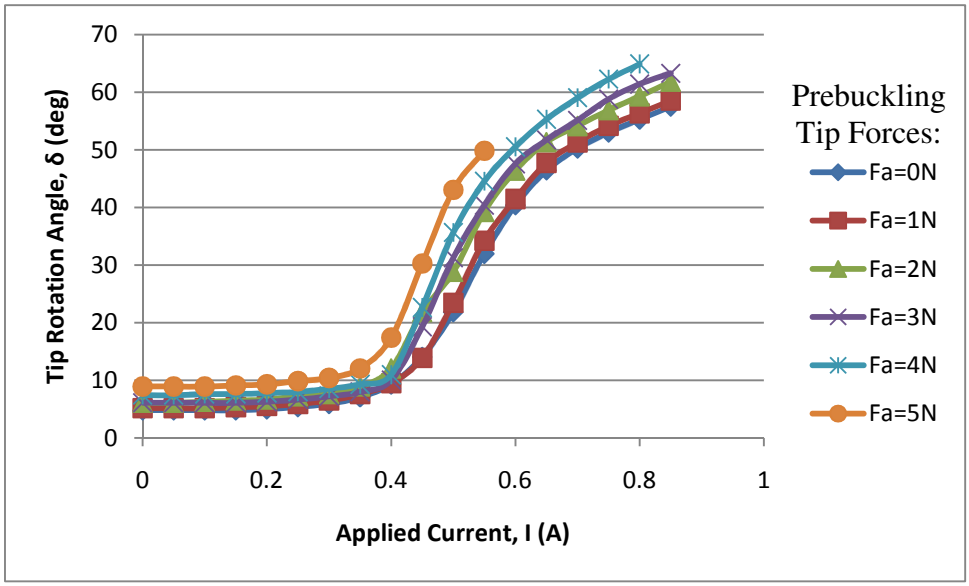

Figure 40: Experimental Data: Tip Rotation Angle over Applied Current

Figure 40 clearly shows a trend to higher tip rotation angles by increasing the axial buckling load. The figure also shows that the displacement with no applied current increases with increasing axial force, this may be caused by bending and buckling phenomena from the applied axial load. The slope of the curves for the different load cases followed also the same pattern. The actuator had nearly no response in the first part of the slope (0A<I<0.4A), followed by a steep rise (0.4A<I<0.75A) and a plateau phase where the tip rotation angle seems to reach a maximum in the order of 55 deg to 70 deg dependent on the applied buckling load. The measurements of the F_a=5 N curve had to be cut off at I=0.55 A because the air conditioning in the lab turned on and corrupt the measurements. The measurements were good enough to prove the concept and to obtain trends so the decision was made to use the data obtained in this experiment.

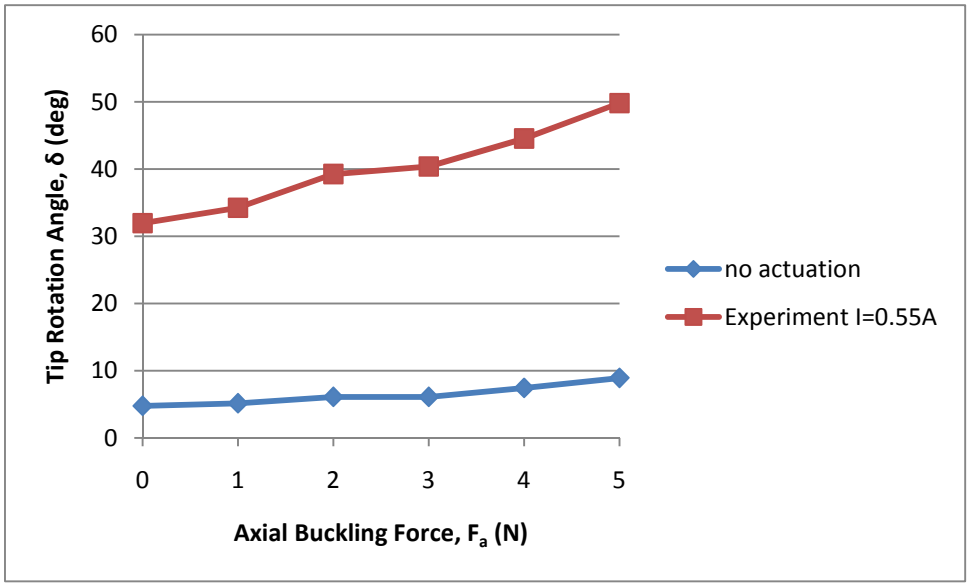

Figure 41: Experimental data for I=0.55A: Tip Rotation over Buckling Force

Figure 41 shows the experimental data for the tip rotation over the buckling force F_a for the non actuated case and the actuated case. The figure shows that the test specimen already had a tip rotation of 4.76 deg at the start of the experiment without any axial load; this displacement may be caused by the hysteresis of the SMA wire after test actuation prior to the experiment. By subtracting the displacement caused by the external axial force with the displacement due to actuation of the wire, an improvement of 33.5% of tip rotation angle could be obtained by using the Post-Buckled Precompressed (PBP) mechanism in comparison of using the specimen without any externally applied load. An improvement of up to 50.5% of tip rotation angle could be achieved with higher current levels, but due to the fact that the control system described in Chapter 4.2 could only provide a maximum actuation current of I=0.6 A, the 0.55 A case seemed to be the right fit for the proposed application in the airfoil.

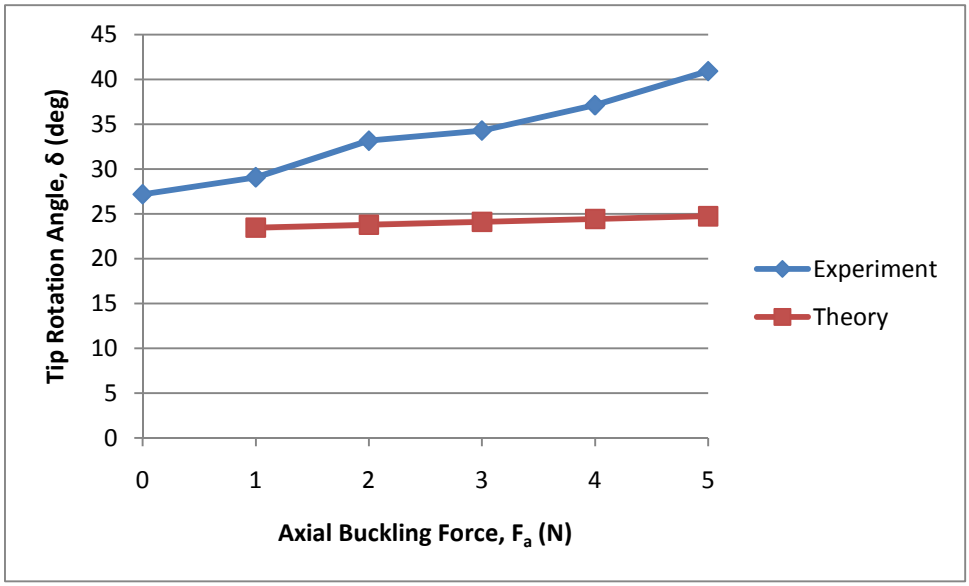

Figure 42: Experimental and Theoretical Data: Tip Rotation over Buckling Force

The test procedure described above and the iteration of equation 3.1-20 led to the results shown in Figure 42. The figure shows the experimental and theoretical results over an applied axial force, F_a. It is obvious that the experimental and theoretical results are vary greatly, this is may be caused by the highly nonlinear and hysteretic behavior of the SMA wire which is exacerbated by the Post-Buckled Precompressed arrangement. The slope of the two curves is one to two orders of magnitude off.

3.4.2 Actuator Tip Force

The test setup described in chapter 3.3.2 obtained the results shown in Figure 43 for an actuator from design concept III. All the experiments were undertaken in a short amount of time to ensure their comparability, so that variable environmental conditions (room temperature, variable air flow from air conditioning …) don't corrupt the measurements.

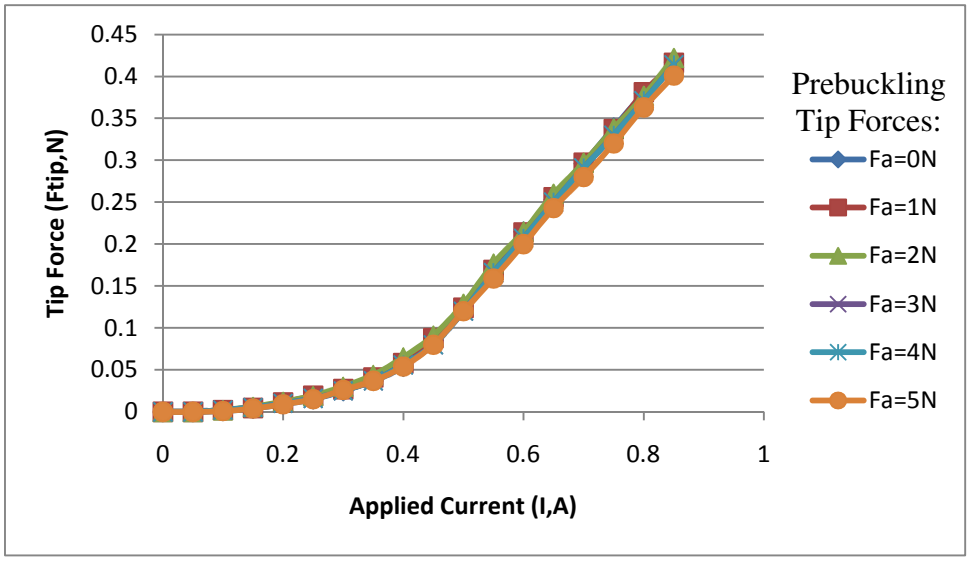

Figure 43: Blocked Tip Force over Applied Current

Figure 43 clearly shows that the applied axial buckling load had limited or no impact on the developed blocked tip force. The difference in tip force between the unloaded case and the case with a buckling load F_a=5 N was only -3.83% at an applied current of 0.85A. The impact of a change in axial buckling force on the tip force couldn't therefore be neglected. Nevertheless it was from great importance to know the maximum achievable tip force to validate that the actuator can achieve a high enough force to overcome air loads (pressure on skin) obtained by the CFD analyses.

The CFD analyses described in Chapter 4.3.5 obtained the forces acting on the airfoil and the actuators at an angle of attack between α=0° and α=10° and for tip rotation angles between δ=0° and δ=30°. The CFD analyses obtained a maximum tip force of $F_{tip\ max}$=0.405 N for each actuator. Experiments (Figure 43) showed that the actuator can achieve blocked tip forces in excess of 0.45 N.

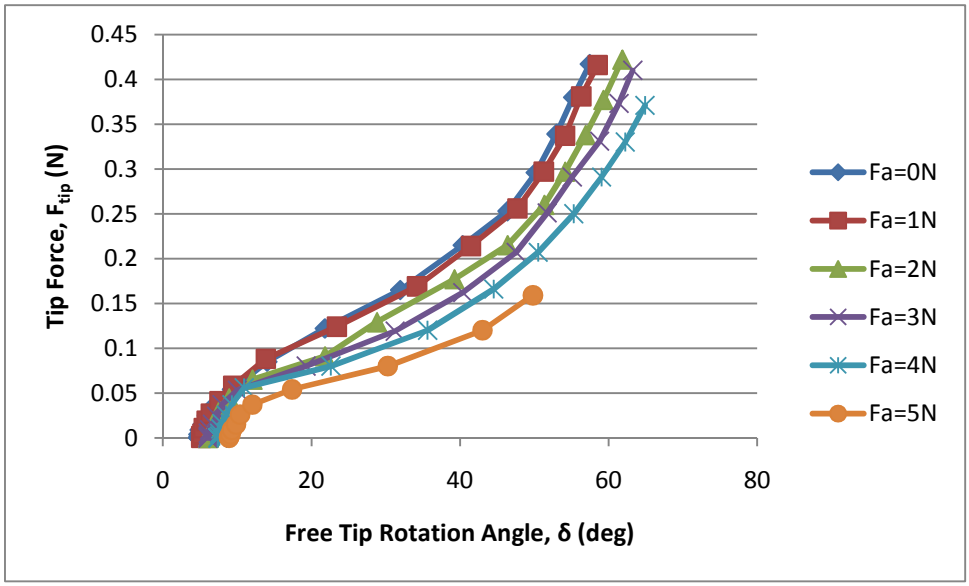

Figure 44: Available Tip Force over Free Tip Rotation Angle

By combining Figure 40 and Figure 43, a graph with tip force over free tip rotation angle could be obtained (Figure 44). Former graphs showed that by increasing the axial buckling load F_a the rotation angle significantly increases and the blocked tip force slightly decreases, with Figure 44 this becomes more obvious. The graph only shows the free rotation angle (without any applied force to the tip) and the blocked stress (without any movement of the tip itself). For the application of the actuator in the actual airfoil a closed position feedback loop (Chapter 4.2) controls the tip displacement.

4 Adaptive Airfoil Specimen

In the next step, the SMAPBP actuator developed in the previous section was incorporated in an airfoil. This section explores the capabilities of the SMAPBP actuator integrated in the airfoil and the airfoil shape change accompanied by its actuation. To overcome the nonlinear and hysteretic behavior of the SMA material, the application of an active position feedback system is also discussed. In the following a CFD model was developed to obtain the lift coefficient for the different actuation states of the airfoil. Wind tunnel experiments were used to investigate the behavior of the adaptive airfoil in a real life application.

4.1 Adaptive Airfoil Modeling and Design

The airfoil intended to prove the concept of a SMAPBP actuator actuated airfoil should have a chord length of 150 mm and a width of 100 mm. As a basis for the modeling of the airfoil, the NACA profile series was considered. The decision was made to use the NACA0012 profile because of the large amount of available research data for this airfoil. The symmetric airfoil was used because this thesis focused more on the capabilities of the actuator integrated in the airfoil then maximizing the aerodynamic performance (airfoil profile design). The coordinates of the NACA0012 airfoil were obtained by equation 4.1-1.[63]

$$y_{af} = \frac{t_{af}}{0.2} c_{af} \left[0.2969 \sqrt{\frac{x_{af}}{c_{af}}} - 0.1260 \left(\frac{x_{af}}{c_{af}} \right) - 0.3537 \left(\frac{x_{af}}{c_{af}} \right)^2 + 0.2843 \left(\frac{x_{af}}{c_{af}} \right)^3 - 0.1015 \left(\frac{x_{af}}{c_{af}} \right)^4 \right] \quad 4.1\text{-}1$$

A 150mm chord length was chosen for the design of the airfoil, which led to a maximum thickness of 18 mm. The maximum thickness occurred at a distance of 45 millimeter from the leading edge. It was then decided to use the first 60 mm of the profile as a D-spar composite leading edge and the last 90 mm was actuated length. This decision led to a 40% leading edge and 60% actuator distribution in respect to the overall length of the airfoil.

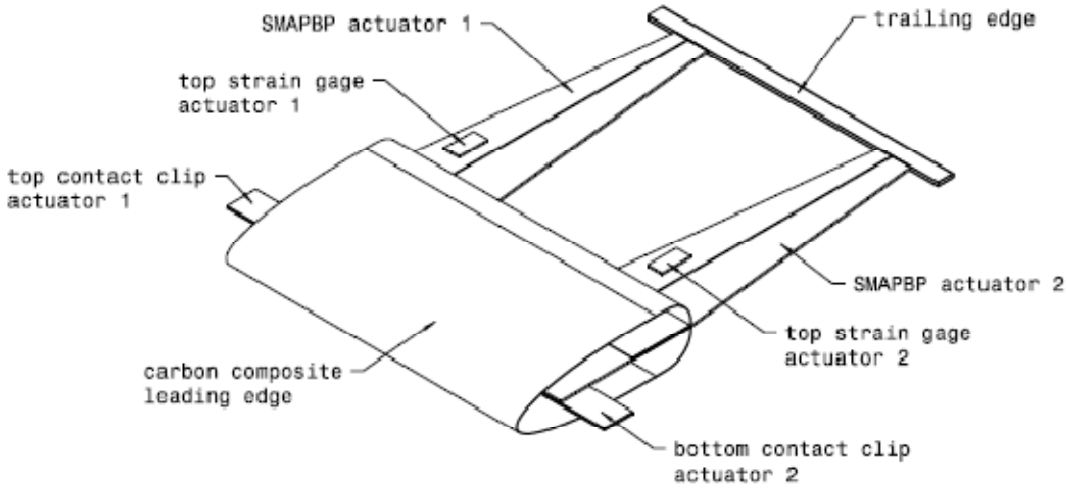

Figure 45: Drawing of Assembled Airfoil without Applied Skin

Figure 45 shows the assembly of the airfoil without the skin. The airfoil structure basically consisted of four main components; the carbon fiber composite leading edge, the actuators, the trailing edge and the elastic latex skin.

The leading edge was based on the shape of a NACA0012 airfoil with a chord length of 150 mm. The decision was made to build a leading edge with an overall length of 60 mm to provide at least some contour of the NACA0012 airfoil after the maximum thickness (at 48 mm). In order to obtain a smooth crossover between the leading edge contour and the straight skin to the trailing edge, a rounded edge was designed at the end of the leading edge. At a distance of 48mm from the leading edge a spleen was used to smoothen the crossover.

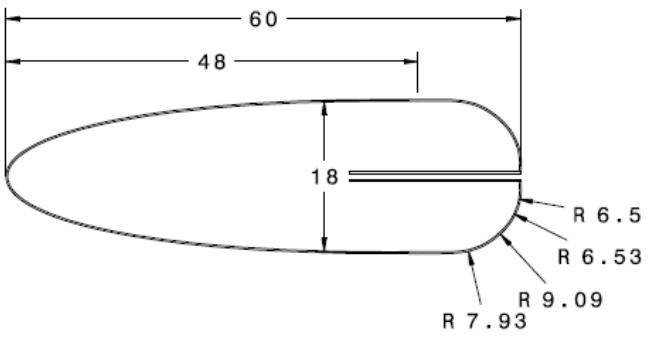

Figure 46: Cross-section of Leading Edge with Dimensions

The SMAPBP actuator was clamped and bonded to the inside of the leading edge at the ends of the carbon composite layer (between horizontal lines in Figure 46). This design approach made it possible to use the entire chord length of the airfoil more effectively because the clamping area of the actuator was integrated into the substructure of the leading edge and not behind the leading edge. This approach led to a higher actuated length and therefore larger trailing edge displacements.

The trailing edge consisted of a simple steel sheet that was bended 180°. The trailing edge had the only purpose to connect the two actuators and to obtain a fixture for the applied skin. The trailing edge had an overall length of 100 mm (similar to the width of the leading edge), a thickness of 0.127 mm and a width of 5 mm.

The skin had the purpose to give the airfoil a smooth surface and to apply the necessary buckling load to the SMAPBP actuator. The skin consisted of a 100 mm long and 40 mm wide latex tube.

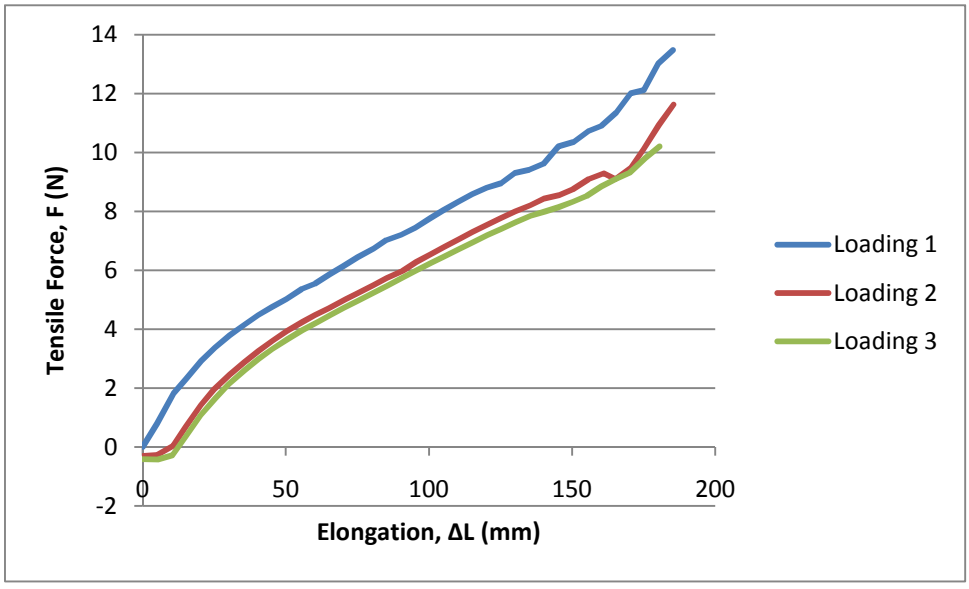

Figure 47: Tensile Measurements of Latex Skin

In order to obtain the load that was applied to the actuator from the skin, tensile measurements of the elastic latex skin were undertaken. The tensile load was applied perpendicular to the

length of the latex tube. Figure 47 shows the results of a tensile test of a 100 mm long and 40 mm wide specimen. The magnitude of the measurements decreases with increasing number of loading cycles. Based on the tensile tests an axial load of F_{askin} between 6 N and 8 N was assumed.

4.1.1 Geometry Change of the Actuated Airfoil

During actuation the whole appearance of the airfoil changes significantly. The leading edge can be seen as a fixed substructure, the trailing edge on the other hand can get displaced by the actuated actuator by a certain displacement. The elastic latex skin smoothens the transition between leading edge and trailing edge and obtains the airfoil's surface during actuation. This chapter covers the analytical approach necessary to capture the airfoil's shape change during actuation.

4.1.1.1 Displacement of Trailing Edge

To precisely capture the behavior of the airfoil during operating, obtaining lateral and vertical displacements of the trailing edge was important. To obtain this tip displacement a mathematical model was developed. For the model only the actuator was considered.

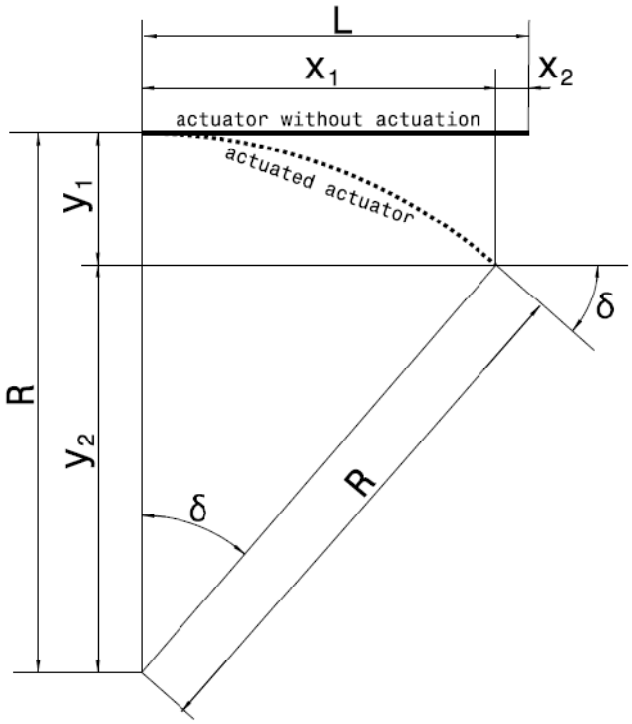

Figure 48: Nomenclature and Terminology for Tip Displacement of Airfoil

Due to the fact that the actuation force was only acting at the root and the tip of the actuator in one line and to simplify the process, the curvature (4.1-2) of the actuator was assumed constant over the length of the actuator.

$$\boldsymbol{\kappa = \frac{1}{R}} \qquad \text{4.1-2}$$

By considering a constant curvature, the bended actuator can be assumed as a part of a circle. This assumption enables the correlation between the angle of the partial circle δ (also tip displacement angle), the radius R and the length of the partial circumference, here the length of the actuator L. The following relationship could be obtained [64]:

$$R\delta = L \qquad \text{4.1-3}$$

The unit of the rotation angle δ was in radians in equation 4.1-3 and 4.1-4. Combining 4.1-2 and 4.1-3, the curvature of the actuator can be obtained with the known parameters L and δ:

$$\kappa = \frac{\delta}{L} \qquad \text{4.1-4}$$

The displacements of the trailing edge can now be easily determined by using trigonometric relationships:

$$x_1 = Rsin\delta = \frac{L}{\delta}sin\delta \qquad \text{4.1-5}$$

$$x_2 = L - x_1 = L - \frac{L}{\delta}sin\delta = L(1 - \frac{sin\delta}{\delta}) \qquad \text{4.1-6}$$

$$y_2 = Rcos\delta = \frac{L}{\delta}cos\delta \qquad \text{4.1-7}$$

$$y_1 = R - y_2 = \frac{L}{\delta} - \frac{L}{\delta}cos\delta = \frac{L}{\delta}(1 - cos\delta) \qquad \text{4.1-8}$$

For the CFD Model the displacements x_1 (4.1-5) and y_1 (4.1-8) are the important parameters. Using the actual data of the used SMAPBP actuator in the airfoil the displacements of the trailing edge shown in Figure 49 and Table 2 were obtained.

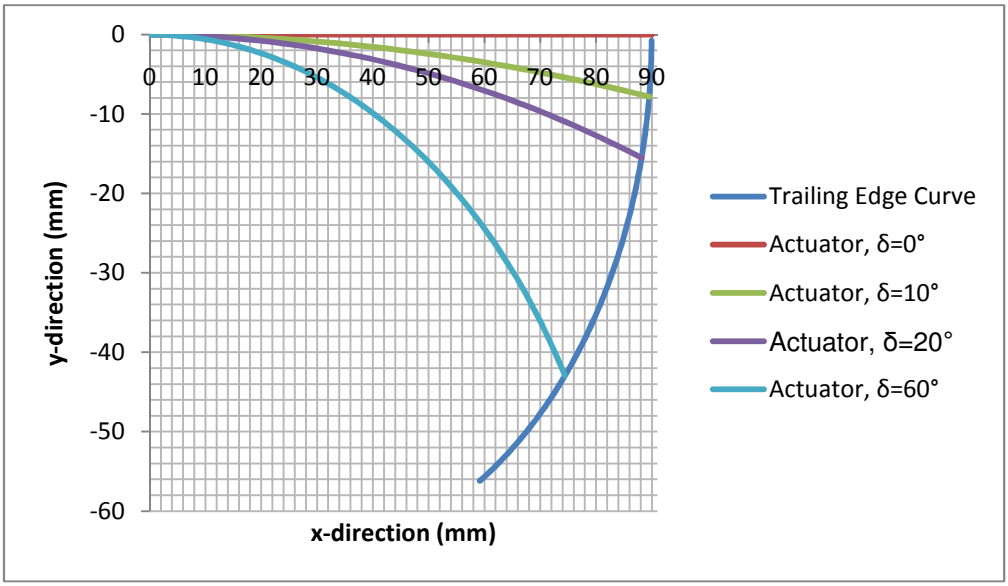

Figure 49: Displacement of Trailing Edge

Table 2: Trailing Edge Displacements due to Actuation

δ (°)	x1 (mm)	y1 (mm)	x2 (mm)	y2 (mm)	κ (1/mm)
0	**90**	**0**	0	oo	**0**
5	**89.886**	**3.924**	0.114	1027.4	**0.00097**
10	**89.544**	**7.834**	0.456	507.828	**0.001939**
15	**88.976**	**11.714**	1.025	332.061	**0.002909**
20	**88.183**	**15.549**	1.817	242.282	**0.003879**
25	**87.171**	**19.325**	2.829	186.939	**0.004848**
30	**85.944**	**23.029**	4.056	148.859	**0.005818**

By obtaining these displacements a more precise CFD model could be obtained.

4.1.1.2 Adaptive Geometry of airfoil

With the trailing edge displacements obtained in the previous chapter, the shape change of the entire airfoil was investigated in the following. The following figures show the entire airfoil with leading edge, actuator and skin for variable actuator tip rotation angles. The actuator tip rotation angles range from δ=0° up to δ=30° in 5° steps. In the following figures the leading edge is colored blue, the actuator is colored red and the skin is colored purple. For better clearness, the skin is only visible in case it is not adjacent to the substructure, the actuator itself or the trailing edge. Nevertheless the skin covers the whole outline of the airfoil.

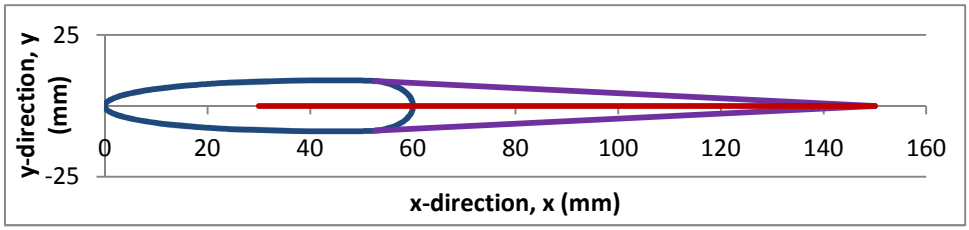

Figure 50: Airfoil Cross Section at δ=0°

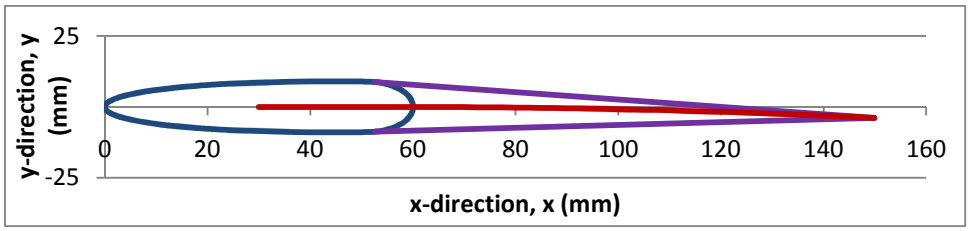

Figure 51: Airfoil Cross Section at δ=5°

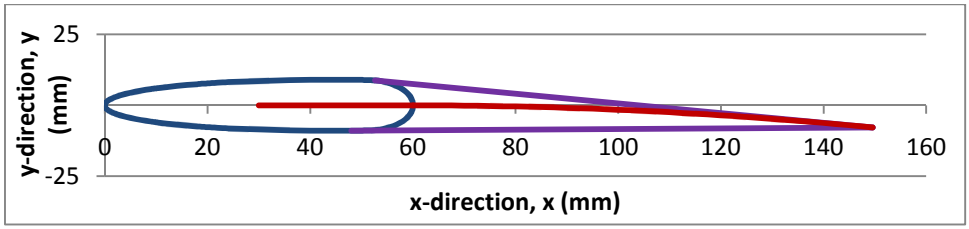

Figure 52: Airfoil Cross Section at δ=10°

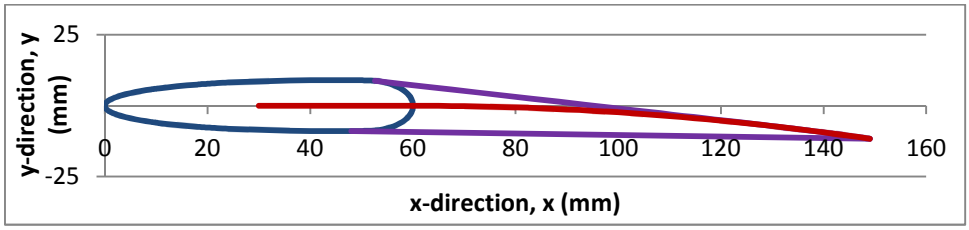

Figure 53: Airfoil Cross Section at δ=15°

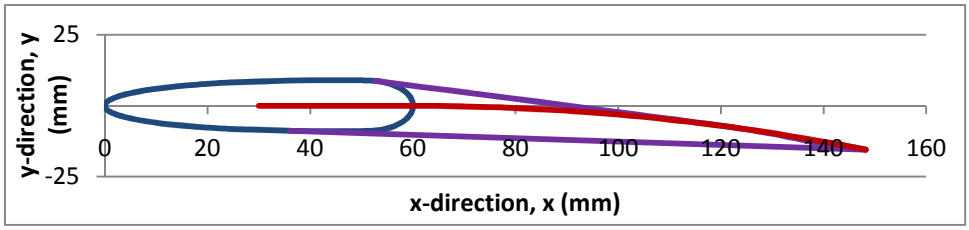

Figure 54: Airfoil Cross Section at δ=20°

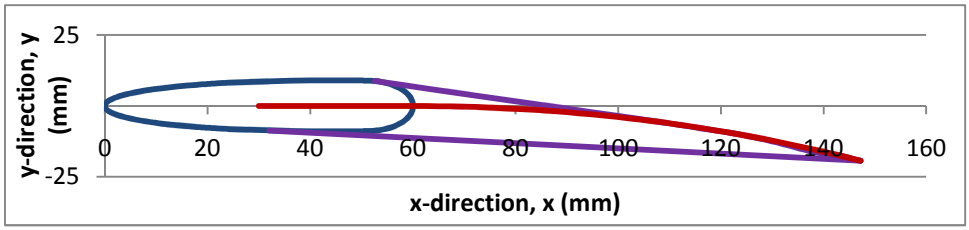

Figure 55: Airfoil Cross Section at δ=25°

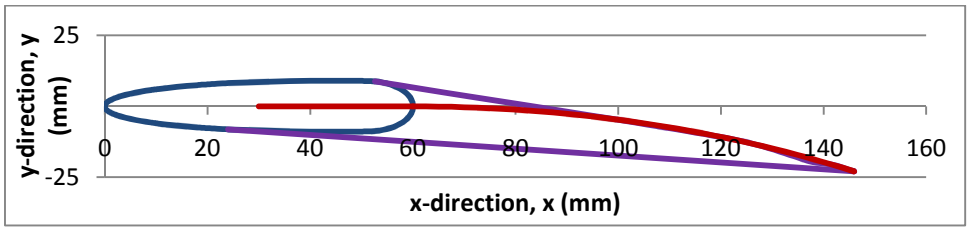

Figure 56: Airfoil Cross Section at δ=30°

4.1.2 Airfoil Manufacturing

The first step in the manufacturing of the airfoil was the manufacturing of the leading edge. As described above the leading edge had the purpose to take a vast bulk of the air loads and to hold the actuators in place. Furthermore it had to accommodate all the wires and cables of the actuator and the position feedback system. The most important role of the leading edge was to give the entire airfoil its characteristic aerodynamic shape. In order to manufacture the leading edge of the airfoil it was necessary to build a male tool first that had the shape and the dimensions of the finished end part. The male tool was manufactured out of pink foam and cut into the shape outlined in Figure 46. The pink foam tool was then taped with Kevlar tape to ensure an easy release of the finished part after curing. In the next step two layers of carbon fiber composite in wet layup were laid over the male part and cured for 24 hours at room temperature with the laminating epoxy (125 resin, 229 hardener; mixture ratio 100:30 by weight) from pro-set™.

Figure 57: From Left to Right: Pink Foam Tool, Female Tool and Leading Edge

Figure 57 shows the pink foam tool (left) that was used as a tool for the actual tool (middle). The actual tool consisted of three different parts; the upper and the lower composite part of the leading edge and an aluminum plate to obtain the clamping area for the actuators inside the finished part.

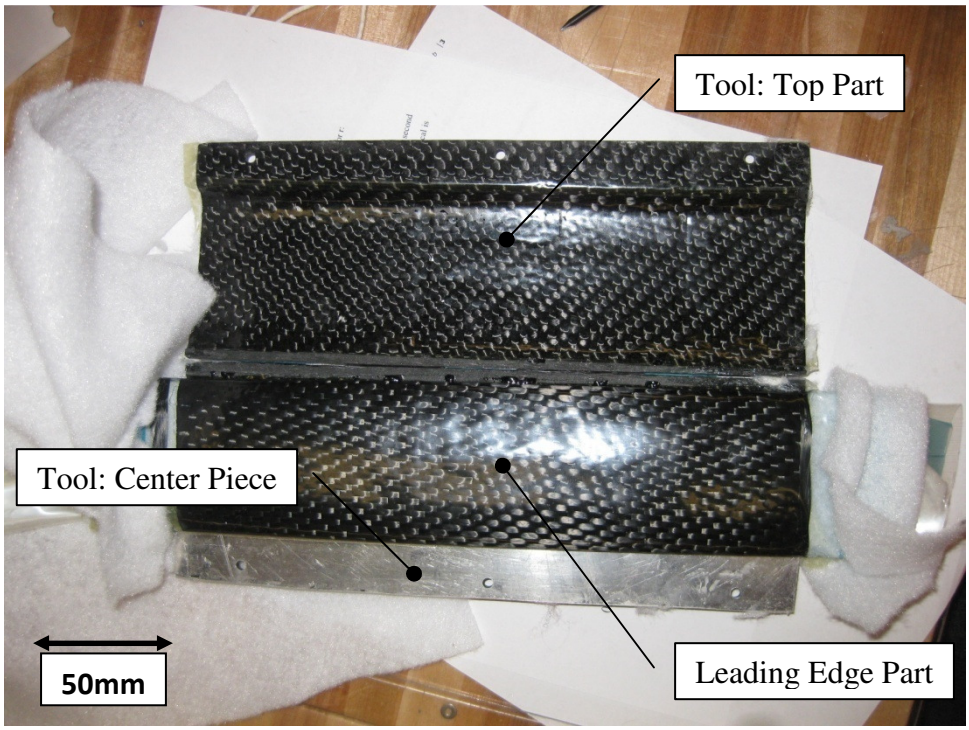

Figure 58: Leading Edge Part in Tool

For the layup of the leading edge part, a one layer thick carbon fiber cloth ply with wet layup was chosen. To ease the process of releasing the part from the tool, it was decided to layup the carbon cloth between two plastic release sheets and seal them with blue tape. This carbon fiber cloth epoxy release sheet was then wrapped tightly into the tool. Vacuum was applied to the inside and the outside of the part plus tool and checked for leaks. The part was then cured for 24 hours under vacuum and room temperature. Figure 58 shows the three parts of the tool with a cured leading edge part still in the tool. After removing the part from the tool and removing the plastic release foil from the composite structure, the leading edge was cut into a width of 100 mm.

The second big contributors to the airfoil were the actual actuators. The manufacturing of the actuators was described in detail in Chapter 4.1.2, so there is no need to describe it again. Two actuators were used in this 100 mm wide airfoil. The actuators were aligned to the sides of the leading edge which led to a distance of 40 mm between the actuators. The actuators were bonded inside the leading edge with Hysool, put under pressure and cured for 24 hours under room temperature. In the following strain gages of the active position feedback system were bonded to both actuators, this process is explained in detail in Chapter 4.2.1.1.

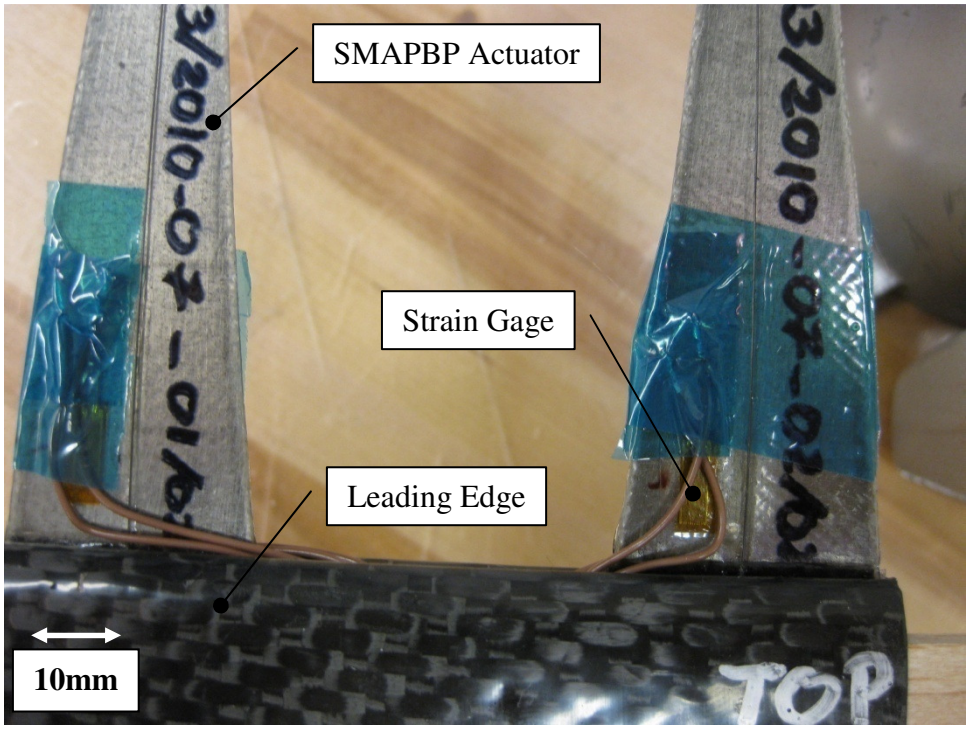

Figure 59: Applied Strain Gages with Connection Wires

In the next step the trailing edge was attached to the tip of the actuators. The trailing edge was just a folded piece of stainless steel of 100 mm length and 5 mm width with a stiffness high enough to withstand any bending in order to provide a straight trailing edge at all time. The attachment of the trailing edge was through friction fit to ensure easy maintainability and control of each of the actuators.

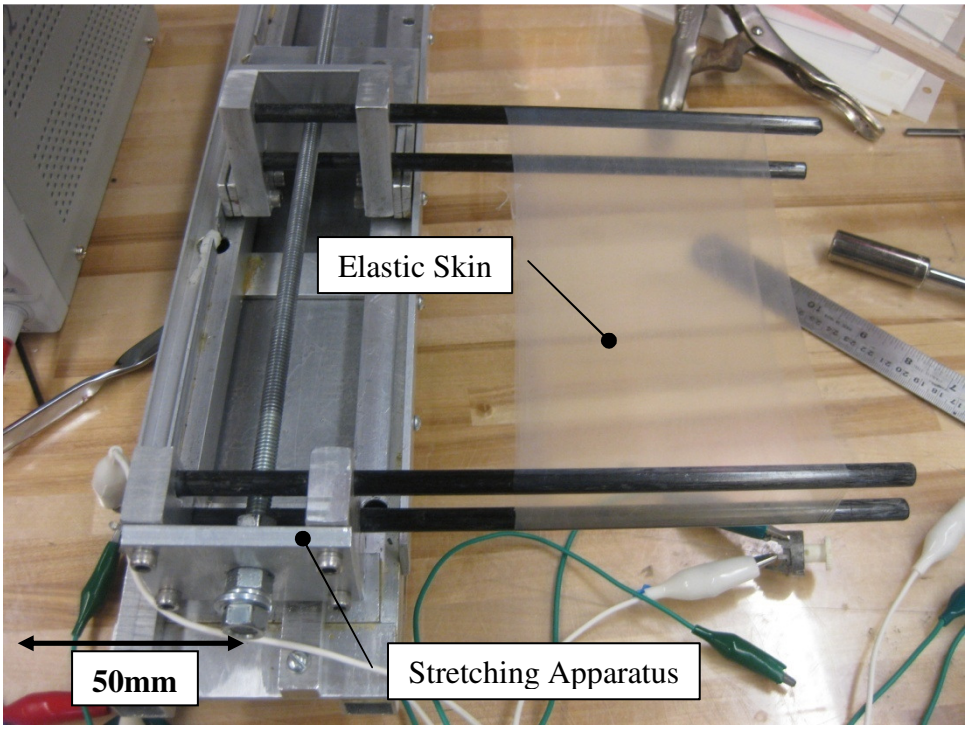

Figure 60: Stretching of the Skin

Figure 60 shows the stretching of the elastic latex skin. The skin was stretched to a length of 180 mm three times before it was applied to the airfoil to obtain a consistent buckling force over the entire lifetime of the skin and airfoil. The airfoil was inserted into the stretching apparatus and by decreasing the pretension of the stretching apparatus the skin laid against the leading and trailing edge and completed the airfoil.

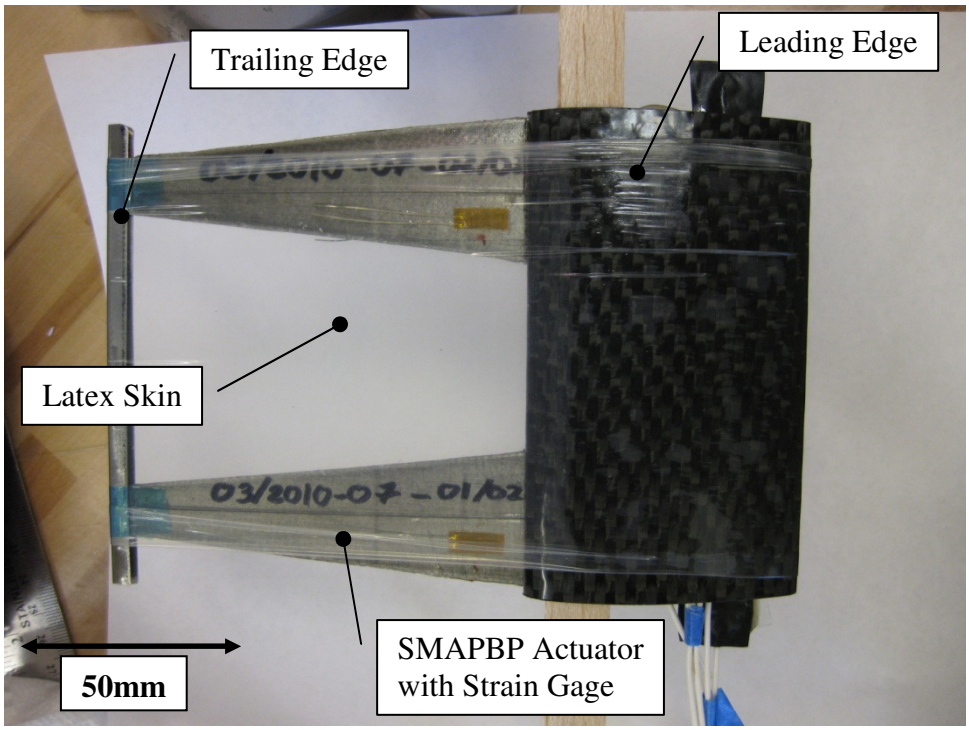

Figure 61: Airfoil with Applied Elastic Skin

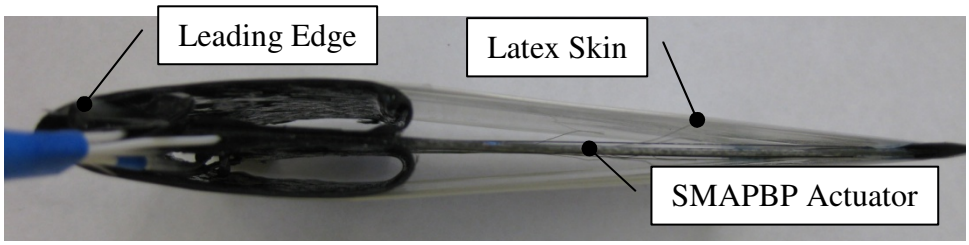

Figure 62: Side View of Airfoil with Applied Elastic Skin

Figure 62 and Figure 65 are showing the assembled airfoil, only the wires for the strain gages are missing in these two images. Figure 65 gives a good side view of the cross section of the airfoil with no actuation. It can be seen that the leading edge gives the airfoil the basic shape and that the tip of the actuators serves as a trailing edge. The applied latex skin gives the airfoil the familiar aerodynamic shape.

4.2 Active Position Feedback System Architecture

Due to the highly hysteretic and nonlinear behavior of the shape memory alloy actuator, it was necessary to introduce an active position feedback system to the airfoil. The control system had the function to control the tip displacement over the applied actuator current. Different concepts for the feedback system were considered and the decision fell on using strain gages to measure the variation of strain on the surface of the actuator. The strain on the surface correlates directly to the curvature of the actuator and therefore to the tip rotation angle. Figure 63 shows the principle architecture of the active position feedback system proposed for the airfoil. The figure shows the principle of an intelligent structure. An intelligent structures basically consist of three main parts; a sensor, an actuator and a controller. For the proposed airfoil the sensor is the strain gage plus Wheatstone bridge (blue arrows), the actuator is the actual SMAPBP actuator with current amplifier (red arrows) and the controller which is the control routine developed in Labview®.

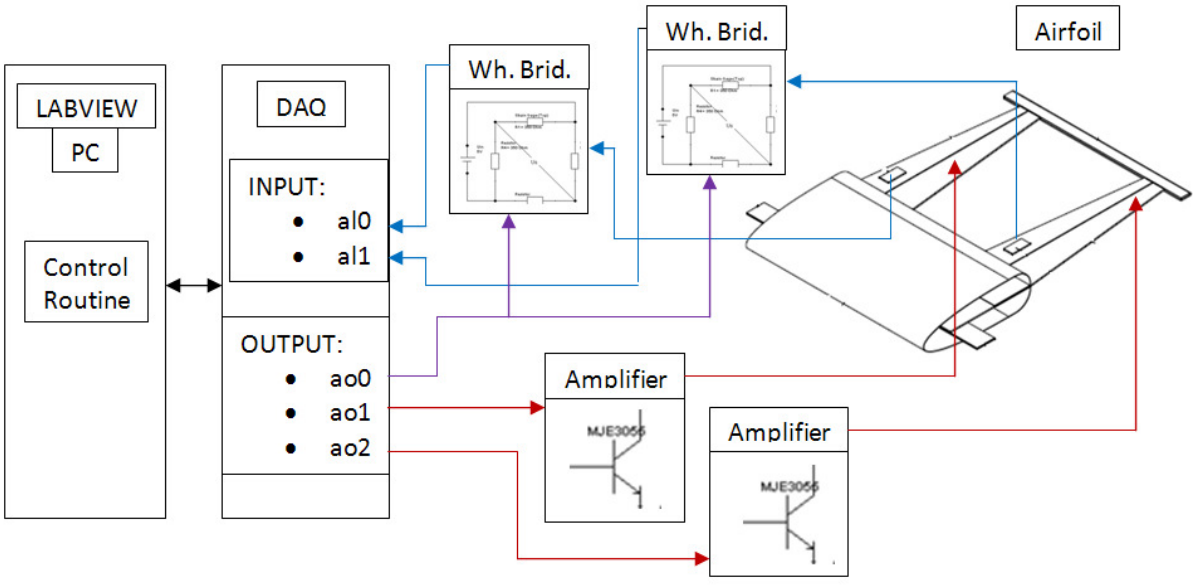

Figure 63: Position Feedback System Architecture

By displacing the trailing edge, the resistance of the strain gages applied to the actuators changed and therefore its voltage level. The sensor (strain gage plus Wheatstone bridge) senses a change in voltage that was then red into the analog input channels of the data

acquisition system (DAQ (National Instruments NI USB-6251)). For the two actuators two channels were needed (analog input channel aI0 and aI1). The DAQ system was connected over a USB port to a personal computer with Labview® application. Labview® was used to write the actual control routine to obtain a specific trailing edge displacement. The control routine in Labview® is described later in this chapter (Chapter 4.2.2). The control system in Labview® will provide the DAQ with three voltage output channels; one channel has a constant value of 5 V and serves as the external power supply necessary for the Wheatstone bridge. The other two channels are the outlets to the two actuators; the outlets are controlled by the control routine.

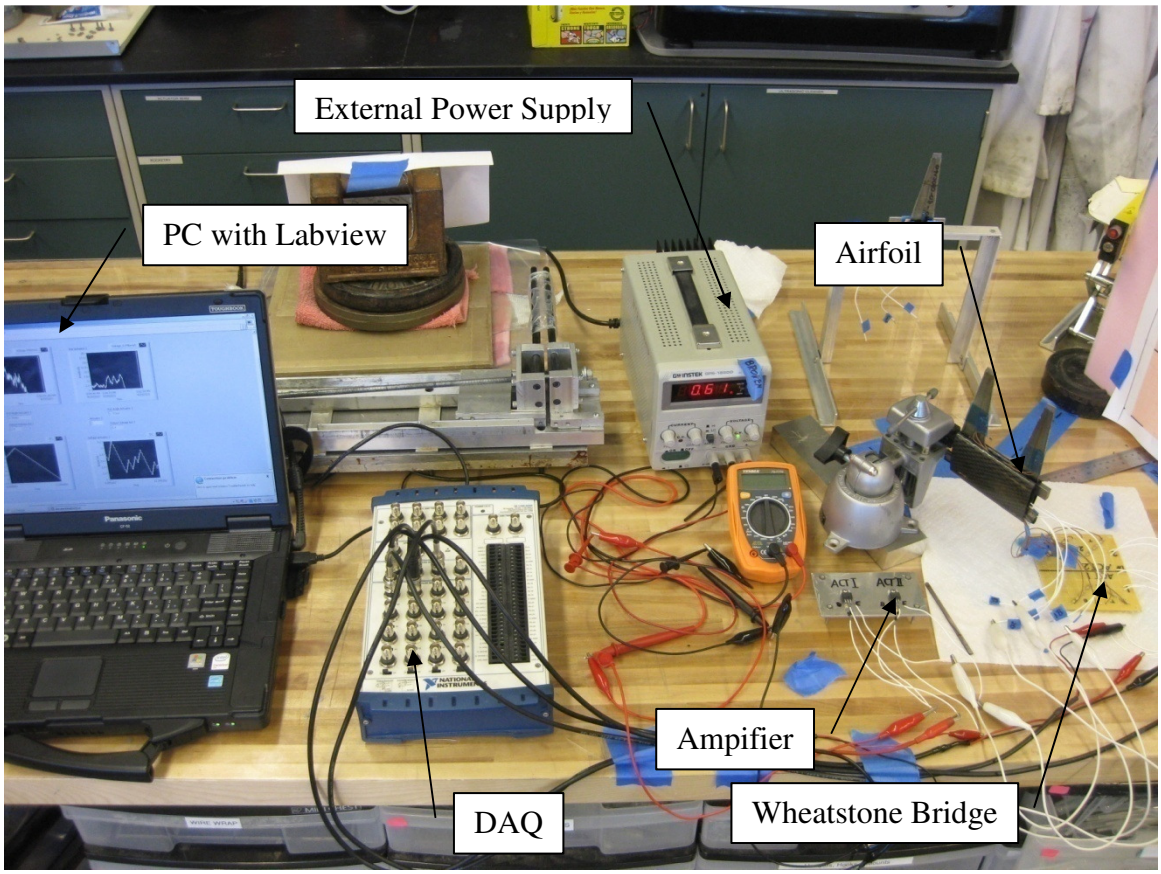

Figure 64: Picture of Experimental Setup for Position Feedback System

Due to the fact that Labview® only provides a variable voltage output and that a variable current level was needed to actuate the actuator's SMA wires, a current amplifier needed to be interposed. With this simple position feedback loop it was possible to overcome the nonlinear

hysteretic behavior of the SMA wire and made it possible to command the trailing edge of the airfoil to a specific predetermined displacement. In the following each of the different subsystem of the whole active feedback system will be described more in detail. The three main parts of the control system are the strain gage applied to the actuator and it's Wheatstone bridge, the control routine in Labview® and the amplifier system which actuates the actuators.

4.2.1 Sensor - Strain Gage

The first part of the active position feedback system was the strain gage that served as the sensor in this system. Due to the fact that Labview® couldn't provide a voltage at the input channels of the DAQ, a Wheatstone bridge with external excitation voltage needed to be applied to the strain gages.

4.2.1.1 Application on Airfoil

The strain gages were attached close to the root of the actuator, just off actuator centerline. The small offset to the centerline was necessary to neglect the effect of the heating of the SMA wire during actuation. Figure 65 shows the application of the top strain gage on one of the actuators. Laminating epoxy from Pro-Set with 125 resin and 229 hardener was used to attach the strain gages on top and bottom side of the actuator. A technical note from VISHAY™ recommends using the same epoxy that was used in the layup of the substructure composite to lock down the strain gage.[65]

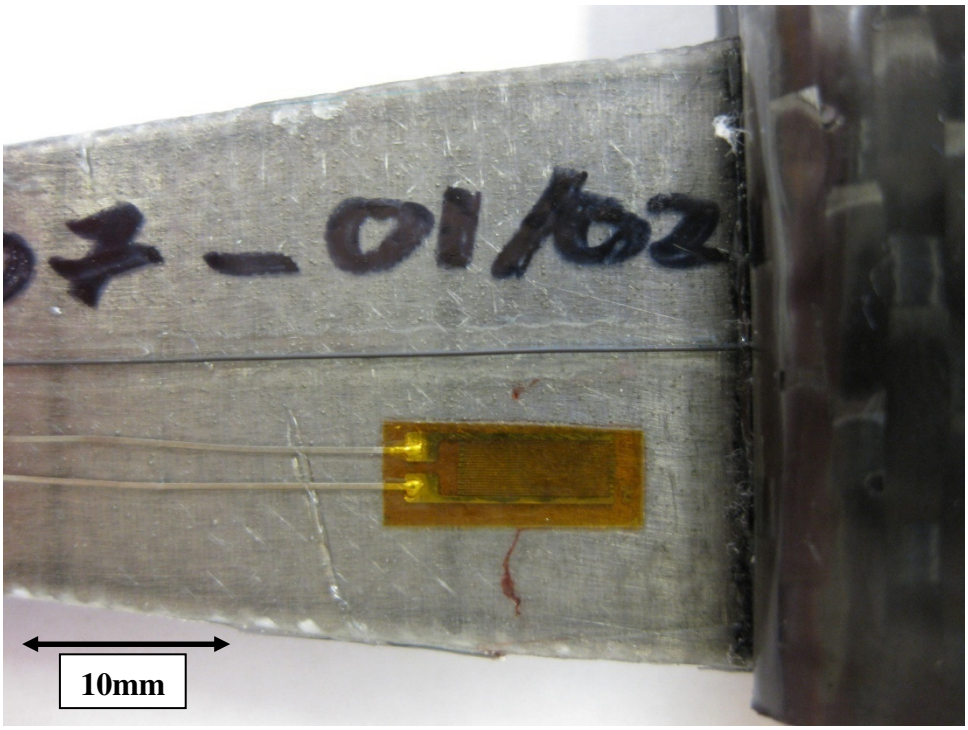

Figure 65: Strain Gage Application on Actuator

Two strain gages were attached on each actuator, one on the top surface, one on the bottom surface to account for thermal expansion.[66]

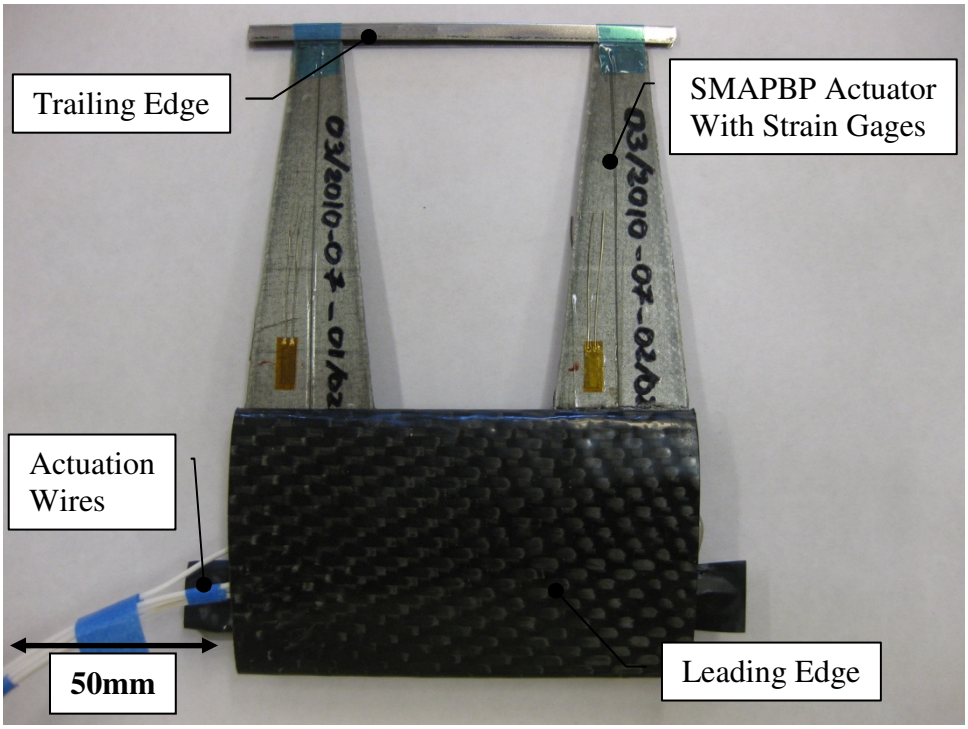

Figure 66: Strain Gage Application on Airfoil

4.2.1.2 Wheatstone Bridge

As mentioned above, the Labview® input channels of the DAQ were not providing any voltage to excite a strain gage, therefore a Wheatstone bridge with an external excitation power source needed to be applied. A half-bridge Wheatstone bridge configuration was chosen to obtain the strain of the two strain gages. The strain gages applied to the actuator are from OMEGA, with a serial number SGD-7/350-DY13 and a resistance of 350 Ω and gage factor of 2.02. Figure 86 shows the Wheatstone bridge used to obtain the strain/voltage change for one actuator. To obtain a feedback system for the whole wing section with two actuators, two Wheatstone bridges needed to be built.

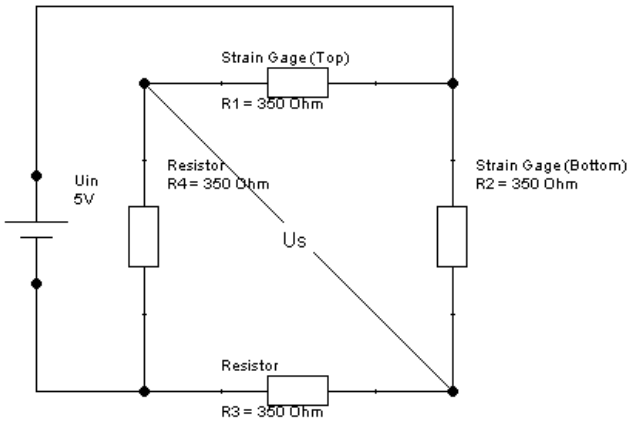

Figure 67: Wheatstone Bridge to Obtain Surface Strain for one Actuator

The voltage across the Wheatstone bridge could be calculated using the following equation [66]:

$$U_s = \frac{\frac{R_1}{R_2}}{\left(1+\frac{R_1}{R_2}\right)^2}\left(-\frac{\Delta R_1}{R_1}+\frac{\Delta R_2}{R_2}-\frac{\Delta R_3}{R_3}+\frac{\Delta R_4}{R_4}\right)U_{in} \qquad 4.2\text{-}1$$

For the Wheatstone bridge shown in Figure 67 the equation 4.2-1 can be simplified by assuming that the resistors will not change their resistance and therefore ΔR_3 and ΔR_4 are equal to zero. Furthermore it can be said that the resistance of the two strain gages R_1 and R_2 are equally 350 Ω. Therefore equation 4.2-1 can be simplified to:

$$U_s = \frac{1}{4}\left(-\frac{\Delta R_1}{R_1} + \frac{\Delta R_2}{R_2}\right) U_{in} \qquad 4.2\text{-}2$$

By considering that the relationship between change in resistance and change of strain are directly related to each other by a constant, the gage factor S_G:

$$\frac{\Delta R}{R} = S_G \varepsilon \qquad 4.2\text{-}3$$

In case that the actuator was displaced downwards the strain at the top surface was positive and the strain at the lower surface of the actuator was negative. By combining equation 4.2-2 and 4.2-3 the following relationship can be obtained:

$$U_s = \frac{1}{4}(-2S_G \varepsilon) U_{in} \qquad 4.2\text{-}4$$

$$\varepsilon = -\frac{2U_s}{S_G U_{in}} \qquad 4.2\text{-}5$$

The measured output of the Wheatstone bridge was a change of voltage level proportional to the strain at the strain gage. The input voltage for the Wheatstone bridge was provided by a Labview output channel to U_{in}=5 V. Due to the fact that the strain at the strain gage is proportional to the curvature of the actuator which is also proportional to the tip displacement angle, the measured voltage change of the Wheatstone bridge is directly proportional to tip rotation angle due to actuator actuation.

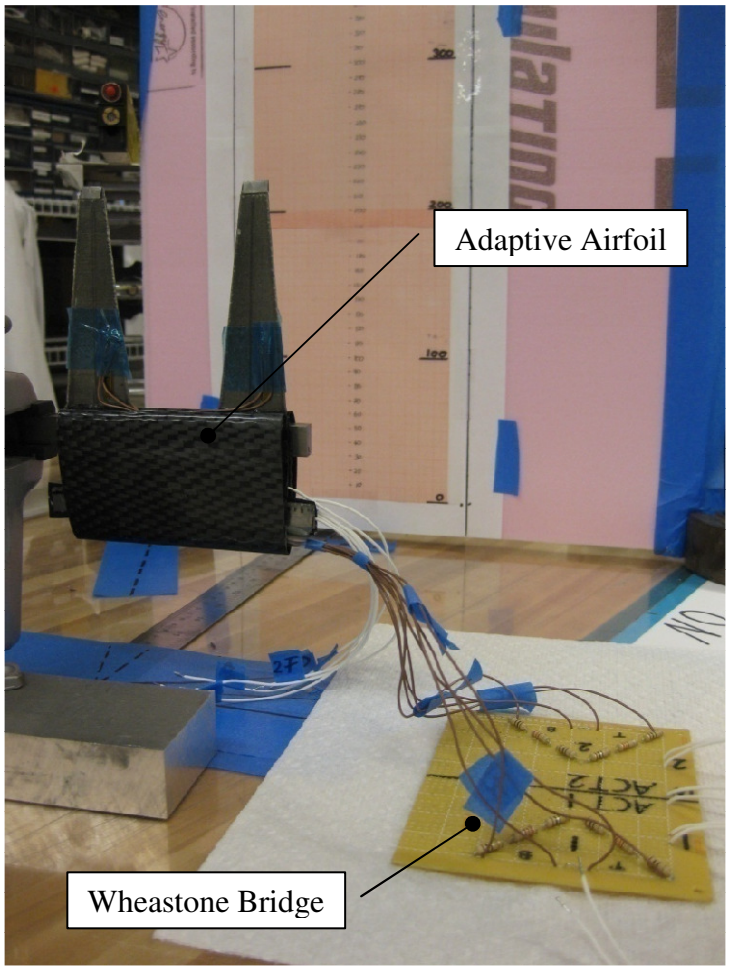

Figure 68: Airfoil with Wheatstone Bride Circuit Board

4.2.2 Controller - Control Routine in Labview®

The control routine implemented in Labview® was the core of the entire position feedback system. The program served the purpose to compare the actual value to the desired value of the tip rotation angle. The control routine received an input voltage from the strain gages on the actuators and it provided an output voltage to the current amplifier which actuated the actuators.

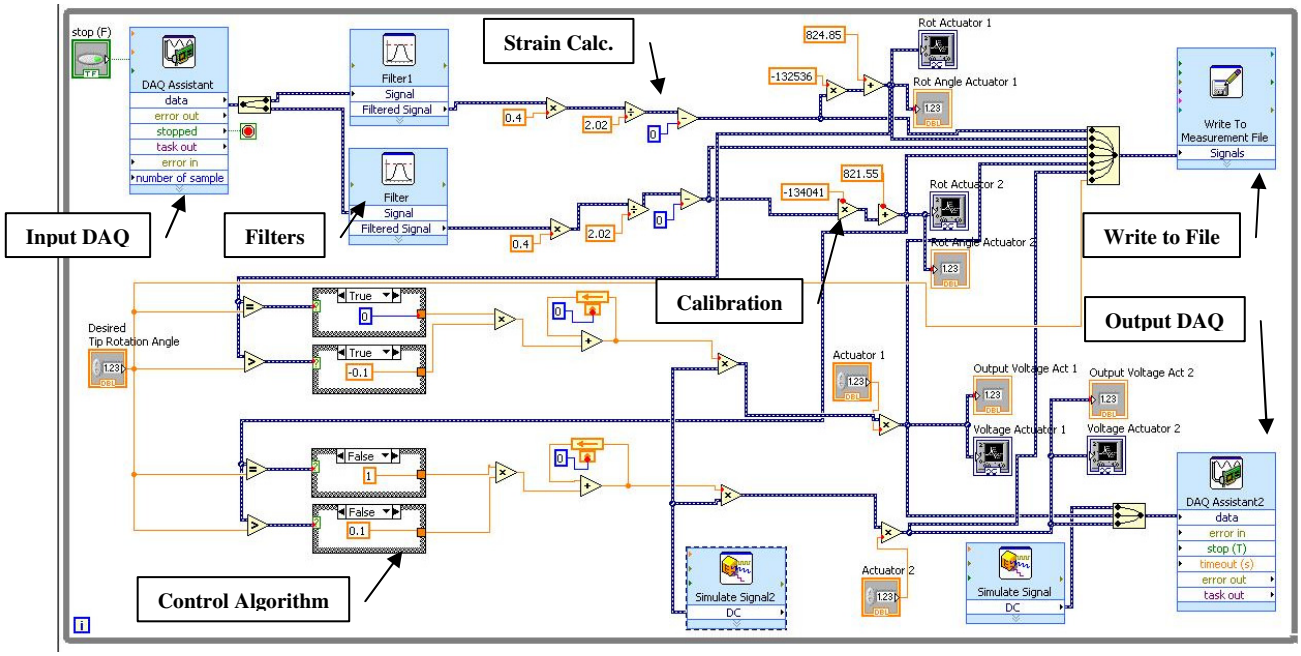

Figure 69: Labview Block Diagram for Control Program

The block diagram for the entire control routine is shown in Figure 72. The Input DAQ received a voltage signal from the Wheatstone bridge with the strain gages applied on the actuators. The voltage signals (two voltage signals; one for each actuator) were red in a sample rate of 100 Hertz. A voltage range between -5 V and +5 V was expected because of the set excitation voltage of the Wheatstone bridge of 5 V (Simulate Signal, lower right corner Figure 72). In the following the signals were smoothened by a Filter with rectangular moving average smoothing with 100 half-width moving average. The voltage signals were then converted into a strain signal and transformed into tip rotation angle by using the calibration parameters/curves described by the calibration obtained in Chapter 4.2.2.1. These transformations provided the actual value of the tip rotation angle that was needed for the control loop routine.

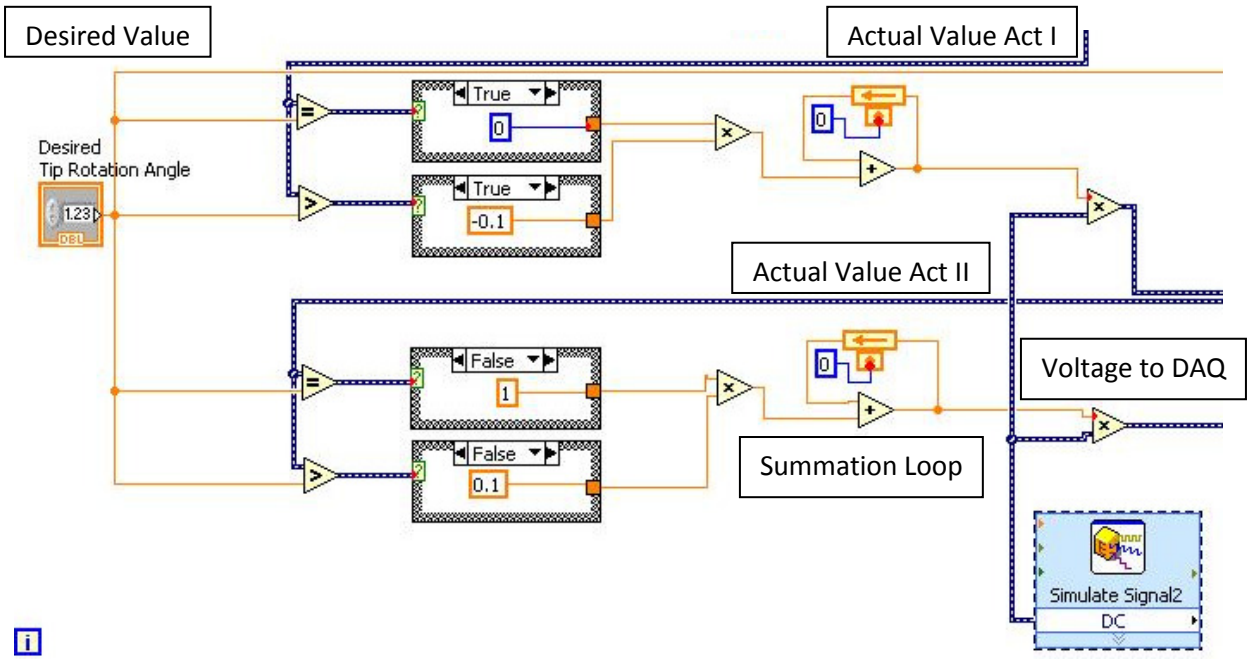

Figure 70: Block Diagram of Control Loop in Control Routine

Labview® provided only simple programming tools. A simple case structure was selected with a summation loop to solve the control problem. For the case that the actual value and the desired value are exactly the same the summand was multiplied by zero. If the values were not the same the summand was multiplied by one and the summation loop went on. In case that the actual value was bigger than the desired value the summand was set to -0.1, in case it was bigger it was set to +0.1. The summation loop therefore obtained a factor that was multiplied by a voltage obtained by the DC Simulate Signal2. The voltage obtained by the DC Simulate Signal2 was set to a constant value of 1 V. By this multiplication an output current for the DAQ output was obtained for the current amplifier.

The strains from the strain gages, the actual actuator tip rotation angles, the desired tip rotation and the output voltage level were written in a file for documentation purposes.

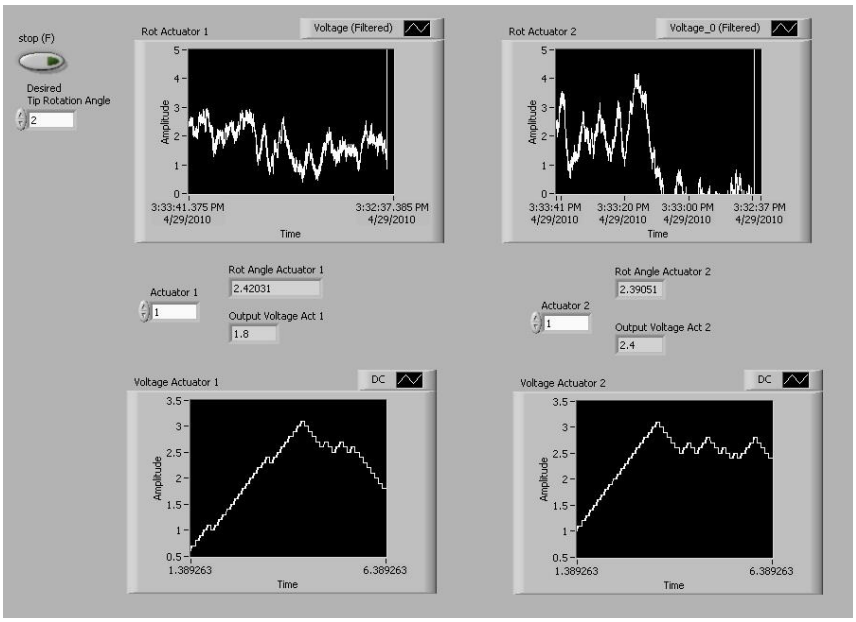

Figure 71: Front Panel of Labview® Control Routine

Figure 71 shows a screenshot of the Labview® front panel of the control routine application. On the top are the two graphs for the actual tip rotation angle measured by the strain gages (left: actuator 1, right: actuator 2), the lower part are the two graphs for the output voltage (left: actuator 1, right: actuator 2). The desired tip rotation angle could be typed into the field in the upper left corner. A numeric indicator for each of the values from the graphs was provided between the tip rotation graphs and the output voltage graphs to read the values more precisely.

4.2.2.1 Feedback System Calibration

The strain gages applied to the actuators are providing the control software with a variable voltage U_s proportional to the actuator tip displacement of the actuator. The strain of the strain gages was calculated by using the equation developed above:

$$\varepsilon = -\frac{2U_s}{S_G U_{in}} \qquad 4.2\text{-}6$$

In order to develop a relationship between the measured strain at the actuator and the actual tip rotation angle, the feedback system needed to be calibrated.

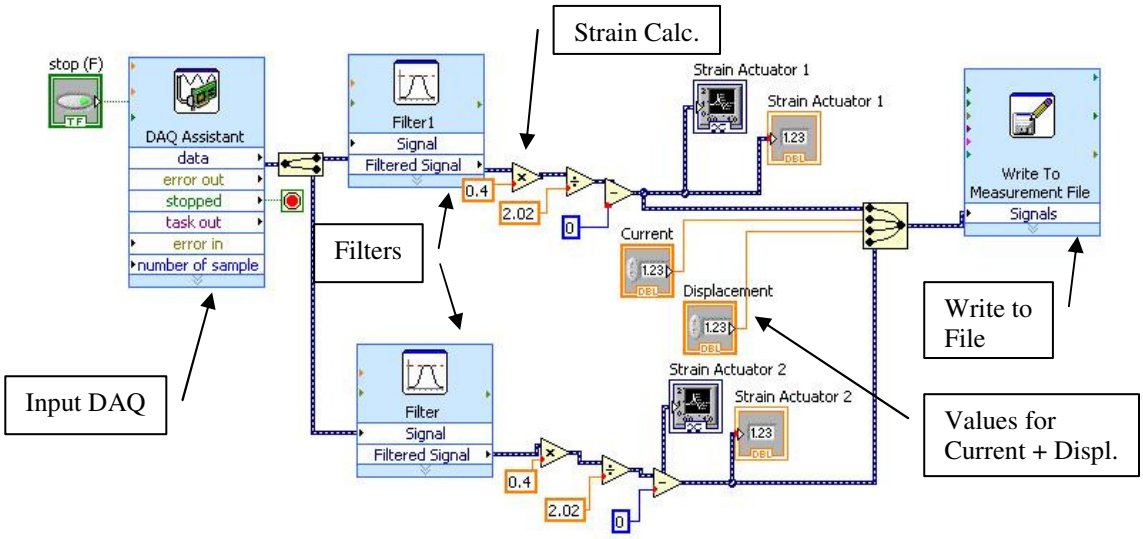

Figure 72: Labview Block Diagram for Feedback Loop Calibration

Figure 72 shows the principle architecture of the calibration routine from Labview®. The DAQ to the left red the voltage input values from the Wheatstone bridge. The two voltage signals were smoothened by a low pass filter. The voltage signal was then transformed into a strain signal with the equation developed above. The two strain signals together with the measured values of current and actuator tip rotation angle (displacement) were then written into a file and analyzed in order to obtain the calibration curves.

The strain of the strain gage and the tip rotation angle were measured simultaneously and plot against each other in a diagram. Each actuator needed a calibration curve of its own because of possible discrepancies in the actuator manufacturing or strain gage application. The calibration curves can be seen in Figure 73 for SMAPBP actuator 1 and in Figure 74 for SMAPBP actuator 2.

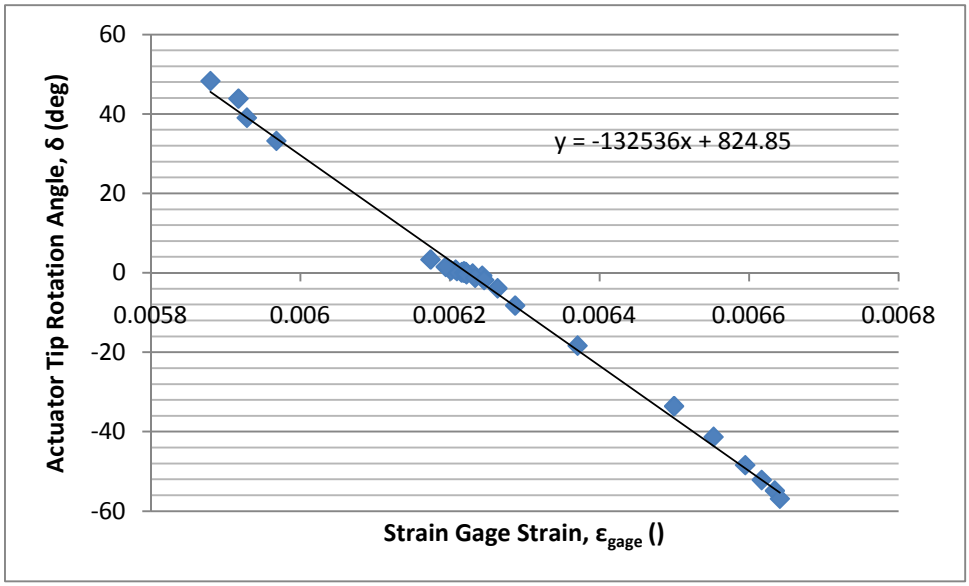

Figure 73: Calibration Curve Actuator 1

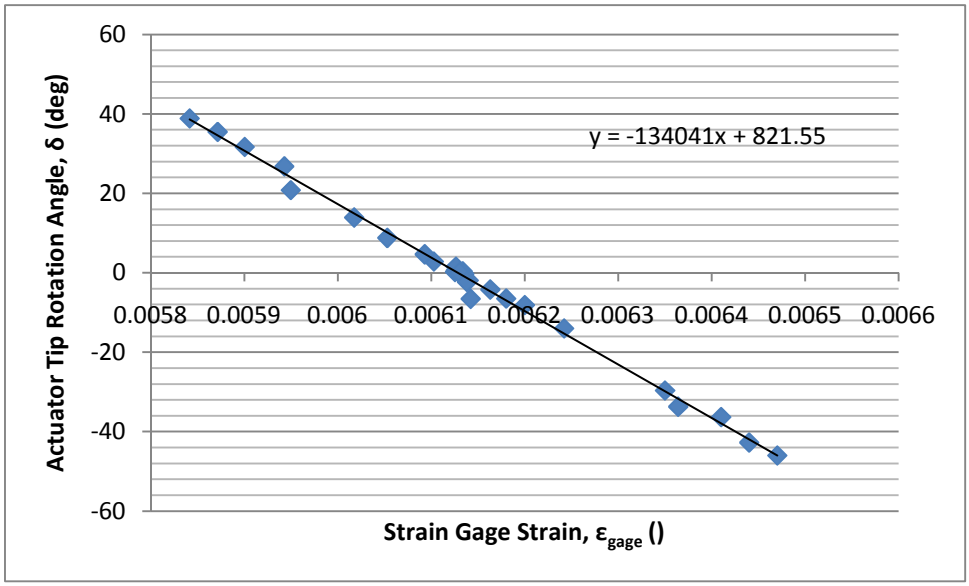

Figure 74: Calibration Curve Actuator 2

A linear approximation curve was laid over the measured points in order to obtain a calibration curve. The tables in Appendix A show that the approximation curve obtains close values to the actual measured actuator tip rotation angles. The following two equations were obtained by the linear approximation curves and were employed in the control routine.

Actuator 1: $$\delta_{\text{Act }1}(\varepsilon_{\text{gage1}}) = -132536°(\varepsilon_{\text{gage1}}) + 824.85° \quad \text{4.2-7}$$

Actuator 2: $$\delta_{\text{Act }2}(\varepsilon_{\text{gage2}}) = -134041°(\varepsilon_{\text{gage2}}) + 821.55° \quad \text{4.2-8}$$

With these two calibration equations it was achievable to develop a control routine for the active position feedback system.

4.2.3 Actuator - Current Amplifier & SMAPBP Actuator

Due to the fact that Lab view and the Data Acquisition System (DAQ) were only providing a variable voltage output with a maximum output voltage of 10V and a constant current, it was necessary to build a current amplifier (Figure 75). Former experiments showed that the SMA wire of the actuator will be actuated by a change in current level and not by a change in voltage level. The decision for the use of the MJE3055T[67] transistor was made because of its emitter-base voltage of 5V and its current gain that ranges from 20 to 100.

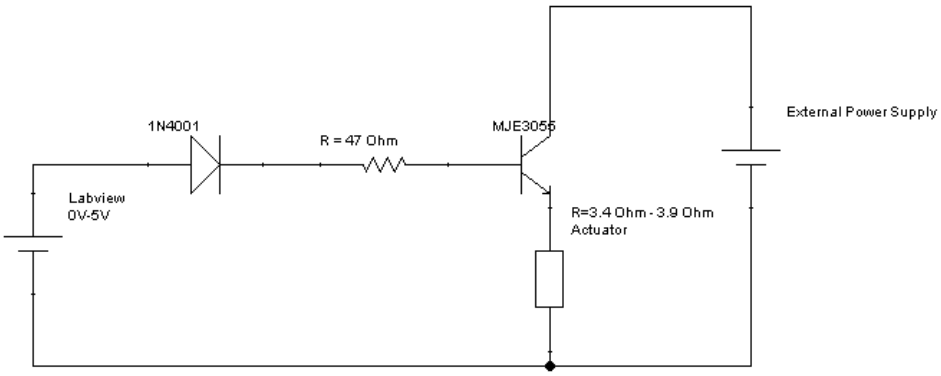

Figure 75: Current Amplifier with Actuator at Emitter

The amplifier circuit from Figure 75 needed to be expanded to actuate both sides of the actuator. Because of this reason it was necessary to have two of these amplification circuits for each actuator. For the whole airfoil with two SMAPBP actuators a number of four amplifiers was necessary.

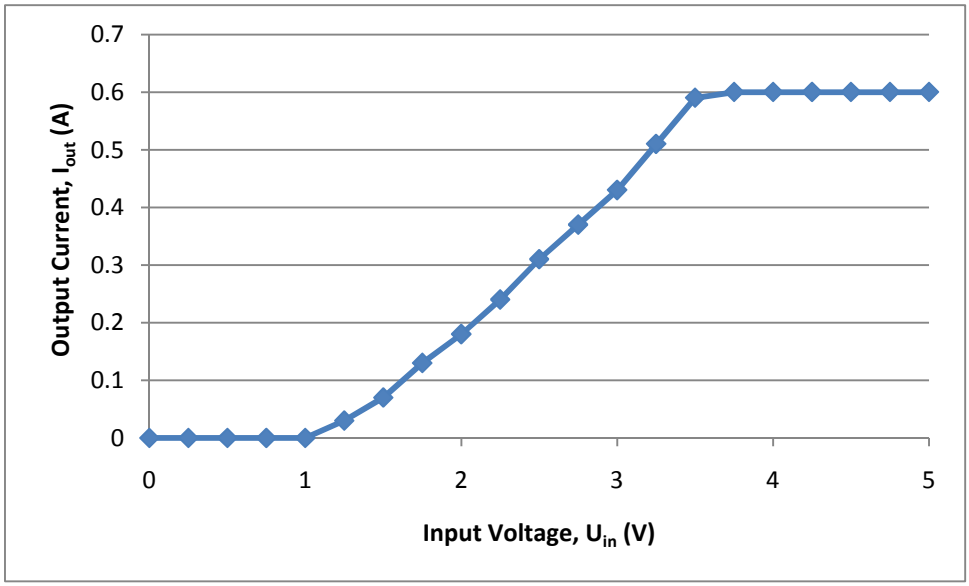

Figure 76: Performance of Amplifier Circuit

Figure 76 shows the performance of the amplifier circuit with an applied input voltage between base and emitter of the transistor and an output current between collector and emitter. The current amplifier described above showed a linear behavior between U_{in}=1 V and U_{in}=3.5 V. The threshold voltage of the diode at the base of the exciter may be the cause of the zero output current between 0 V and 1 V input voltage. There was no need for the input voltage and output current to be linear for but it made the controllability and adjustment easier and more stable.

During operation the transistor in the amplifier circuit reached temperatures in access of 120°C. To prevent the transistor from destruction, the decision was made to attach the transistors to a 100 mm wide and 60 mm long thick metallic plate. The metallic plate served as a heat conductor to conduct the heat away from the transistors and increase the cooling surface by up to 10 magnitudes. By increasing the cooling surface and allowing an air flow over and under the plate, the temperature of the transistors could be decreased to 45°C.

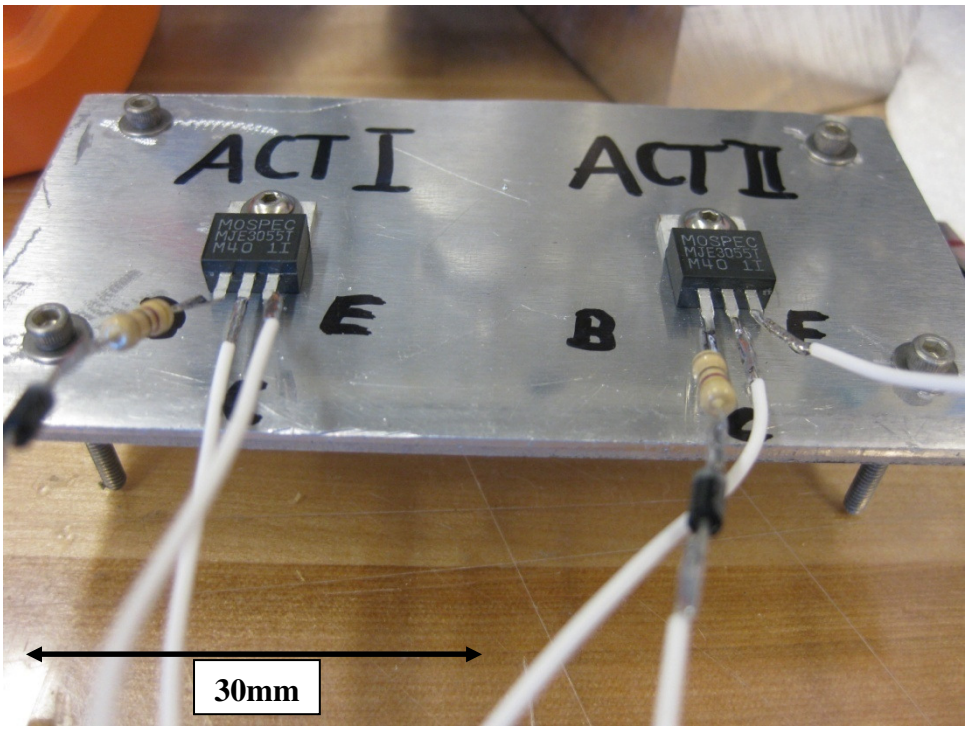

Figure 77: Transistor Amplifier with Cooling Plate

4.3 CFD Model

4.3.1 Operating Condition Assumptions

In order to obtain a CFD model and wind tunnel test some basic operating conditions needed to be set. An application of this airfoil with a chord length of 150 millimeters can be envisioned in small UAVs, such as the Raven RQ-11 developed by AeroVironment in 2002. The Raven RQ-11 is a remote or GPS controlled Miniature Unmanned Aerial Vehicle (MUAV) used by the U.S. Army, the US Marines, and the US Air Force. The Raven RQ-11 is also used by militaries from Australia, Czech Republic, Denmark, Spain, Iraq, Italy, Lebanon, Netherlands and the United Kingdom.[68] Because of this broad band of usage of the Raven RQ-11 MUAV and its similar dimensions to the proposed airfoil, the Raven RQ-11 cruising speed and operation altitude were used for the CFD model and the wind tunnel tests. The Raven RQ-11 has a wing span of 1.4m, a weight of 1.9kg and an operating speed between 32 km/h (8.89 m/s) – 81 km/hr (22.5 m/s).[69] To account for any uncertainties during flight the free stream velocity to the airfoil was assumed to be $v_{freestream}$=25m/s. The Raven RQ-11 operates at an altitude from 30 m to 152 m. Because of this low operation altitude and to simplify the analyses, an operation altitude at sea level standard condition was assumed. With an operating temperature of T_t=20°C (293.15K) the absolute pressure was assumed be P_t=101,325 Pa for sea level conditions that leads to a air density of ρ_{air}=1.2041 kg/m^3.[70]

4.3.1.1 Computational Mythology

The computer used for these calculations was located in the design lab (Room 3101) in Learned Hall at the University of Kansas, Lawrence. The Computer had an Intel® Pentium® 4 CPU with 3.40 GHz and 2.00 GB RAM. GAMBIT® 2.2.30 was used for mesh generation and FLUENT® 6.2.16 was used for the flow calculation and the development of the contours.

4.3.2 Geometry and Mesh Generation

4.3.2.1 CFD Geometry of Actuated Airfoil

By using the dimensions of the airfoil obtained in Chapter 4.1.1 the geometry of the adaptive airfoil during actuation could be created in GAMBIT (see Figure 78).

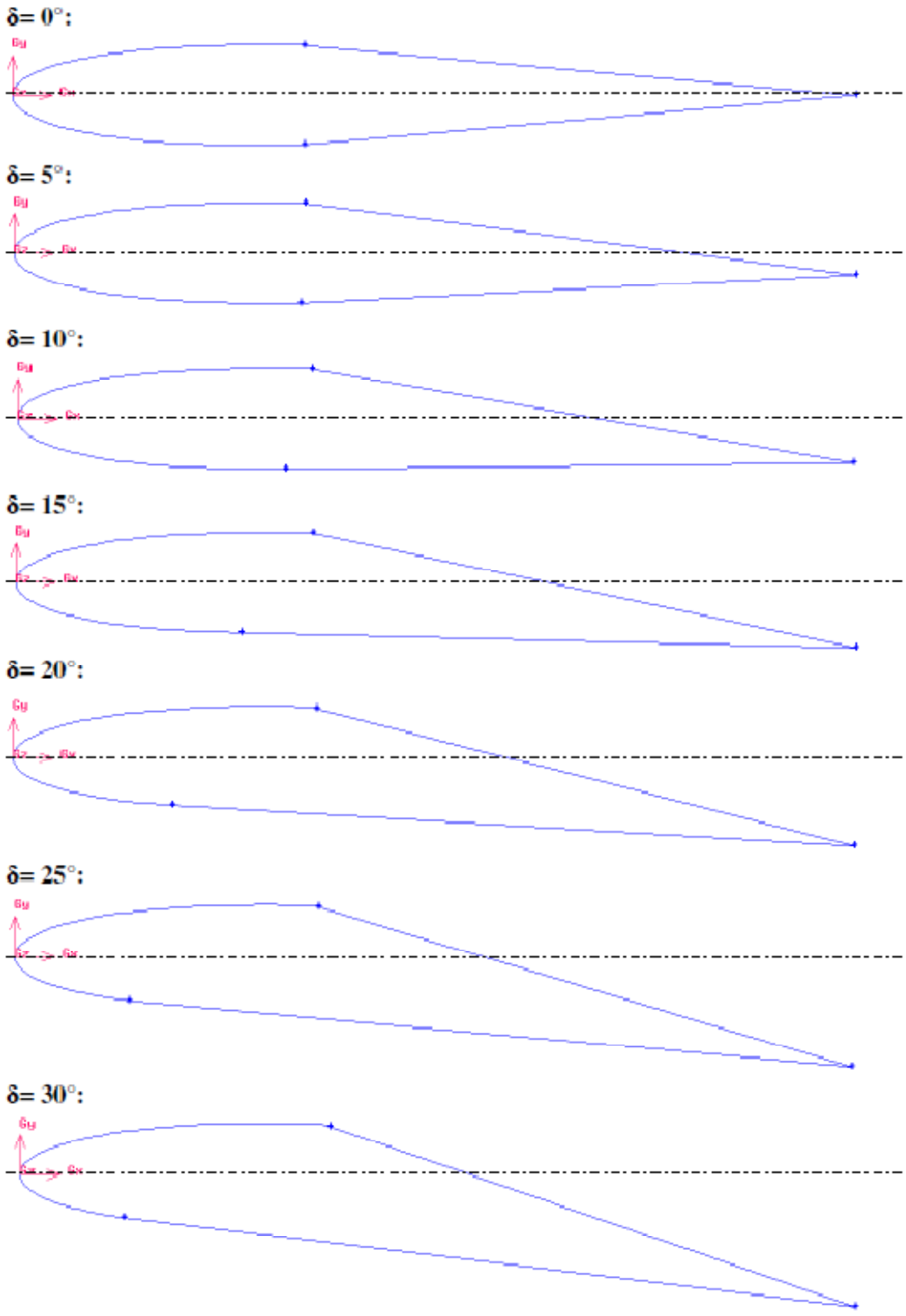

Figure 78: CFD Airfoil Geometry of Airfoil Shape Change due to Actuation

Figure 78 shows the geometry for the airfoil created in GAMBIT for different actuator tip rotation angles.

4.3.2.2 Mesh Generation

A farfield boundary around the airfoil needed to be generated for the mesh generation. A rule of thumb is to create the farfield boundaries in a distance of ten to twenty times the length of the airfoil in order to simulate the flow around the airfoil more precisely.[71] The author decided to use 3000 mm (20 times the length of the airfoil) in the horizontal direction (behind the airfoil) and 2000 mm (13.3 times the length of the airfoil) in vertical direction. The vertex at the tip of the trailing edge was used as the center point of the half circle of the farfield boundary in front of the airfoil.

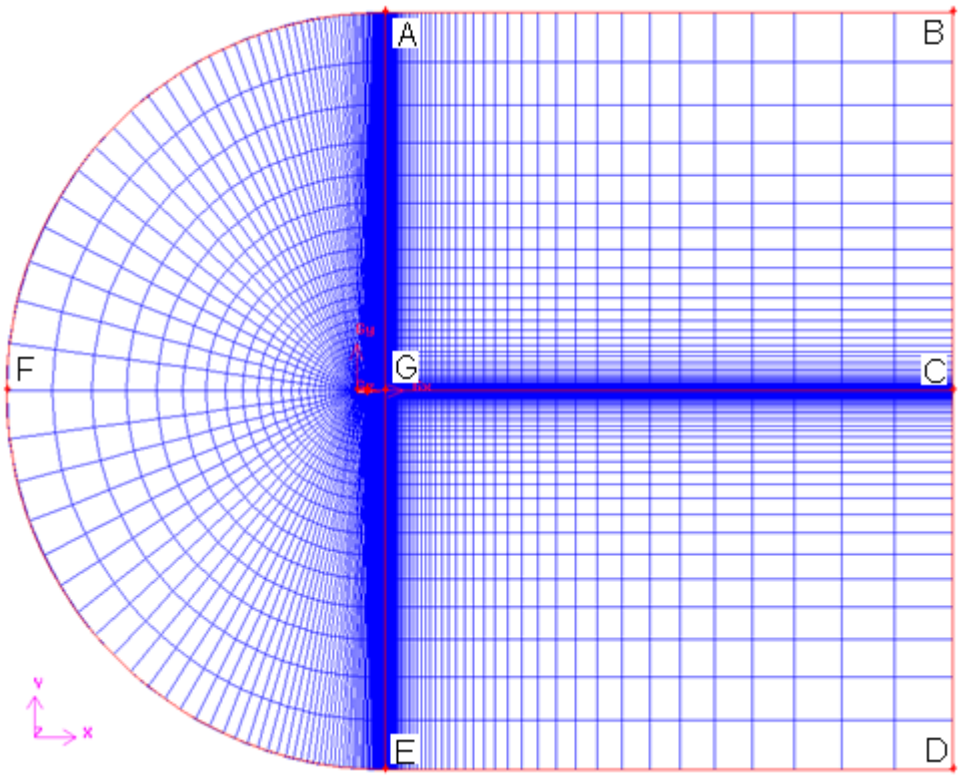

Figure 79: CFD Mesh Farfield

Table 3: Mesh Generation for Farfield Boundaries

Line	Direction		Interval Count
AB, GC, ED	Left to Right	First Length: 0.5	60
GA, CB	Upwards	Successive Ratio: 1.15	45
GE, CD	Downwards	Successive Ratio: 1.15	45
AF	From A to F	First Length: 0.5	75
EF	From E to F	First Length: 0.5	75

The change in interval count for the mesh generation on the surface line of the airfoil was caused by the changing geometry of the airfoil. Figure 80 and Figure 81 shows that the vertices I and J are the points were the skin separates from the leading edge substructure. Due to the actuation, these points were starting to move and the length of the lines with the mesh seed starting to vary greatly. According to the limitations of the control system described in Chapter 4.2.2 the maximum deflection of the actuator was $\delta=30^{o}$, caused by the limited current amplification factor of the amplifier circuit (Chapter 4.2.3).

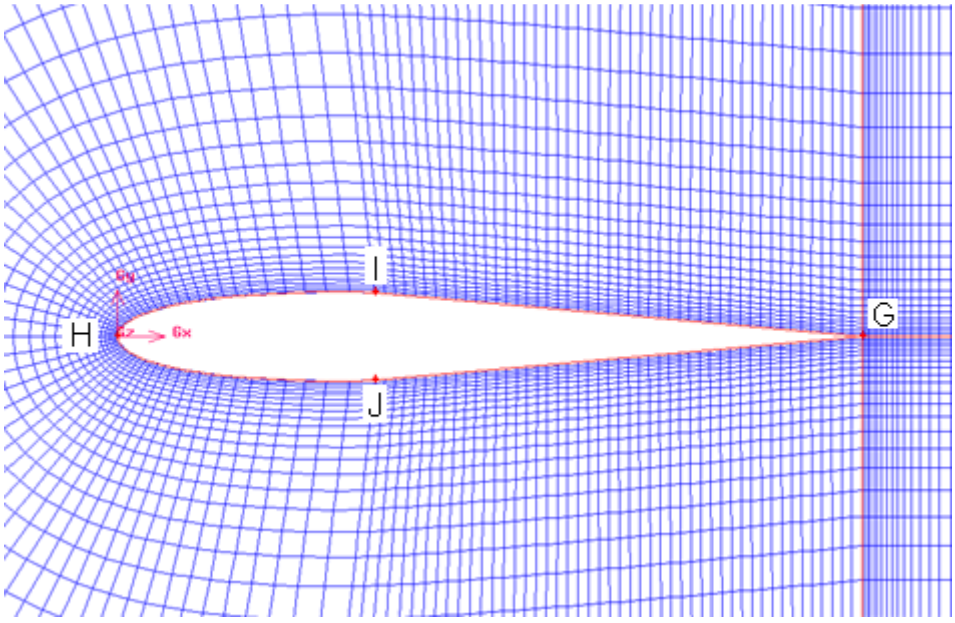

Figure 80: CFD Mesh for Airfoil with no Actuation

Table 4: Mesh Generation around Airfoil

			Interval Count						
Line	**Direction**		**δ = 0°**	**δ = 5°**	**δ = 10°**	**δ = 15°**	**δ = 20°**	**δ = 25°**	**δ = 30°**
GI	-	Successive Ratio: 1	35	35	35	30	30	30	30
GJ	-	Successive Ratio: 1	35	35	35	40	45	45	45
HI	H to I	First Length: 0.5	40	40	40	45	45	45	45
HJ	H to J	First Length: 0.5	40	40	40	35	35	35	35

Figure 81 shows the mesh around the airfoil for the fully actuated case of 30°. It can be seen that the vertex at the trailing edge is the middle point of the two farfield squares and the half circle.

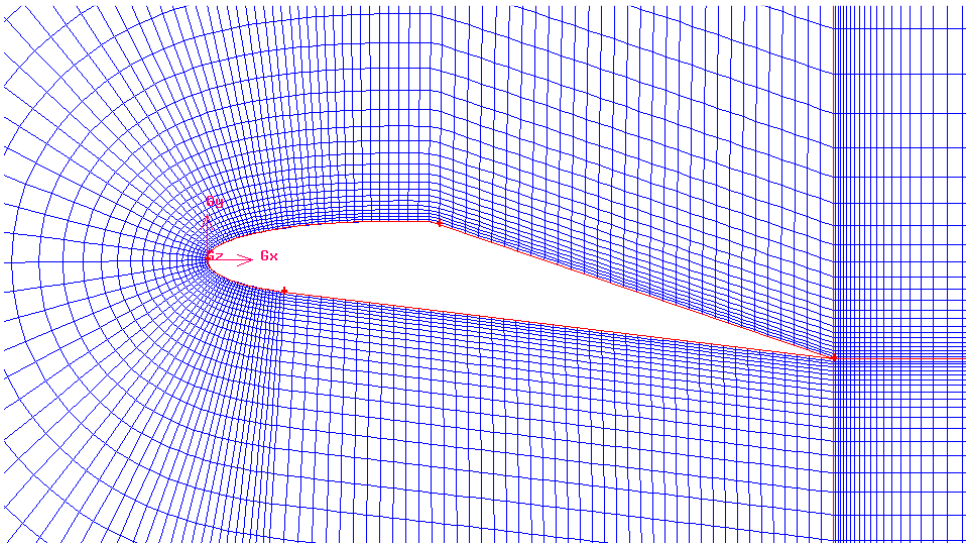

Figure 81: CFD Mesh for Airfoil with 30 deg Actuator Tip Displacement

The mesh described above had an overall number of 12150 cells with 24555 faces and 12405 nodes for each of the seven different sub cases (δ=0°, δ=5°, …, δ=30°).

4.3.3 Fluent Setup

The speed of sound under SSL (standard sea level) conditions is 340 meter/second which led to a free stream Mach number of 0.0735. The Mach number was low enough that the assumption of existence of incompressible flow was legitimate. An implicit segregated solver for inviscid, steady flow was selected for the analyses. The operating pressure was set to 101,325 Pa, the operating temperature was set to 293.15 Kelvin (20°C) and the density of air was set to 1.2041 kg/m^3 (see Chapter 4.3.1: Operating Condition Assumptions).

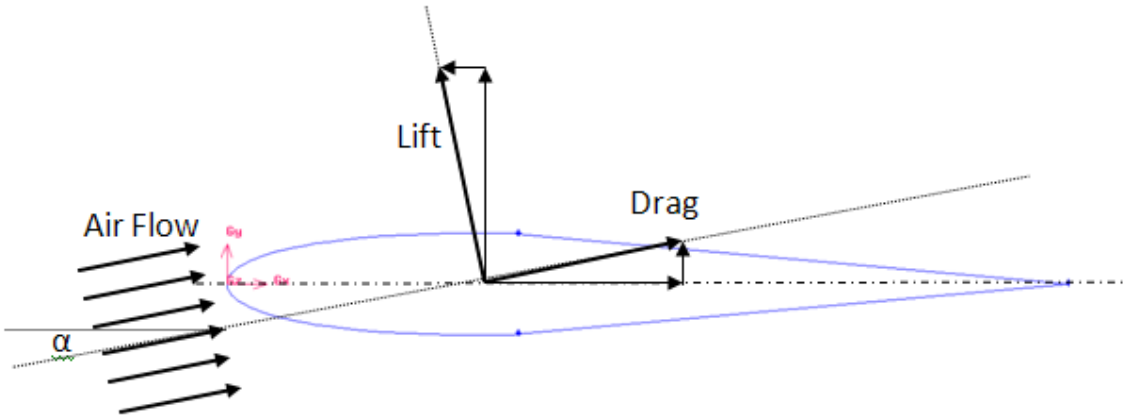

Figure 82: Airfoil with Angle of Attack in Air Flow

The assumption was made that the airflow arrives at the airfoil under the angle of attack in order to simplify the process of analyzing the airfoil at different angles of attack (Figure 82). Therefore the velocity needed to be divided into components (Table 5: Velocity Components). To obtain the correct drag and lift coefficient the factor components needed to be purported (Table 5: Factors).

Table 5: Velocity and Angular Components

	α=0°	α=2°	α=4°	α=6°	α=9°	α=10°
Velocity Component						
x	25.00 m/s	24.98 m/s	24.94 m/s	24.86 m/s	24.76 m/s	24.62 m/s
y	0.00 m/s	0.87 m/s	1.74 m/s	2.61 m/s	3.48 m/s	4.34 m/s
Factor Component						
x	1.0000	0.9994	0.9976	0.9945	0.9903	0.9848
y	0.0000	0.0349	0.0698	0.1045	0.1392	0.1736

The CFD model in Fluent was separated in four different regions, Farfield 1 (Figure 79: AF and EF), Farfield 2 (Figure 79: AB and DE), Farfield 3 (Figure 79: BC and CD) and the Airfoil (Figure 79: GI, IH, HJ and JG). Farfield 1 and Farfield 2 were set to Velocity-Inlet with the velocity components outlined in Table 5. Farfield 3 was set to Pressure-Outlet with a gauge pressure of 0 Pa. The Airfoil boundary was set to Wall to ensure no flow passes through the airfoil.

The solution parameters were set to simple pressure-velocity coupling with the PRESTO! – pressure discretization for the Second Order Upwind Scheme. The residuals for continuity, x-velocity and y-velocity were set to a 1e-06 convergence criterion. After initializing and iterating FLUENT obtained the results described in the following chapters.

4.3.4 Lift- and Drag Coefficients

The lift and drag coefficients were obtained for six different angles of attack, α=0°, α=2°, α=4°, α=6°, α=8° and α=10°.

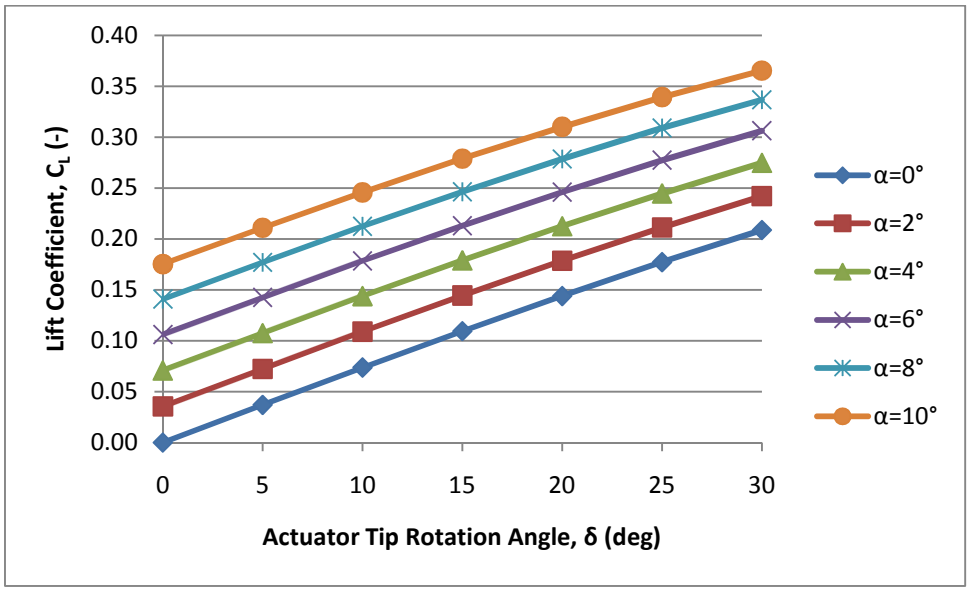

Figure 83: Lift Coefficient C_L over Actuator Tip Rotation Angle δ

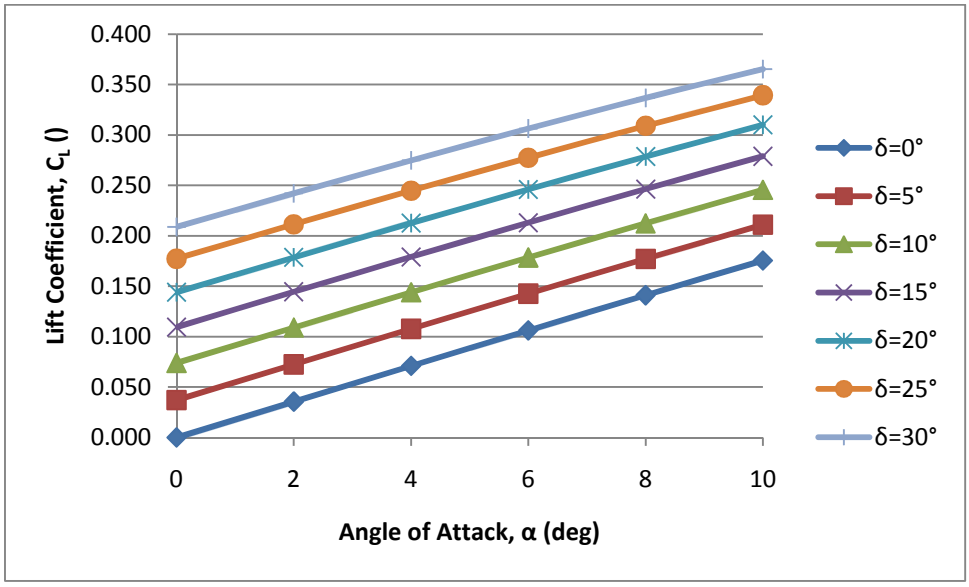

Figure 84: Lift Coefficient C_L over Angle of Attack α

Figure 83 clearly shows an improvement in lift coefficient due to actuation for no angle of attack, the lift coefficient increased from zero with no actuation to over 0.2 with 30° actuator tip rotation angle. These results could be increased even more by increasing the angle of attack. Figure 83 also shows the nearly linear slope of the curves in regards to the actuator tip rotation angle; this means that the lift coefficient can be easily controlled by the actuator itself. This meant that the lift coefficient is directly proportional to the actuator tip displacement angle.

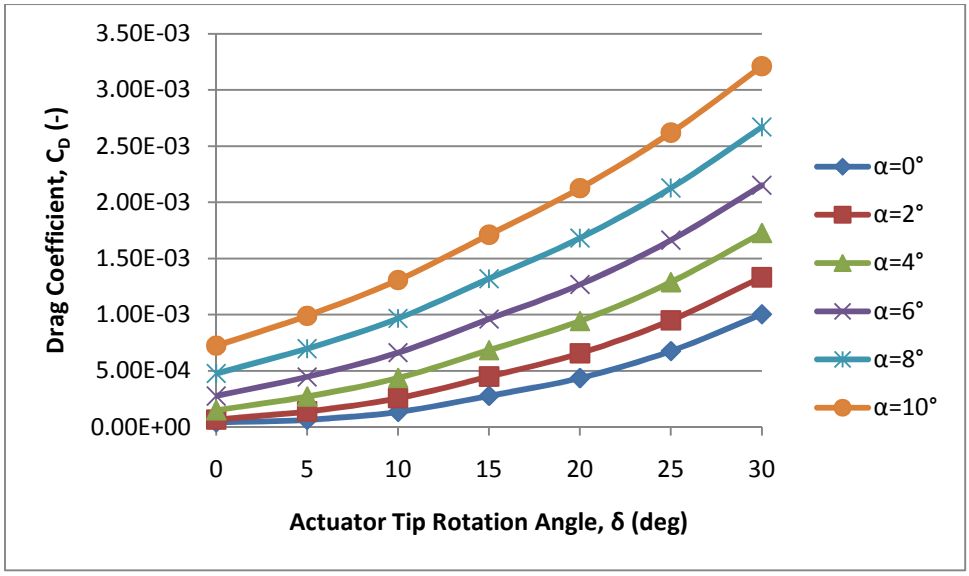

Figure 85: Drag Coefficient C_D over Actuator Tip Rotation Angle δ

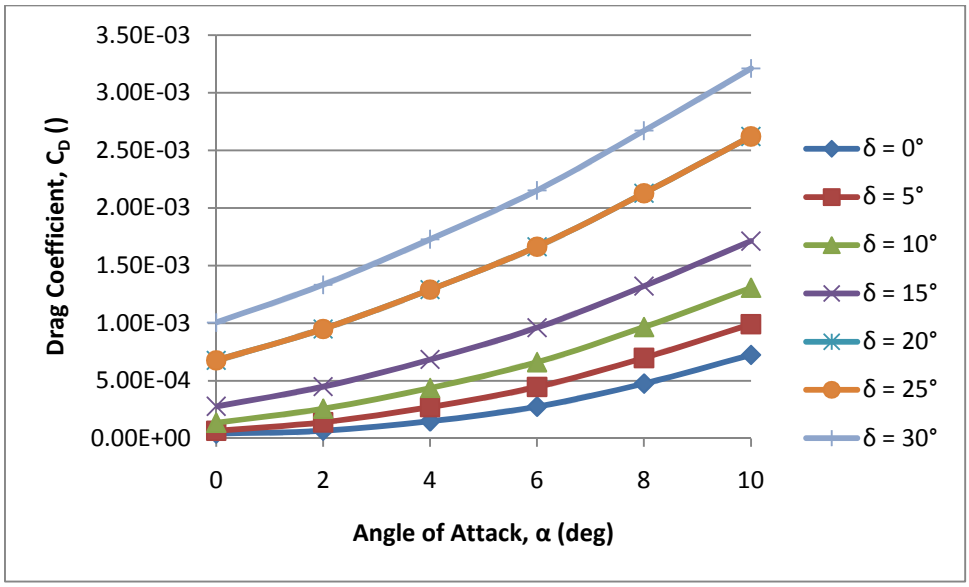

Figure 86: Drag Coefficient C_D over Angle of Attack α

Figure 85 shows the drag coefficient due to pressure force. The drag coefficient is a summation of the drag coefficient due to pressure force $C_{d\ pressure}$ and the pressure coefficient due to viscous force $C_{d\ skin\ friction}$. In this model the drag coefficient due to viscous force was set to zero because of the inviscid model. In reality $C_{d\ skin\ friction}$ has the biggest contribution to drag but will be ignored in this case because of the specification of an inviscid model.

4.3.4.1 Lift Forces on Airfoil

For the analyses of the maximum force on the flap it was important to obtain the lift on the airfoil. The FLUENT® analyses described above gave back a lift force for an airfoil width of one meter. But because the airfoil used in the experiments had two actuators and a length of 100 millimeters, the actual lift force was only 10% of the lift force obtained by FLUENT®.

Table 6: Lift Force over Actuator Tip Rotation Angle

	δ=0°	**δ=5°**	**δ=10°**	**δ=20°**	**δ=30°**	**δ=40°**	**δ=50°**
α=0°	0.00 N	1.39 N	2.77 N	4.12 N	5.42 N	6.67 N	7.86 N
α=2°	1.34 N	2.72 N	4.10 N	5.43 N	6.72 N	7.95 N	9.11 N
α=4°	2.67 N	4.05 N	5.42 N	6.73 N	8.00 N	9.21 N	10.34 N
α=6°	3.99 N	5.36 N	6.71 N	8.01 N	9.26 N	10.44 N	11.53 N
α=8°	5.30 N	6.66 N	7.99 N	9.27 N	10.48 N	11.63 N	12.67 N
α=10°	6.60 N	7.93 N	9.24 N	10.49 N	11.67 N	12.77 N	13.74 N

Because the lift force was the lift coefficient multiplied by the constant values of air density, air speed and area of airfoil, the lift force had a similar linear slope then the lift coefficient from Figure 83 and Figure 84. Table 6 shows zero lift for a non actuated airfoil, this made sense because a symmetric airfoil (NACA 0012) was used. The maximum lift that was produced by the 150 mm long and 100 mm wide airfoil was 13.75 Newton.

4.3.5 Pressure Distribution on Airfoil

The forces obtained by FLUENT in Chapter 4.3.4.1 were the forces acting on the entire wing, it was therefore necessary to obtain the fraction of the force applied only on the flap part of the wing. The drag forces were so small that they were neglected in the following calculations. The leading edge part had a length of 60 mm (40% of airfoil length) and the flap

part had a length of 90 mm (60% of airfoil length). The use of the pressure distribution over the airfoil obtained by CFD obtained a more accurate solution than taking the fraction of the length of the airfoil.[51]

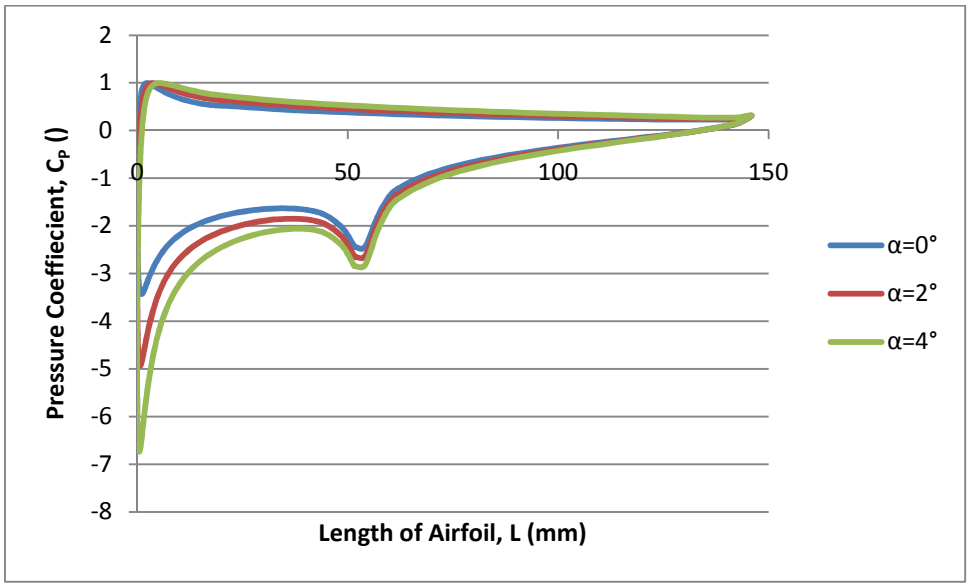

Figure 87: Pressure Coefficient Distribution over Airfoil at δ=30° for α=0°, α=2° & α=4°

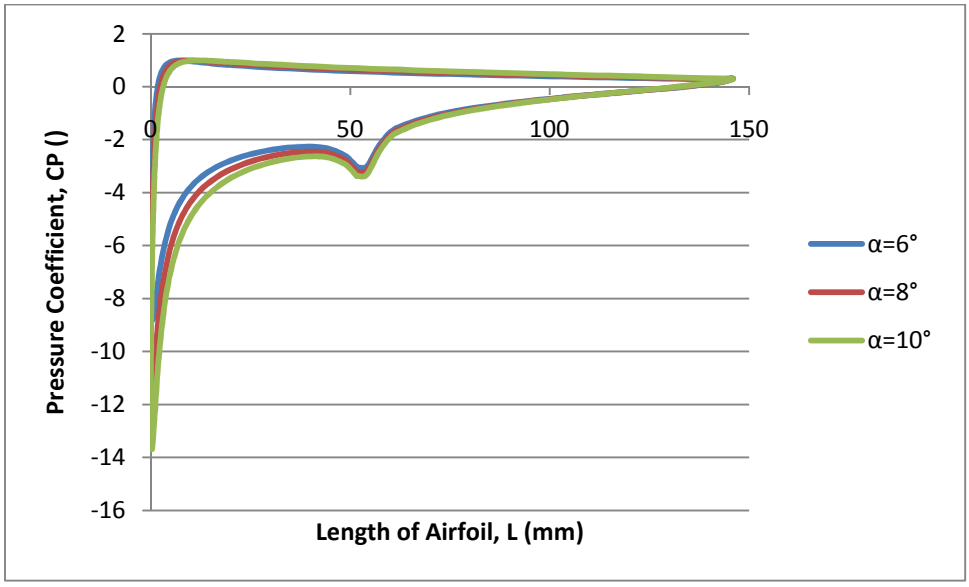

Figure 88: Pressure Coefficient Distribution over Airfoil at δ=30° for α=6°, α=8° & α=10°

The only reason why the six different pressure distributions were separated into two different charts was to make the change between the different angles of attack more obvious, otherwise the transitions became blurry. Figure 87 shows the pressure coefficient distribution over the

entire airfoil for three different angles of attack (α=0°, α=2° and α=4°) for an actuator tip rotation angle of δ=30°. Figure 88 shows the pressure distribution for the angles of attack of α=6°, α=8° and α=10° for an actuator tip rotation angle of δ=30°. The pressure coefficients of the other sub cases (δ=0°, δ=5°, δ=10°, δ=15°, δ=20° and δ=25° for α=0°, α=2°, α=4° α=6°, α=8° and α=10°) can be found in Appendix B. The pressure coefficients distribution is negative over the top of the airfoil and positive over the bottom of the airfoil. As expected, the pressure peaks occurred at the leading edge. The dent in the pressure distribution over the top of the airfoil (approximately at a distance of ~60 mm) was caused by the slope change of the skin while leaving the contour of the leading edge and becoming a straight line to the trailing edge (see Figure 78).

By integrating the area under the pressure coefficient curve (Figure 87 and Figure 88) the fraction of the pressure coefficient distribution over the flap section in relation to the pressure coefficient distribution over the whole airfoil was calculated. Table 7 shows the pressure distribution ratio for the flap area. With a length of the leading edge of 60 mm and an actuator/flap length of 90 mm, the following percentiles were obtained.

Table 7: Pressure Distribution Ratio on Flap Area for various Angles of Attack α and Actuator Tip Rotation Angles δ

	δ=0°	**δ=5°**	**δ=10°**	**δ=20°**	**δ=30°**	**δ=40°**	**δ=50°**
α=0°	25.38%	15.59%	16.45%	14.69%	14.20%	13.20%	13.38%
α=2°	23.41%	14.65%	14.89%	13.11%	12.79%	11.97%	12.19%
α=4°	21.69%	13.65%	13.38%	11.90%	11.90%	10.86%	11.18%
α=6°	19.93%	12.49%	12.24%	10.91%	10.71%	9.94%	10.28%
α=8°	18.60%	11.53%	11.26%	10.06%	9.84%	9.17%	9.46%
α=10°	17.42%	10.69%	10.49%	9.28%	9.08%	8.45%	8.72%

By multiplying the lift force obtained above (Table 6) with the pressure distribution ratio from Table 7 the lift force on the entire flap area was obtained. Figure 89 shows a plot of the force on the flap region for various angles of attack and actuator tip rotation angles. The author wants to emphasize again that all the forces in this chapter are for an airfoil with 100mm span.

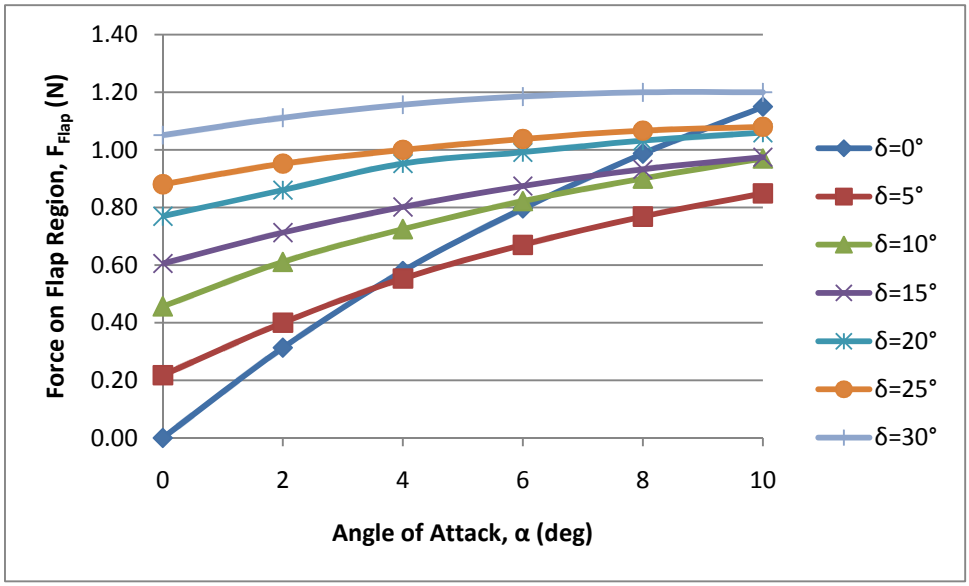

Figure 89: Force on Flap Region over Angle of Attack

Figure 89 shows that the force on the flap area converged to a maximum of F_{Flap}=1.2 N. It was interesting that almost all the curves have similar slopes, except for the airfoil geometry with no actuation (δ=0°). It was obvious that the curve for the airfoil with no actuation must have no lift force at an angle of attack of α=0°, because of its symmetric outline. Nevertheless this curve has a consistent slope throughout varies angles of attack which leads to a maximum force of F_{Flap}=1.15 N at an angle of attack of α=0°. By looking at the pressure distribution for δ=0° case from Figure 97 and Figure 98 in Appendix B it becomes obvious that the ratio of pressure distribution between flap area and leading edge area was higher than for any other case, therefore the percentage of the force acting on the flap increased. By multiplying these percentages of the pressure distribution ratio with the lift force from Table 6 (for δ=0° case: 0N<L<6.6N) the slope in Figure 89 was obtained.

The forces obtained in this chapter are the forces acting on the whole length of the actuator (whole flap area). This means that a part of this force will be dissipated by the leading edge and the other part needed to be exceeded by the actuation tip force of the actuator. With a conservative approach for the force separation, 30% of the flap force was carried by the leading edge and 70% needed to be overcome by the actuator. This assumption led to a

maximum force at the trailing edge $F_{TrailingEdge}$=0.805 N. Recalling that the proposed and built airfoil had two actuators built in, it could be said that the force at the trailing edge of $F_{TrailingEdge}$ would be partitioned to the two actuators, which led to a maximum force of 0.4025 N that each of the actuators needed to overcome.

4.4 Wind Tunnel Tests

On the 30th of April wind tunnel tests were undertaken in the small subsonic wind tunnel at The University of Kansas. The purpose of the wind tunnel test was to prove the performance of the airfoil in a real life application. The wind tunnel tests should prove if the SMAPBP actuator could be able to displace the trailing edge and increase the lift due to actuation. The performance of the airfoil was evaluated for different angles of attack and different actuator tip angle rotations.

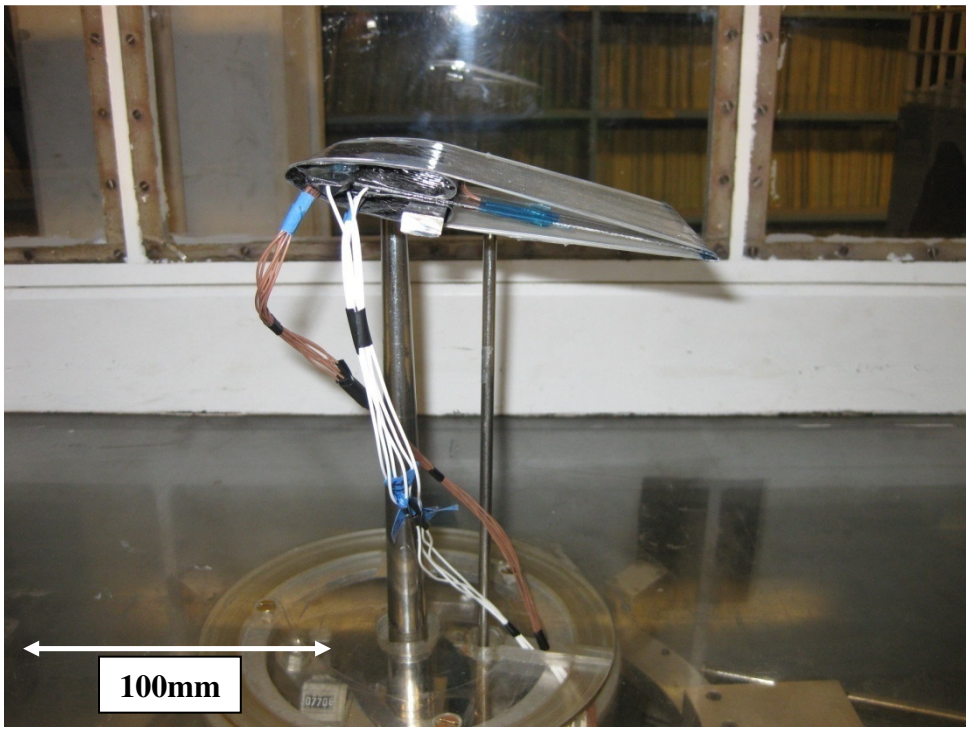

Figure 90: Side View of Airfoil in Wind Tunnel

A thick steel bar served as a spar of the airfoil. The steel bar gave the leading edge enough stiffness to mount the airfoil on the side of the actual wind tunnel mount. Measurements were taken for actuator tip rotation angles of $\delta=0°$, $\delta=10°$, $\delta=20°$ and $\delta=30°$ with angles of attack of $\alpha=0°$, $\alpha=2°$, $\alpha=6°$ and $\alpha=10°$. For each angle of attack the measurements of the four tip rotation were undertaken. After each angle-of-attack measurement, the wind tunnel was turned off and a new angle of attack was adjusted.

4.4.1 Behavior of Airfoil in Wind Tunnel

The SMAPBP actuator performed quite well during the wind tunnel tests, the trailing edge was displaced up to δ=30°. The behavior of the airfoil in the wind tunnel seemed a little bit different than without any applied air flow. The first big difference was that the power consumption of the actuators was significantly higher than without any airflow. Without any airflow an actuator tip rotation angle of δ=30° could be achieved with 0.6 A actuation current, during the wind tunnel tests a actuation current of up to 1.0 A needed to be applied to achieve similar displacements. This effect was probably caused by convectional cooling of the SMA actuator wires by the surrounding airflow. Due to the fact that the airfoil didn't have side panels air flow could enter into the airfoil and cool down the SMA wires (see Figure 91).

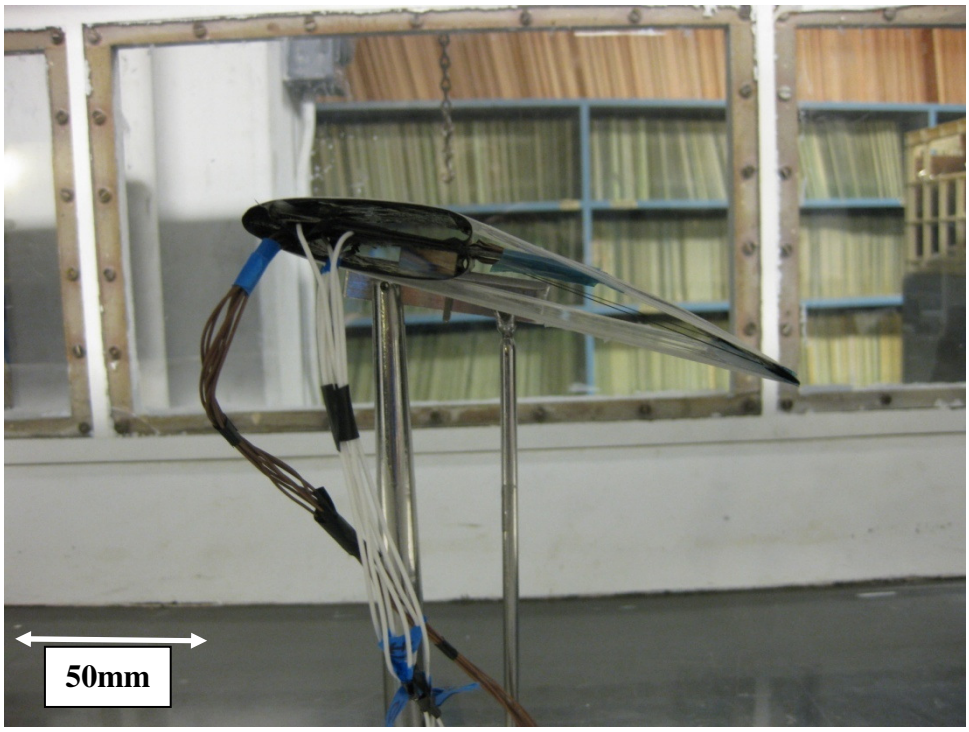

Figure 91: Side view of Airfoil in Wind Tunnel with a Tip Rotation of δ=30°

During the wind tunnel tests it was observed that the skin membrane between the end of the leading edge and the trailing edge vibrates with a very low amplitude but high frequency. The impact of this high frequency vibration on the performance of the airfoil was assumed to be rather insignificant, therefore it was neglected.

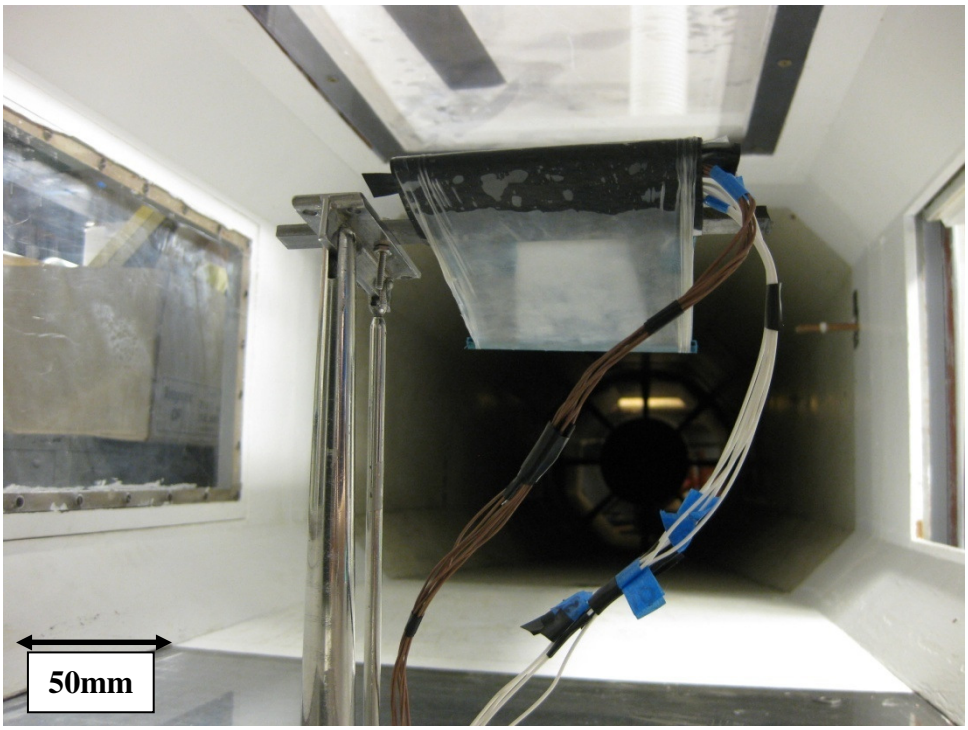

Figure 92: Front view of Actuated Airfoil with δ=30°

The measurements for lift and drag were recorded twice for each measurement.

4.4.2 Lift and Drag Coefficients

The lift and drag coefficients were calculated from the lift and drag forces obtained by the wind tunnel experiments.

$$C_L = \frac{L}{\frac{1}{2}\rho v^2 A} \qquad 4.4\text{-}1$$

With the lift force (L) obtained by the wind tunnel tests, ρ is the density of air (assumed to be 1.2041 kg/m^2) and v is the velocity of the airflow. In this case the velocity was set to 25 m/s due to the assumptions made for the CFD analyses in Chapter 4.3.1. The airfoil had a chord length of 150 mm (0.15 m) and a width of 100 mm (0.1 m) which led to an area A of 0.015m^2.

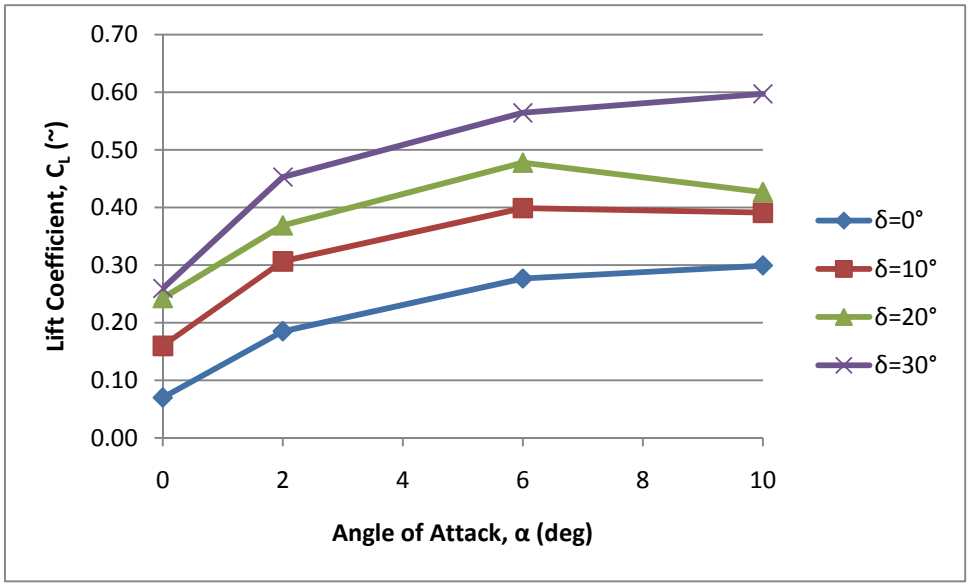

Figure 93: Lift Coefficient over Angle of Attack from Wind Tunnel Experiments

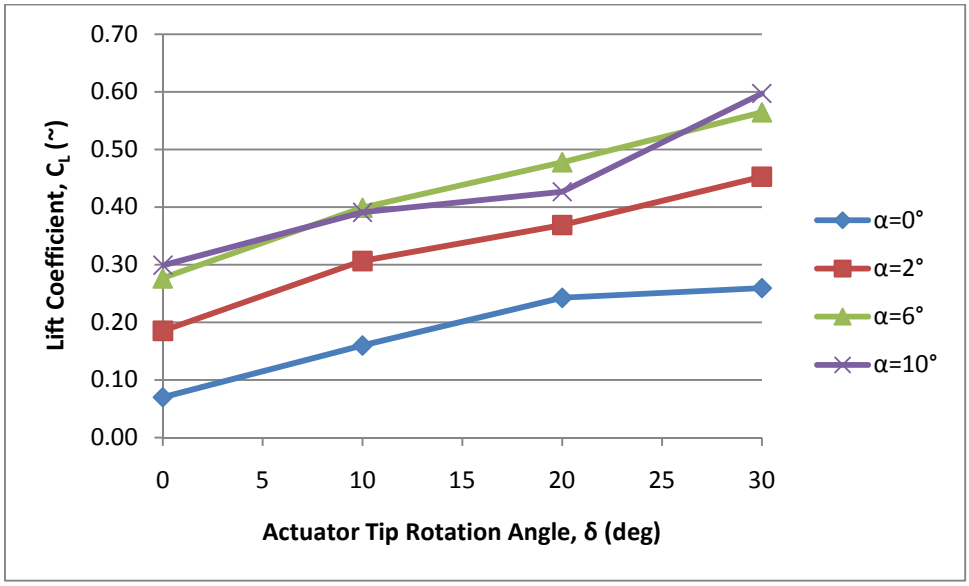

Figure 94: Lift Coefficient over Actuator Tip Rotation Angle from Wind Tunnel Experiments

Figure 93 and Figure 94 show the lift coefficient over various angles of attack and actuator tip displacement angles. The two figures show that the lift increased with an increasing angle of attack α and increasing actuator tip rotation angle δ. It can be seen that the slope in Figure 94 is almost linear. The values for the lift coefficient for an angle of attack of α=6° and α=10° had similar values. For an actuator tip rotation angle of δ=20°, the lift coefficient of the α=10° case was even smaller than the α=6°. These observations made no sense and it may be caused by a recording error of some kind. By looking at Figure 93 it seems that the curves have a

slightly curved slope that would suggest that the airfoil is being subjected to stall. By looking at the CFD results for the lift coefficient from Chapter 4.3.4 it is obvious that the airfoil should not be subjected to stall with these flight conditions.

The drag coefficient is calculated in a similar manner than the lift coefficient:

$$C_D = \frac{D}{\frac{1}{2}\rho v^2 A} \qquad 4.4\text{-}2$$

Where D is the drag force obtained by the wind tunnel tests.

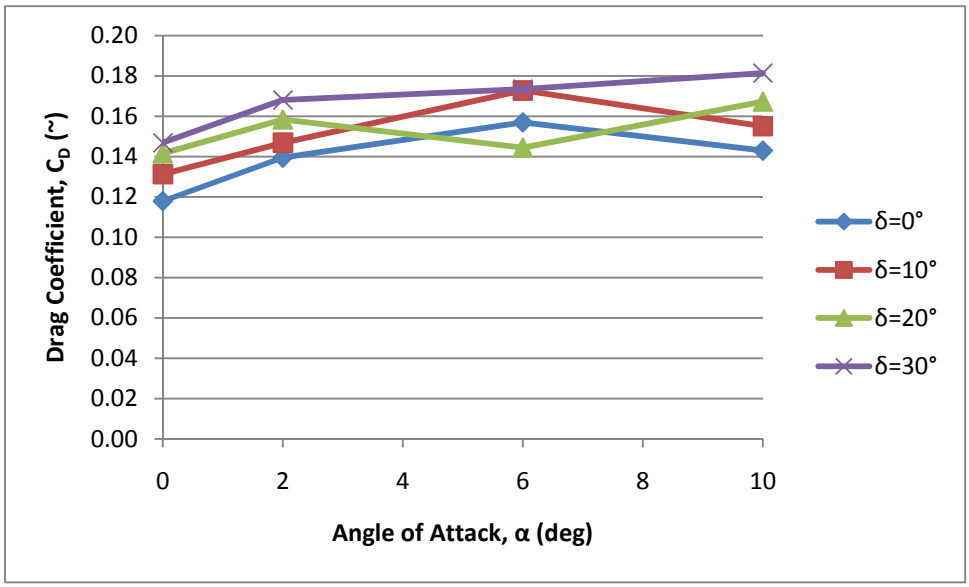

Figure 95: Drag Coefficient over Angle of Attack from Wind Tunnel Experiments

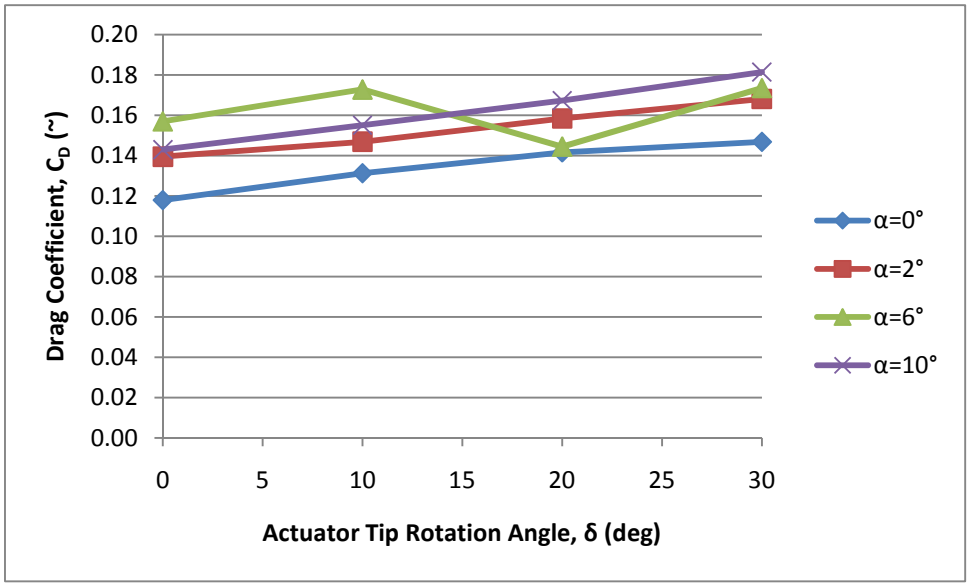

Figure 96: Drag Coefficient over Actuator Tip Rotation Angle from Wind Tunnel Experiments

Figure 95 and Figure 96 show the drag coefficient for various angles of attack and actuator tip rotation angles. The trend of the two figures for the drag coefficient were similar to those of the lift coefficient, the curves in Figure 95 show a slightly curved trend and the curves in Figure 96 are almost linear. By looking at Figure 95 and Figure 96 for the case with an angle of attack of α=6° it seems that the measurements are afflicted with some kind of error. The drag coefficient measured in the wind tunnel experiments were one to two magnitudes higher than the drag coefficients obtained by the CFD analyses, this could have two profound reasons. The first reason was that the CFD analyses only obtained the drag coefficient due to pressure force. The CFD analyses ignored the effect of drag due to viscous force (skin friction) which has the biggest contribution to the drag coefficient. The second reason why the measured drag coefficient was so much higher may be the additional drag that's induced from the test fixture, the wires and the flow around the sides of the airfoil.

Nevertheless, the wind tunnel tests proved that the airfoil was working under operating conditions. The experiments showed that the lift can be increased by actuating the SMAPBP actuator. The wind tunnel experiments also showed that the SMAPBP actuator can overcome the aerodynamic loads and displace the trailing edge.

5 Conclusions, Recommendations and Future Work

5.1 Conclusions

5.1.1 SMAPBP Actuator

The experiments showed that the developed SMAPBP actuator was capable of achieving high tip displacements and rotations. It can be concluded that Post-Buckled Precompressed (PBP) amplification techniques work quite well with antagonistically arranged SMA bender beams. A 135 mm long steel-fiberglass-epoxy composite actuator was actuated by a pair of 0.254 mm diameter Dynalloy Flexinol wires. The specimen demonstrated deflection levels in excess of 120° peak-to-peak, representing a deflection growth of 33.5% at axial loads of 5 N. Experiments showed that the actuator can be actuated in both direction with similar results and magnitude on the tip angle rotation and tip force values. Trapezoidal buckling beam theory with consideration of local stiffness's coming from laminated plate theory locally showed a good first approximation for the theoretical results. Nevertheless, the slope of the theoretical and experimental results differed by an order of two in magnitude. This may be caused by the highly hysteretic behavior of the SMA material with and its amplification due to the applied PBP mechanism. The SMA actuator wires were prestrained to approximately 2.5% and demonstrated increasingly hysteretic behavior as axial loads were increased. Because of the highly hysteretic behavior, it was clear that SMAPBP actuators should only be used as precision controllers in conjunction with position feedback loops. Although the antagonistic prestrain levels were indeed quite low, this lent to good high cycle performance as the actuator showed no signs of actuation fatigue over several thousand actuation cycles. The work introduced by the SMAPBP actuators succeeded the required pulling force to overcome the air loads at the trailing edge of the wing. The measurements of the maximum tip force were only taken for the blocked force case where the wire was aligned at the surface of the actuator. Considering the fact that for higher tip rotation angles the SMA wire would be further away from the neutral axis of the actuator, it can be stated that the vertical tip force

part will increase significantly. The force introduced by the SMA wire due to actuation will add an additional bending load to the buckling load from actuation. At this stage the actuator is optimized for a buckling force of around 3.5 N – 4.5 N and an actuated/buckling length of 90 mm. The work that was done in this thesis can serve as a basic design study for future SMAPBP actuators for other load cases and applications.

5.1.2 Airfoil

With the employment of the SMAPBP actuator in the airfoil, the concept of an adaptive flap system with SMA actuation and applied PBP mechanism, was proven too. The decision was made to use the NACA0012 profile with a chord length of 150 mm as a baseline for the development for the adaptive airfoil. The experiments showed that the SMAPBP actuator integrated into the airfoil worked quite well with the applied buckling force from an elastic latex skin. The experiments showed that the SMAPBP actuator can achieve high trailing edge displacements. The airfoil was proposed of being employed in a Micro Unmanned Aerial Vehicle (MUAV), the decision was made to use the popular RQ-11 developed by AeroVironment because of its similar airfoil dimensions. Based on the data sheet provided by AeroVironment the maximum cruising speed of the MUAV was set to 25 m/s for the CFD-analyses. The CFD analyses obtained the lift coefficients for the non actuated and actuated airfoil for different angles of attack ($0° < \alpha < 10°$). An increase in lift coefficient of $C_L=0$ at the non actuated state ($\alpha=0°$) to $C_L=0.209$ for a tip rotation angle of $\delta=30°$ was obtained. For an angle of attack of $\alpha=10°$ an improvement from $C_L=0.175$ ($\delta=0°$) to $C_L=0.365$ ($\delta=30°$) could be obtained. By using the pressure coefficient distribution, the maximum force on the flap region was calculated. The values from the CFD analyses were then compared to the results of the experimental tip force tests to ensure that the flap system was capable of achieving the necessary force to overcome the aerodynamic loads. Wind tunnel experiments showed that the airfoil was working quite well under real live conditions and that the SMAPBP actuator was able to overcome the aerodynamic loads introduced by the air flow. An increase in lift

coefficient from C_L=0.07 for the non actuated case with no angle of attack to CL=0.299 for an angle of attack of α=10° (δ=0°) could be obtained. For the α=10° case, the lift coefficient was increased from C_L=0.299 with no actuation to C_L=0.597 for an actuator tip rotation angle of δ=30°. The lift coefficients obtained from the CFD analyses were similar to the lift coefficients from the wind tunnel experiments for small actuator tip rotation angles. By increasing the actuator tip rotation angle the discrepancy between the CFD result and the wind tunnel result was increasing too. For an angle of attack of α=10° and a tip rotation angle of δ=30° the difference between the CFD analyses and the wind tunnel tests in lift coefficient was ΔC_L=0.232. This could have multiple reasons; it may be caused by the modeling of the shape of the airfoil in GAMBIT (e.g. modeling of crossover of the elastic latex from leading edge to trailing edge). Another explanation could be that the airflow in the wind tunnel test went into the airfoil thru the sides and developed additional lift to the inside area of the latex skin (last 90 mm of airfoil). By comparing the maximum drag coefficient of the CFD analyses (C_D=0.00321) to the maximum drag coefficient of the wind tunnel tests (C_D=0.181) the immense impact of the introduced drag due to viscous force (skin friction) became obvious. An inviscid model was selected because of the very low Mach number (Ma=0.0735) due to the air flow velocity assumption of 25m/s. The inviscid model accounts only for the drag induced by pressure force and not by viscous force which has the biggest contribution to drag. The other reason for the large difference between the drag coefficients may be the drag introduced by the test fixture and the measuring cables in the wind tunnel.

The developed control system in this thesis was quite simple but it showed good controllability of the entire airfoil and it proved the concept that the non-linear hysteretic behavior could be overcome with a simple active position feedback system. In this case the active position feedback system was implemented with strain gages applied to the airfoil that measured the strain that is proportional to the actuator tip rotation angle. With a simple

control loop in Labview®, the actuation current could be changed over an amplifier with a maximum output current of 0.6 A, which led to a maximum trailing edge rotation of approximately $\delta=30°$. A precision of 2° was obtained by the control algorithm caused by oscillation of the input signal with a respond time from around one to two seconds in case the output voltage was between 2.5 V and 4.5 V. For the case that the voltage was lower then 2.5 V, the reaction took up to 5 seconds to achieve the desired tip displacement. Nevertheless, the control system showed good controllability of the airfoil by using Labview® as a programming software.

5.2 Recommendations and Future Work

The theoretical approach showed some discrepancies with respect to the experimental results. A more exact analytical model needs to be obtained for this kind of SMA actuated actuator. The analytical theory used in this thesis was originally developed for piezoelectric non-tapered actuators. There are several differences that needed to be considered between the piezoelectric actuator and the SMAPBP actuator from this thesis. The first big difference was the tapered shape of the SMAPBP specimen. In this thesis a shape function for a trapezoidal shape was used to modify the known PBP equation. Other differences that were not considered are impacting the result too, for example that the piezoelectric approach had the piezoelectric material as a sheet over the whole substructure of the actuator and the SMA wire instead was only a wire with a given diameter in the running along the symmetry line of the actuator. Another factor could be that the SMA wire was not integrated in the laminate because of the burn-through issue described in Chapter 3.1.2.4. Future work should be focused on the development of a new kind of theory that considers all these factors that are different in the SMAPBP actuator compared to its piezoelectric model. As mentioned above, the SMAPBP actuator developed in this work was optimized for a buckling load of 3.5 N – 4.5 N and an actuated/buckling length of 90 mm. For other applications new actuators need to be considered which are designed specifically for the desired load case. Nevertheless, this

work and its developed design and manufacturing techniques could serve as a good basis for future SMAPBP actuator developments.

The second part of the thesis was focused on the development of the adaptive airfoil. The research done in this work was using the symmetric NACA0012 airfoil, because the focus of this thesis was more on the performance of the SMAPBP actuator integrated into the airfoil than to optimize the airfoils aerodynamic performance. Future work should be focused on the improvement of the shape of the airfoil. FLUENT showed that the pressure distribution had a significant dent at the crossing from the leading edge contour to the straight surface from leading edge to trailing edge. A more optimized end of the leading edge would enhance the overall performance of the entire airfoil. The research done in this thesis can be seen as a starting point for more improved airfoil shape. A better aerodynamic performance and higher lift coefficients will bring the change from the basic symmetric NACA 0012 shape to a more aerodynamic non-symmetric NACA profile.

The results obtained by the CFD analyses and the wind tunnel tests were similar to each other for the lift coefficients but differed greatly for the drag coefficients. The accuracy of the CFD model can be increased significantly by developing a three dimensional CFD model that accounts for drag introduced by viscous force. The accuracy of the wind tunnel tests in contrast can be increased by attaching side panels to the airfoil. The side panels prevent the airflow from entering the airfoil through the sides and decreases the impact of the test fixture on the measurements.

Future research should also being focused on the improvement of the control system. The control system developed in this master thesis served the only purpose to show the possibility of overcoming the nonlinear, hysteretic behavior of the SMAPBP with an applied active position feedback system. For an actual application in a UAV the mass of the control system with amplifier state needs to be decreased by one or two magnitudes, a switch to an other

more powerful control/amplifier system would be recommended. The linear control algorithm was overshooting by an average of 2°, for precision trailing edge displacement it would be necessary to change the kind of algorithm. A change of the software to a more control friendly software would also be recommended. Labview with its limited programming tools was good enough to prove the basic idea of the concept and its do ability.

Acknowledgements

The author wants to thank his advisor, Dr. Ron Barrett for his excellent supervision of this thesis. Dr. Ron Barrett helped me to learn how to think outside the box, to try new approaches, which is from significant importance for working in the field of adaptive materials and structures. I want to thank him for introducing me to the field of adaptive materials, a very interesting field with unique possibilities and opportunities. I also would like to thank Dr. Mark Ewing and Dr. Ray Taghavi for their support and time for serving as my Master's committee members.

A special thanks goes to our lab director Wes Ellison, whose knowledge and great helpfulness was a significant contribution to the success of this project. I also want to thank John Hunter from the composite laboratory for his help and advice regarding composite layup and manufacturing.

I also want to thank my laboratory colleges Mike Brennison and Richard Bramlette for their support and help during my research in the Adaptive Structures Lab of The University of Kansas. I would also like to thank Wonjin Jin for his help and guidance in the area of CFD modeling.

Last but not least I want to thank my family back home in Germany for their great support in my studies.

6 References

1. Anon., Dictionary, O. "Oxford English Dictionary," *Notes and Queries*.

2. Klickstein, H. "Pierre Curie: An appreciation of his scientific achievements," *Journal of Chemical Education* Vol. 24, No. 6, 1947, p. 278.

3. Voigt, W. *Lehrbuch der kristallphysik*: BG Teubner, 1910.

4. Buehler, W., and Wiley, R. "The properties of TiNi and associated phases," *Report, NOLTR*, 1961, pp. 61-75.

5. Roskam, J. *Airplane design*: DARcorporation, 1985.

6. Crawley, E. "Intelligent structures for aerospace: a technology overview and assessment," *AIAA Journal* Vol. 32, No. 8, 1994, pp. 1689-1699.

7. Nishiyama, Z., Fine, M., Meshii, M., and Wayman, C. *Martensitic transformation*: Academic Press, 1978.

8. Waram, T. *Actuator design using shape memory alloys*: TC Waram, 1993.

9. Patoor, E., Lagoudas, D., Entchev, P., Brinson, L., and Gao, X. "Shape memory alloys, Part I: General properties and modeling of single crystals," *Mechanics of materials* Vol. 38, No. 5-6, 2006, pp. 391-429.

10. Huang, W., and Goh, H. "On the long-term stability of two-way shape memory alloy trained by reheat treatment," *Journal of Materials Science Letters* Vol. 20, No. 19, 2001, pp. 1795-1797.

11. Huang, W., and Toh, W. "Training two-way shape memory alloy by reheat treatment," *Journal of Materials Science Letters* Vol. 19, No. 17, 2000, pp. 1549-1550.

12. Crawley, E., and De Luis, J. "Use of piezoelectric actuators as elements of intelligent structures," *AIAA Journal* Vol. 25, No. 10, 1987, pp. 1373-1385.

13. Lesieutre, G. A., and Davis, C. L. "Can a Coupling Coefficient of a Piezoelectric Actuator be Higher than its Active Material?," *Journal of Intelligent Material Systems and Structures* Vol. 8, 1997, pp. 859 - 867.

14. Lesieutre, G. A., and Davis, C. L. "Transfer Having a Coupling Coefficient Higher than its Active Material," *US Pat. 6,236,143 issued 22 May*, 2001.

15. Barrett, R., and Tisco, P. "PBP Adaptive Actuator Device and Embodiments," *International Patent Application Number PCT/NL2005/000054, via TU Delft, 18 February*, 2005.

16. Barrett, R., Vos, R., Tisco, P., and De Breuker, R. "Post-Buckled Precompressed (PBP) Actuators: Enhancing VTOL Autonomous High Speed MAVs," *13th AIAA/ASME/AHS Adaptive Structures Conference 18 - 21 Apr 2005 - Austin, Texas*, 2005.

17. Vos, R., De Breuker, R., Barrett, R., and Tisco, P. "Morphing Wing Flight Control Via Post-Buckled Precompressed Piezoelectric Actuators," *AIAA Journal of Aircraft* Vol. 44, No. 4, 2007, pp. 1060 - 1068.

18. Barrett, R., McMurtry, R., Vos, R., Tisco, P., and De Breuker, R. "Post-Buckled Precompressed Pieyoelectric Flight Control Actuator Design, Development and Demonstration," *Journal of Smart Materials and Structures* Vol. 15, No. 5, 2006, pp. 1323 - 1331.

19. De Breuker, R., Vos, R., Barrett, R., and Tisco, P. "Nonlinear Semi-Analytical Modeling of Post-Buckled Precompressed (PBP) Piezoelectric Actuators for UAV Flight Control," *proceedings of the 47th AIAA/ASME/ASCE/AHS/ASC Structures, Structural Dynamics and Materials Conference 14th AIAA/ASME/AHS Adaptive Structures Conference, Newport, RI, May 1-4*, 2006, pp. AIAA-2006-1795.

20. Van Schravendijk, M., Groen, M., Vos, R., and Barrett, R. "Closed Loop Control for High Bandwidth, High Curcature Post-Buckled Precompressed Actuators," *50th AIAA/ASME/ASCE/AHS/ASC Structures, Structural Dynamics, and Materials Conference 17th AIAA/ASME/AHS Adaptive Structures Conference 11th AIAA No, Palm Springs, California, May 4 - 7*, 2009, pp. AIAA-2009-2113.

21. Crawley, E., Lazarus, K., and Warkentin, D. "Embedded Actuation and Processing in Intelligent Materials," *presented at the 2nd International Workshop on Composite Materials and Structures for Rotorcraft, Troy, NY, Sept.*, 1989.

22. Lazarus, K., and Crawley, E. "Multivariable Active Lifting Surface using Strain Actuation: Analytical and Experimental Results," *paper presented at the Third International Conference on Adaptive Structures, sponsored by the ASME, San Diego, CA, 9 - 11 November*, 1992.

23. Lazarus, K., Crawley, E., and Bohlmann, J. D. "Static Aerolastic Control Using Strain Actuated Adaptive Structures," *Proceedings of the First Joint U.S.7/Japan Conference on Adaptive Strucures, Maui, Hawaii, October*, 1990.

24. Spangler, R. L., and Hall, S. R. "Piezoelectric Actuators for Helicopter Rotor Control," *31st Structures, Structural Dynamics and Materials Conference, Long Beach, CA, April*, 1990.

25. Barrett, R. "Intelligent Rotor Blade Actuation through Directionally Attached Piezoelectric Crystals," *46th AHS National Conference and Forum, Washington, D.C., May*, 1990.

26. Barrett, R. "Intelligent Rotor Blade and Structures Development using Piezoelectric Crystals," *MS Thesis, the UM, College Park, Maryland*, 1990.

27. Barrett, R. "Actuation Strain Decoupling Through Enhanced Directional Attachment in Plates and Aerodynamic Surfaces," *Proceedings of the First European Conference on Smart Structures and Materials, Glasgow Scotland, 12-14 May 1992, IOP Publishing, Bristol, UK 1992, 383 - 386*, 1992.

28. Barrett, R. "Method and Apparatus for Sensing and Actuating in a Desired Direction," *US Pat. 5,440,193, Aug.*, 1995.

29. Ehlers, S. M., and Weisshaar, T. A. "Adaptive Wing Flexural Axis Control," *paper presented at the Third International Conference on Adaptive Structures, sponsored by the ASME, San Diego, CA, 9 - 11 November*, 1992.

30. Ehlers, S. M., and Weisshaar, T. A. "Effects of Material Properties on Static Aerolastic Control," *paper presented at the 33rd Structures, Structural Dynamics and Materials, Dallas, TX, 15th April*, 1992.

31. Ehlers, S. M., and Weisshaar, T. A. "Static Aeroelastic Behavior of an Adaptive Laminated Piezoelectric Composite Wing," *AIAA-90-10f8-CP*, 1990, pp. 1611-1623.

32. Barrett, R. "Active Plate and Missile Wing Development Using DAP Elements," *AIAA Journal* Vol. March, 1994.

33. Barrett, R. "Active Plate Missile Development Using EDAP Elements," *Journal of Smart Materials and Structures* Vol. 1, No. 3, p. 214226.

34. Barrett, R. "Active Composite Torque-Plate Fins for Subsonic Missiles," *paper presented at the Dynamic Response of Composite Structures Conference, New Orleans, Louisiana, August 20 - September 1*, 1993.

35. Barrett, R. "Advanced low-Cost Smart Missile Fin Technology Evaluation," *Report to the USAF Armament Directorate, Eglin Air Force Base, FL, Contract No. F0 8620-93-C-0039, BAT, Nov*, 1993.

36. Barrett, R., Brozoski, F., and Gross, R. S. "Design and Testing of a Subsonic All-Moving Adaptive Flight Control Surface," *AIAA Journal* Vol. 35, No. 7, 1997, pp. 1217 - 1219.

37. Barrett, R., and Brozoski, F. "Missile Flight Control using Active Flexspar Actuators," *Journal of Smart Materials and Structures* Vol. 5, No. 2, 1996, pp. 121 - 128.

38. Barrett, R. "Active Aeroelastic Tailoring of an Adaptive Flexspar Stabilator " *Journal of Smart Materials and Structures* Vol. 5, No. 6, 1996, pp. 723 - 730.

39. Barrett, R. "Invention and Evaluation of the Barrel Launched Adaptive Munition (BLAM)," *final report for USAF contract no. F-49620-93-C-0063, USAF Wright Laboratory Flight Vehicles Branch, WLFMNAV August*, 1995.

40. Barrett, R. "High Bandwith Electric Rotor Blade Actuator Study," *Phase I SBIR proposal, Submitted to the U.S. Army Aviation System Command, St. Louis, MO, 27th June*, 1992.

41. Barrett, R., and Stutts, J. "Design and Testing of a 1/12th Scale Solid State Adaptive Rotor," *Journal of Smart Materials and Structures* Vol. 6, No. 4, 1997, pp. 686 - 695.

42. Barrett, R., Frye, P., and Schliesman, M. "Design, Constructionand Characterization of a Flightworty Piezoelectric Solid State Adaptive Rotor," *Journal of Smart Materials and Structures* Vol. 7, No. 3, 1998, pp. 422 - 431.

43. Bartley-Cho, J. D., Wang, D. P., Martin, C. A., Kudva, J. N., and West, M. N. "Development of high-rate, adaptive trailing edge control surface for the Smart Wing Phase 2 wind tunnel model," *Journal of Intelligent Material Systems and Structures* Vol. 15, No. 4, 2004, pp. 279-291.

44. Vos, R., Barrett, R. M., van Tooren, M. J. L., and Krakers, L. M. "Post-Buckled Precompressed (PBP) piezoelectric actuators for UAV flight control."

45. Vos, R., De Breuker, R., Barrett, R., and Tisco, P. "Post-Buckled Precompressed (PBP) Actuators: Enhancing VTOL Autonomous High Speed MAVs," *Proceedings of the 46th AIAA/ASME/ASCE/AHS/ASC Structures, Structural Dynamics and Materials Conference, Austin, Texas, Apr. 18-21*, 2005, pp. AIAA paper no. AIAA-2005-2113.

46. Vos, R., and Barrett, R. "Post-Buckled Precompressed Techniques in Adaptive Aerostructures: An Overview," *ASME 2008 Conference on Smart Materials, Adaptive Structures and Intelligent Systems - October 28-30, 2008, Ellicot City, MD, USA*, 2008.

47. Vos, R., and Barrett, R. "Dynamic Elastic Axis Shifting: An Important Enhancement of Postbuckled Precompressed (PBP) Actuators," *proceedings of the 48th AIAA/ASME/ASCE/AHS/ASC Structures, Structural Dynamics and Materials Conference, 15th AIAA/ASME/AHS Adaptive Structures Conference, Honolulu, Hawaii, 23 April*, 2007, pp. paper no. AIAA-2007-1705.

48. Barrett, R., Vos, R., and De Breuker, R. "Post-Buckled Precompressed (PBP) Subsonic Micro Flight Control Actuatos and Surfaces."

49. Barrett, R., and Vos, R. "Design, Development and Testing of a Transonic Missile Fin Employing PBP/DEAS Actuators," *SPIE Smart Structures/NDE Conference San Diego, 10-13 March 2008*, 2008.

50. Barrett, R., McMurtry, Vos, R., Tisco, P., and De Breuker, R. "Post-buckled precompressed (PBP) elements: a new class of flight control actuators high-speed autonomous VTOL MAVs," *SPIE Smart Structures/NDE Conference San Diego, California 6-10 March 2005*.

51. Hutapea, P., Kim, J., Guion, A., Hanna, C., and Heulitt, N. "Development of a smart wing," *Aircraft Engineering and Aerospace Technology* Vol. 80, No. 4, 2008, pp. 439-444.

52. Epps, J., and Chopra, I. "In-flight tracking of helicopter rotor blades," *Smart Materials and Structures* Vol. 10, 2001, pp. 104-111.

53. Roh, J. H., Kim, K. S., and Lee, I. "Shape Adaptive Airfoil Actuated by a Shape Memory Alloy and its Aerodynamic Characteristics," *Mechanics of Advanced Materials and Structures* Vol. 16, No. 3, 2009, pp. 260-274.

54. Barbarino, S., Pecora, R., Lecce, L., Concilio, A., Ameduri, S., and Calvi, E. "A Novel SMA-based Concept for Airfoil Structural Morphing," *Journal of Materials Engineering and Performance* Vol. 18, No. 5-6, 2009, pp. 696-705.

55. Rediniotis, O. K., Wilson, L. N., Lagoudas, D. C., and Khan, M. M. "Development of a shape-memory-alloy actuated biomimetic hydrofoil," *Journal of Intelligent Material Systems and Structures* Vol. 13, No. 1, 2002, pp. 35-49.

56. Vos, R., and Barrett, R. "Pressure adaptive honeycomb: a new adaptive structure for aerospace applications." Vol. 7647, 2010, p. 76472B.

57. Dynalloy, I. "Flexinol™ Technical Data." 2007.

58. Jones, R. *Mechanics of composite materials*: Hemisphere Pub, 1999.

59. Smith, W. G. "Technical Note: Analytical Solutions For Tapered Column Buckling," *Computers & Structures* Vol. 28, No. 5, 1987, pp. 677-681.

60. Turner, T. L., and Patel, H. D. "Analysis of SMA hybrid composite structures in MSC.Nastran and ABAQUS," *Journal of Intelligent Material Systems and Structures* Vol. 18, No. 5, 2007, pp. 435-447.

61. Gao, X. J., Burton, D., Turner, T. L., and Brinson, L. C. "Finite element analysis of adaptive-stiffening and shape-control SMA hybrid composites," *Journal of Engineering Materials and Technology-Transactions of the Asme* Vol. 128, No. 3, 2006, pp. 285-293.

62. Kim, S., and Cho, M. "Numerical simulation of a double SMA wire actuator using the two-way shape memory effect of SMA," *Smart Materials & Structures* Vol. 16, No. 2, 2007, pp. 372-381.

63. Ladson, C., Brooks, C., Hill Jr, A., and Sproles, D. "Computer program to obtain ordinates for NACA airfoils," *NASA Technical Memorandum* Vol. 4741, 1996, pp. 1-22.

64. Merziger, G., and Wirth, T. *Repetitorium der höheren Mathematik*: Binomi, 1997.

65. Micro-Measurements, V. "Application Note VMM-19: Surface Preparation of Composites," 2005.

66. Dally, J., and Riley, W. "Experimental Stress Analysis," *McGraw-Hill Book Co., 1978*, 1978, p. 571.

67. RATINGS, M., and TRANSISTORS, P. "SEMICONDUCTOR TECHNICAL DATA," *Pulse* Vol. 1, 1996, p. 50.

68. Zaloga, S., and Palmer, I. *Unmanned Aerial Vehicles: Robotic Air Warfare 1917-2007*: Osprey Publishing, 2008.

69. AeroVironment. "Raven RQ-11B Data Sheet (V1.01.09)," 2009.

70. Anderson, J. *Fundamentals of aerodynamics*: McGraw-Hill New York, 1991.

71. Anderson, D., Tannehill, J., and Pletcher, R. *Computational fluid mechanics and heat transfer*: Hemisphere New York, 1984.

Appendix A – Tables

Actuator Design I, Tip Rotation Angle over Applied Axial Force (Chapter 3.1.2.3):

Table 8: Tip Rotation Angle for Applied Axial Buckling Force

	No Act.	Actuation
F_a (N)	δ (deg)	δ (deg)
0.00 N	2.41°	21.97°
0.10 N	5.23°	27.36°
0.20 N	7.75°	30.31°
0.30 N	12.45°	36.14°
0.40 N	12.91°	38.34°
0.50 N	13.94°	41.01°

Actuator Design II, Tip Rotation Angle over Applied Current (Chapter 3.1.2.3):

Table 9: Tip Rotation Angle Values for Glass Fiber Actuators with Various Number of Glass Fiber Layers

1 GF Layer		2 GF Layers		3 GF Layers	
I (A)	δ (deg)	I (A)	δ (deg)	I (A)	δ (deg)
0.00 A	0.00°	0.00 A	0.00°	0.00 A	0.00°
0.05 A	0.00°	0.05 A	0.00°	0.05 A	0.00°
0.10 A	0.00°	0.10 A	0.00°	0.10 A	0.00°
0.15 A	0.00°	0.15 A	0.00°	0.15 A	0.00°
0.20 A	0.00°	0.20 A	0.00°	0.20 A	0.00°
0.25 A	0.00°	0.25 A	0.00°	0.25 A	0.00°
0.30 A	0.00°	0.30 A	0.00°	0.30 A	0.00°
0.35 A	0.19°	0.35 A	0.00°	0.35 A	0.00°
0.40 A	0.57°	0.40 A	0.19°	0.40 A	0.19°
0.45 A	1.15°	0.45 A	0.38°	0.45 A	0.38°
0.50 A	1.91°	0.50 A	0.38°	0.50 A	0.57°
0.55 A	2.68°	0.55 A	0.58°	0.55 A	0.77°
0.60 A	4.01°	0.60 A	0.96°	0.60 A	1.15°
0.65 A	5.73°	0.65 A	1.15°	0.65 A	1.34°
0.70 A	7.84°	0.70 A	1.54°	0.70 A	1.72°
0.75 A	10.36°	0.75 A	2.51°	0.75 A	2.49°
0.80 A	13.48°	0.80 A	4.26°	0.80 A	3.06°
0.85 A	19.74°	0.85 A	6.42°	0.85 A	3.63°
0.90 A	31.92°	0.90 A	10.64°	0.90 A	4.40°
		0.95 A	29.43°	0.95 A	4.97°

Table 10: Tip Rotation Angle Values for Spring Steel Actuators with Variable SMA Wire Diameter

d_{SMA}=0.127 mm		d_{SMA}=0.254 mm		d_{SMA}=0.381 mm	
I (A)	**δ (deg)**	**I (A)**	**δ (deg)**	**I (A)**	**δ (deg)**
0.00 A	0.00°	0.00 A	0.00°	0.00 A	0.00°
0.05 A	0.00°	0.05 A	0.00°	0.10 A	0.00°
0.10 A	0.00°	0.10 A	0.00°	0.20 A	0.00°
0.15 A	0.19°	0.15 A	0.00°	0.30 A	0.00°
0.20 A	0.38°	0.20 A	0.19°	0.40 A	0.00°
0.25 A	0.38°	0.25 A	0.37°	0.50 A	0.00°
0.30 A	0.57°	0.30 A	0.56°	0.60 A	0.19°
0.35 A	1.72°	0.35 A	0.75°	0.70 A	0.38°
0.40 A	3.81°	0.40 A	1.12°	0.80 A	0.57°
0.45 A	6.65°	0.45 A	1.49°	0.90 A	0.76°
0.50 A	10.39°	0.50 A	2.04°	1.00 A	1.33°
0.55 A	14.93°	0.55 A	2.97°	1.10 A	1.71°
0.60 A	18.78°	0.60 A	4.06°	1.20 A	2.67°
		0.65 A	6.59°	1.30 A	4.58°
		0.70 A	9.92°	1.40 A	7.25°
		0.75 A	16.99°	1.50 A	10.09°
		0.80 A	25.21°	1.60 A	17.84°
		0.85 A	35.19°	1.70 A	27.69°

Actuator Design III, Tip Rotation Angle over Applied Current (Chapter 3.4.1):

Table 11: Tip Rotation Angle for Both Sided Actuation

	Front	**Back**
I (A)	**δ (deg)**	**δ (deg)**
0.00 A	0.00°	0.00°
0.05 A	0.19°	-0.19°
0.10 A	0.19°	-0.38°
0.15 A	0.19°	-0.38°
0.20 A	0.57°	-0.75°
0.25 A	0.76°	-1.13°
0.30 A	1.14°	-1.69°
0.35 A	1.89°	-2.99°
0.40 A	3.40°	-5.20°
0.45 A	7.29°	-9.33°
0.50 A	14.20°	-16.10°
0.55 A	24.82°	-26.58°
0.60 A	33.02°	-34.40°
0.65 A	41.18°	-40.54°
0.70 A	46.54°	-44.57°
0.75 A	51.08°	-49.05°
0.80 A	55.11°	-52.84°
0.85 A	58.59°	-55.73°

Table 12: Tip Rotation Angle over Applied Axial Force and Applied Current

	F_a = 0 N	F_a = 1 N	F_a = 2 N	F_a = 3 N	F_a = 4 N	F_a = 5 N
I (A)	**δ (deg)**	**δ (deg)**	**δ (deg)**	**δ (deg)**	**δ (deg)**	**δ (deg)**
0.00 A	4.76°	5.14°	6.09°	6.09°	7.41°	8.90°
0.05 A	4.76°	5.14°	6.09°	6.09°	7.41°	8.90°
0.10 A	4.76°	5.14°	6.28°	6.09°	7.59°	8.90°
0.15 A	4.76°	5.33°	6.47°	6.09°	7.59°	9.09°
0.20 A	4.95°	5.52°	6.65°	6.28°	7.78°	9.28°
0.25 A	5.33°	5.90°	7.22°	6.65°	7.97°	9.83°
0.30 A	5.90°	6.47°	7.59°	7.22°	8.53°	10.39°
0.35 A	7.03°	7.59°	8.90°	7.97°	9.28°	12.04°
0.40 A	9.28°	9.46°	12.04°	10.02°	10.94°	17.40°
0.45 A	14.04°	13.86°	21.80°	19.29°	22.62°	30.26°
0.50 A	21.80°	23.43°	28.81°	31.24°	35.63°	43.03°
0.55 A	31.94°	34.22°	39.24°	40.36°	44.52°	49.80°
0.60 A	40.36°	41.46°	46.40°	47.55°	50.51°	
0.65 A	46.40°	47.73°	51.34°	51.71°	55.28°	
0.70 A	50.19°	51.27°	54.14°	55.10°	59.04°	
0.75 A	52.99°	54.14°	56.89°	58.78°	62.24°	
0.80 A	55.22°	56.31°	59.29°	61.39°	64.89°	
0.85 A	57.45°	58.52°	61.82°	63.24°		

Table 13: Blocked Tip Force over Applied Axial Force and Applied Current

	F_a = 0 N	F_a = 1 N	F_a = 2 N	F_a = 3 N	F_a = 4 N	F_a = 5 N
I (A)	**F_{tip} (N)**	**F_{tip} (N)**	**F_{tip} (N))**	**F_{tip} (N)**	**F_{tip} (N)**	**F_{tip} (N)**
0.00 A	0.000 N	0.000 N	0.000 N	0.000 N	0.000 N	0.000 N
0.05 A	0.000 N	0.000 N	0.000 N	0.000 N	0.000 N	0.000 N
0.10 A	0.001 N	0.002 N	0.002 N	0.002 N	0.002 N	0.001 N
0.15 A	0.004 N	0.005 N	0.006 N	0.005 N	0.005 N	0.004 N
0.20 A	0.009 N	0.011 N	0.012 N	0.009 N	0.010 N	0.009 N
0.25 A	0.015 N	0.019 N	0.019 N	0.015 N	0.016 N	0.015 N
0.30 A	0.025 N	0.027 N	0.030 N	0.024 N	0.025 N	0.026 N
0.35 A	0.037 N	0.041 N	0.044 N	0.037 N	0.037 N	0.037 N
0.40 A	0.054 N	0.058 N	0.065 N	0.053 N	0.056 N	0.054 N
0.45 A	0.085 N	0.088 N	0.091 N	0.080 N	0.080 N	0.080 N
0.50 A	0.122 N	0.124 N	0.129 N	0.119 N	0.120 N	0.120 N
0.55 A	0.165 N	0.169 N	0.177 N	0.162 N	0.166 N	0.159 N
0.60 A	0.215 N	0.214 N	0.215 N	0.207 N	0.207 N	0.200 N
0.65 A	0.253 N	0.256 N	0.260 N	0.251 N	0.250 N	0.243 N
0.70 A	0.296 N	0.297 N	0.297 N	0.291 N	0.291 N	0.280 N
0.75 A	0.339 N	0.337 N	0.338 N	0.331 N	0.330 N	0.320 N
0.80 A	0.380 N	0.381 N	0.377 N	0.373 N	0.371 N	0.363 N
0.85 A	0.417 N	0.416 N	0.422 N	0.410 N	0.414 N	0.401 N

Current Amplifier Performance (Chapter 4.2.3)

Table 14: Current Amplifier Performance

U_{in} (V)	I_{out} (A)
0.00 V	0.00 A
0.25 V	0.00 A
0.50 V	0.00 A
0.75 V	0.00 A
1.00 V	0.00 A
1.25 V	0.03 A
1.50 V	0.07 A
1.75 V	0.13 A
2.00 V	0.18 A
2.25 V	0.24 A
2.50 V	0.31 A
2.75 V	0.37 A
3.00 V	0.43 A
3.25 V	0.51 A
3.50 V	0.59 A
3.75 V	0.60 A
4.00 V	0.60 A
4.25 V	0.60 A
4.50 V	0.60 A
4.75 V	0.60 A
5.00 V	0.60 A

Calibration Curves for position Feedback System (Chapter 4.2.2.1):

Actuator 1:

Table 15: Calibration Values for Front Actuation Actuator 1

Front Actuation			
I (A)	ε_{gage} ()	δ_{exp} (deg)	δ_{approx} (deg)
0.00 A	6.219E-03	0.00°	0.63°
0.05 A	6.221E-03	0.00°	0.35°
0.10 A	6.216E-03	0.00°	1.03°
0.15 A	6.216E-03	0.19°	0.97°
0.20 A	6.220E-03	0.19°	0.41°
0.25 A	6.221E-03	0.19°	0.31°
0.30 A	6.219E-03	0.37°	0.62°
0.35 A	6.209E-03	0.37°	1.88°
0.40 A	6.202E-03	0.56°	2.93°
0.45 A	6.208E-03	0.74°	2.09°
0.50 A	6.194E-03	1.48°	3.87°
0.55 A	6.174E-03	3.30°	6.55°
0.60 A	5.968E-03	33.17°	33.88°
0.65 A	5.929E-03	39.01°	39.11°
0.70 A	5.917E-03	43.82°	40.60°
0.75 A	5.880E-03	48.24°	45.55°

Table 16: Calibration Values for Back Actuation Actuator 1

Back Actuation			
I (A)	ε_{gage} ()	δ_{exp} (deg)	δ_{approx} (deg)
0.05 A	6.222E-03	0.00°	0.28°
0.10 A	6.230E-03	-0.19°	-0.89°
0.15 A	6.222E-03	-0.38°	0.18°
0.20 A	6.243E-03	-0.75°	-2.62°
0.25 A	6.234E-03	-1.32°	-1.36°
0.30 A	6.246E-03	-1.88°	-2.96°
0.35 A	6.264E-03	-3.92°	-5.33°
0.40 A	6.287E-03	-8.28°	-8.46°
0.45 A	6.371E-03	-18.36°	-19.51°
0.50 A	6.500E-03	-33.60°	-36.62°
0.55 A	6.553E-03	-41.33°	-43.61°
0.60 A	6.595E-03	-48.44°	-49.22°
0.65 A	6.617E-03	-52.18°	-52.14°
0.70 A	6.635E-03	-54.87°	-54.47°
0.75 A	6.641E-03	-56.89°	-55.35°

Actuator 2:

Table 17: Calibration Values for Front Actuation Actuator 2

Front Actuation			
I (A)	ε_{gage} ()	δ_{exp} (deg)	δ_{approx} (deg)
0.00 A	6.131E-03	0.00°	-0.22°
0.05 A	6.129E-03	0.00°	-0.05°
0.10 A	6.125E-03	0.19°	0.52°
0.15 A	6.133E-03	0.37°	-0.58°
0.20 A	6.126E-03	0.56°	0.42°
0.25 A	6.128E-03	0.94°	0.14°
0.30 A	6.126E-03	1.50°	0.39°
0.35 A	6.103E-03	2.79°	3.54°
0.40 A	6.093E-03	4.63°	4.85°
0.45 A	6.053E-03	8.75°	10.22°
0.50 A	6.017E-03	13.88°	14.98°
0.55 A	5.950E-03	20.77°	24.06°
0.60 A	5.943E-03	26.75°	24.98°
0.65 A	5.900E-03	31.64°	30.67°
0.70 A	5.871E-03	35.43°	34.54°
0.75 A	5.841E-03	38.80°	38.55°

Table 18: Calibration Values for Back Actuation Actuator 2

Back Actuation			
I (A)	ε_{gage} ()	δ_{exp} (deg)	δ_{approx} (deg)
0.00 A	6.131E-03	0.00°	-0.22°
0.05 A	6.133E-03	0.00°	-0.51°
0.10 A	6.135E-03	-0.29°	-0.79°
0.15 A	6.130E-03	0.08°	-0.12°
0.20 A	6.140E-03	-1.95°	-1.46°
0.25 A	6.138E-03	-2.32°	-1.19°
0.30 A	6.142E-03	-6.58°	-1.73°
0.35 A	6.163E-03	-4.23°	-4.54°
0.40 A	6.180E-03	-6.51°	-6.82°
0.45 A	6.200E-03	-8.14°	-9.50°
0.50 A	6.242E-03	-14.02°	-15.13°
0.55 A	6.350E-03	-29.66°	-29.61°
0.60 A	6.364E-03	-33.73°	-31.49°
0.65 A	6.410E-03	-36.32°	-37.65°
0.70 A	6.440E-03	-42.74°	-41.67°
0.75 A	6.470E-03	-45.99°	-45.70°

Lift Coefficients C_L (Chapter 4.3.4):

Table 19: Lift Coefficients for different Actuator Tip Rotation Angles

	α = 0°	**α = 2°**	**α = 4°**	**α = 6°**	**α = 8°**	**α = 10°**
δ=0°	0.000	0.036	0.071	0.106	0.141	0.175
δ=5°	0.037	0.072	0.108	0.143	0.177	0.211
δ=10°	0.074	0.109	0.144	0.178	0.212	0.246
δ=15°	0.109	0.144	0.179	0.213	0.246	0.279
δ=20°	0.144	0.179	0.213	0.246	0.279	0.310
δ=25°	0.177	0.211	0.245	0.277	0.309	0.339
δ=30°	0.209	0.242	0.275	0.306	0.337	0.365

Drag Coefficients C_D (Chapter 4.3.4):

Table 20: Drag Coefficients for different Actuator Tip Rotation Angles

	α = 0°	**α = 2°**	**α = 4°**	**α = 6°**	**α = 8°**	**α = 10°**
δ=0°	4.11E-05	6.68E-05	1.48E-04	2.76E-04	4.76E-04	7.25E-04
δ=5°	6.47E-05	1.39E-04	2.71E-04	4.46E-04	6.98E-04	9.90E-04
δ=10°	1.34E-04	2.57E-04	4.36E-04	6.61E-04	9.66E-04	1.31E-03
δ=15°	2.78E-04	4.50E-04	6.84E-04	9.61E-04	1.32E-03	1.71E-03
δ=20°	4.36E-04	6.55E-04	9.44E-04	1.27E-03	1.68E-03	2.13E-03
δ=25°	6.77E-04	9.50E-04	1.29E-03	1.66E-03	2.13E-03	2.62E-03
δ=30°	1.00E-03	1.33E-03	1.73E-03	2.15E-03	2.67E-03	3.21E-03

Forces on Flap (Chapter 4.3.5):

Table 21: Force on Flap Region for Various Angles of Attack α and Actuator Tip Rotation Angles δ

	δ=0°	**δ=5°**	**δ=10°**	**δ=20°**	**δ=30°**	**δ=40°**	**δ=50°**
α=0°	0.00 N	0.22 N	0.46 N	0.61 N	0.77 N	0.88 N	1.05 N
α=2°	0.31 N	0.40 N	0.61 N	0.71 N	0.86 N	0.95 N	1.11 N
α=4°	0.58 N	0.55 N	0.72 N	0.80 N	0.95 N	1.00 N	1.16 N
α=6°	0.80 N	0.67 N	0.82 N	0.87 N	0.99 N	1.04 N	1.18 N
α=8°	0.99 N	0.77 N	0.90 N	0.93 N	1.03 N	1.07 N	1.20 N
α=10°	1.15 N	0.85 N	0.97 N	0.97 N	1.06 N	1.08 N	1.20 N

Wind Tunnel Test – Lift Coefficient (Chapter 4.4.2):

Table 22: Lift Coefficients Obtained by Wind Tunnel Tests

	α=0°	α=2°	α=6°	α=10°
δ=0°	0.070	0.185	0.276	0.299
δ=10°	0.160	0.306	0.399	0.391
δ=20°	0.242	0.369	0.478	0.427
δ=30°	0.259	0.453	0.564	0.597

Wind Tunnel Test – Drag Coefficient (Chapter 4.4.2):

Table 23: Drag Coefficients Obtained by Wind Tunnel Tests

	α=0°	α=2°	α=6°	α=10°
δ=0°	0.118	0.139	0.157	0.143
δ=10°	0.131	0.147	0.173	0.155
δ=20°	0.142	0.158	0.144	0.167
δ=30°	0.147	0.168	0.173	0.181

Appendix B – Figures

Pressure Coefficient Distribution (Chapter 4.3.5):

Actuator Tip Rotation Angle δ=0°:

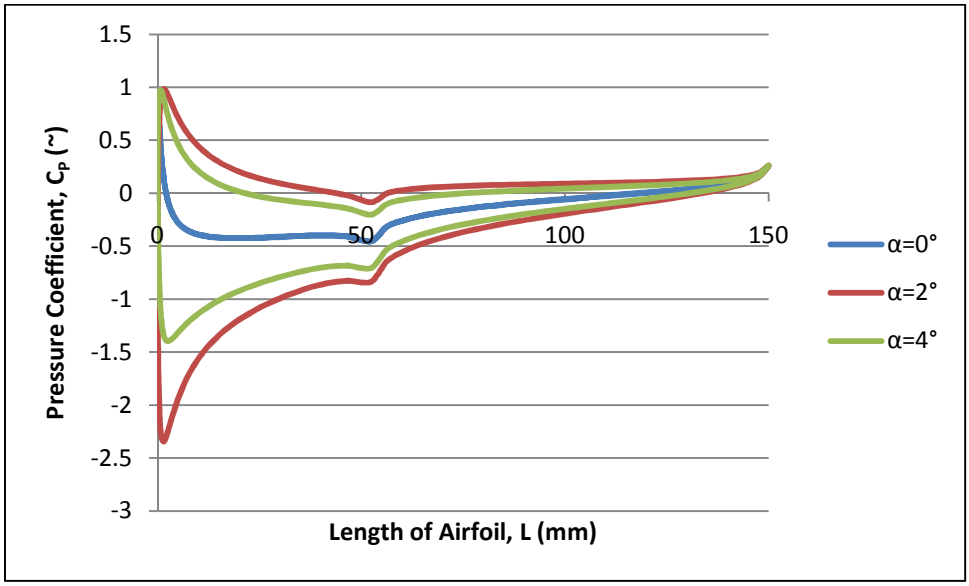

Figure 97: Pressure Coefficient Distribution over Airfoil at δ=0° for α=0°, α=2° & α=4°

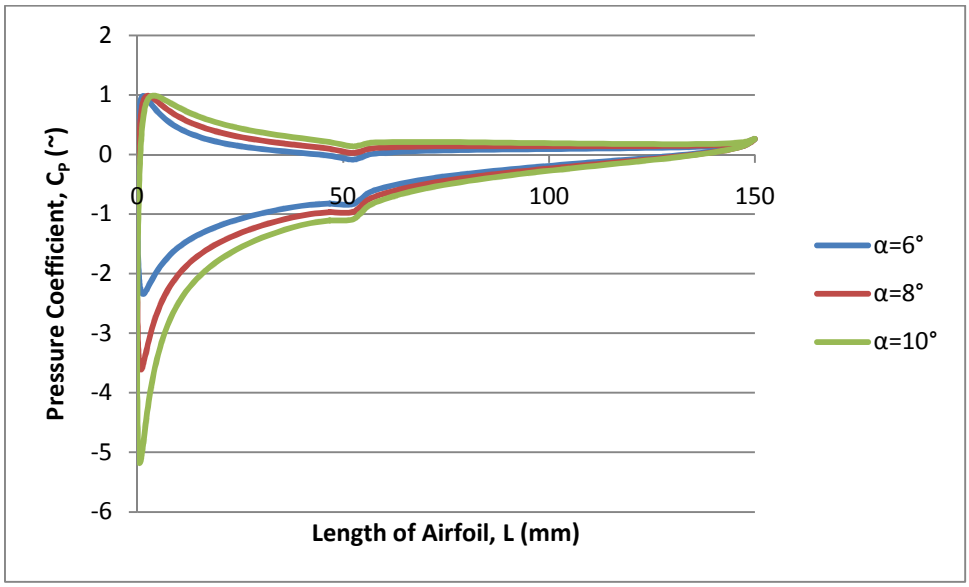

Figure 98: Pressure Coefficient Distribution over Airfoil at δ=0° for α=6°, α=8° & α=10°

Actuator Tip Rotation Angle δ=5°:

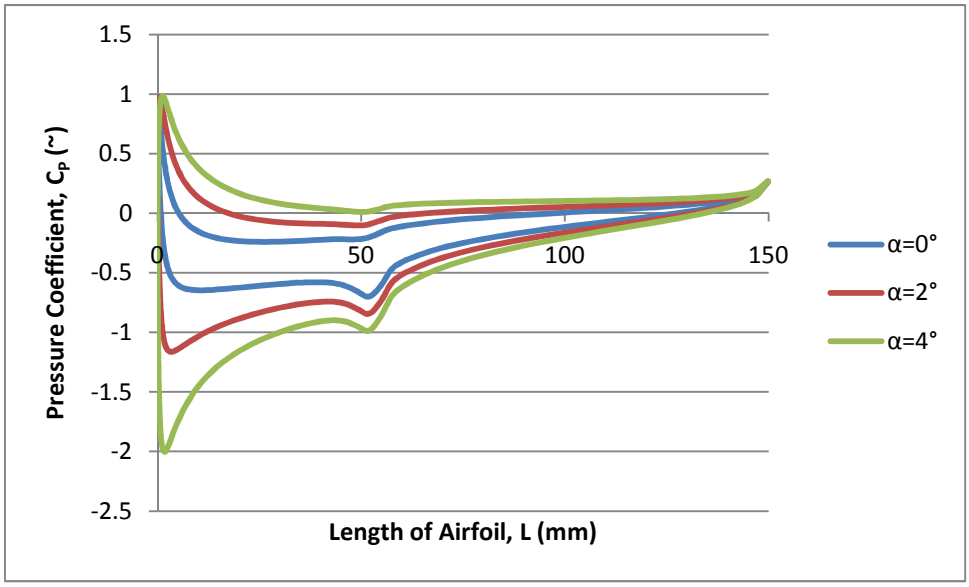

Figure 99: Pressure Coefficient Distribution over Airfoil at δ=5° for α=0°, α=2° & α=4°

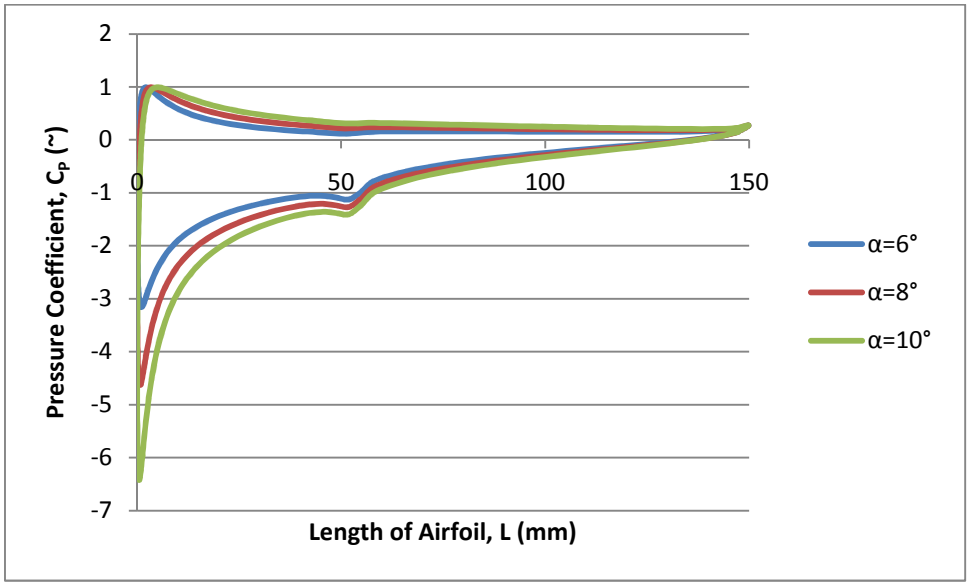

Figure 100: Pressure Coefficient Distribution over Airfoil at δ=5° for α=6°, α=8° & α=10°

Actuator Tip Rotation Angle δ=10°:

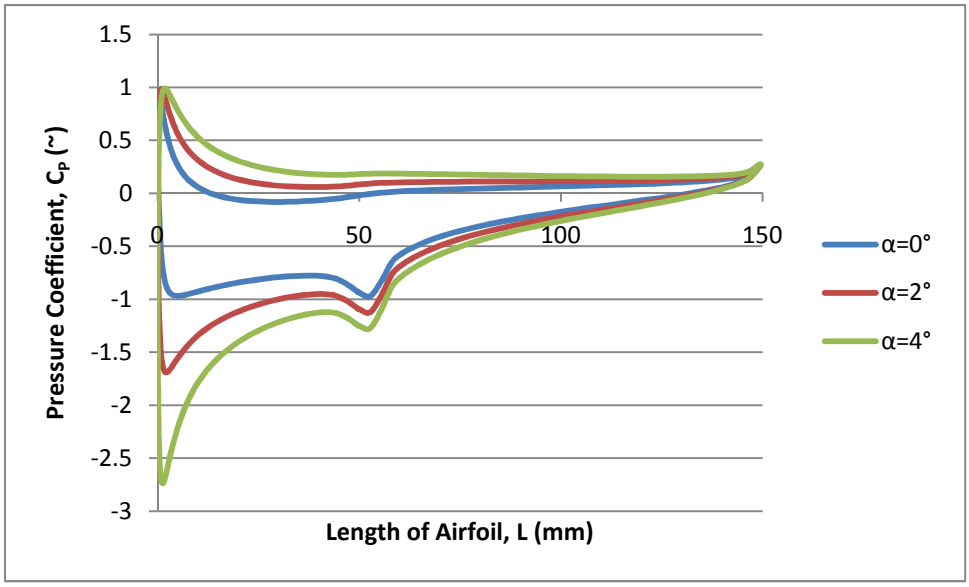

Figure 101: Pressure Coefficient Distribution over Airfoil at δ=10° for α=0°, α=2° & α=4°

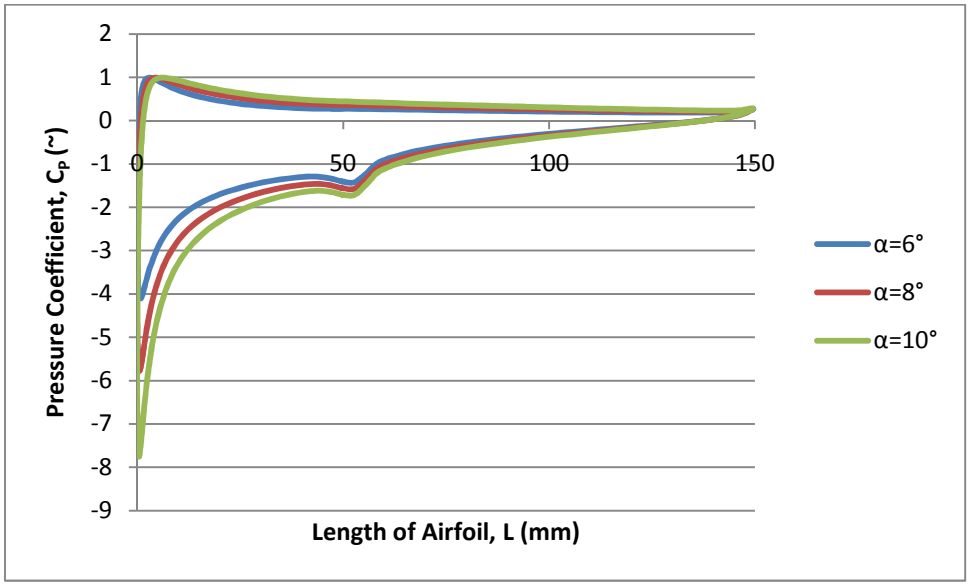

Figure 102: Pressure Coefficient Distribution over Airfoil at δ=10° for α=6°, α=8° & α=10°

Actuator Tip Rotation Angle δ=15°:

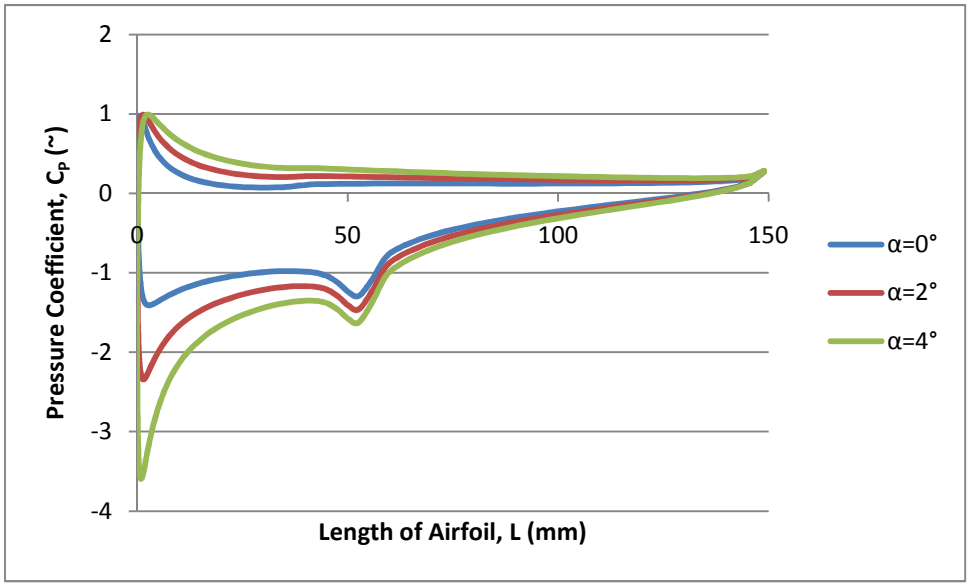

Figure 103: Pressure Coefficient Distribution over Airfoil at δ=15° for α=0°, α=2° & α=4°

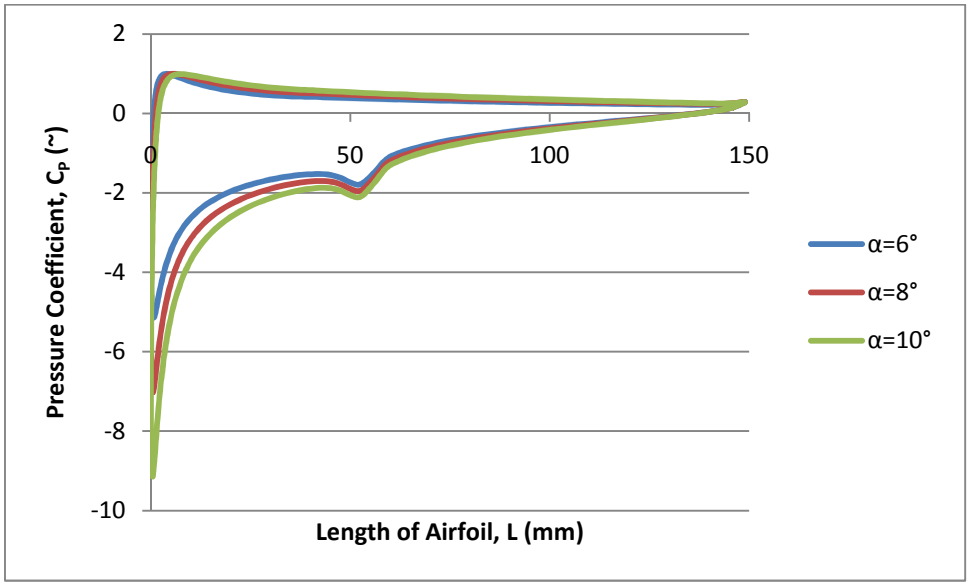

Figure 104: Pressure Coefficient Distribution over Airfoil at δ=15° for α=6°, α=8° & α=10°

Actuator Tip Rotation Angle δ=20°:

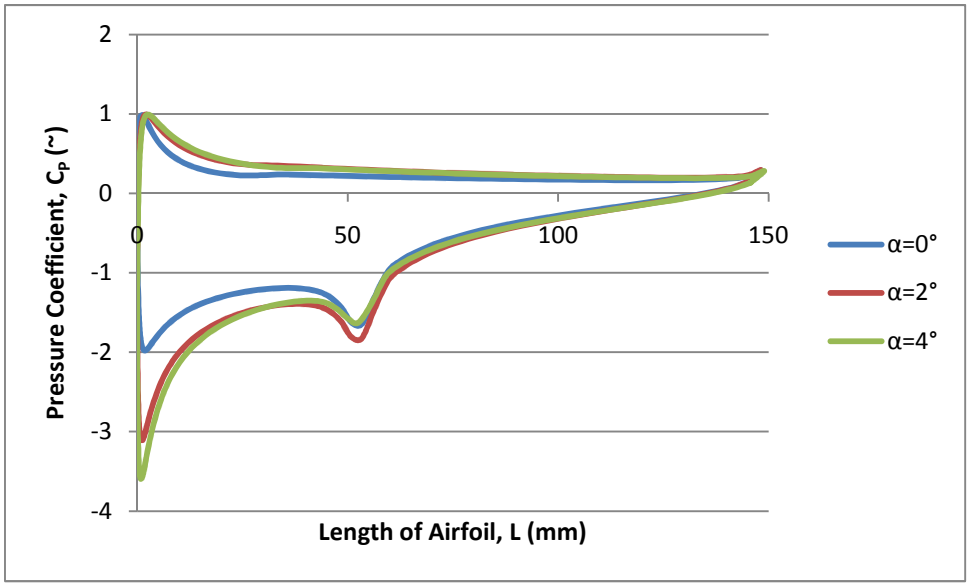

Figure 105: Pressure Coefficient Distribution over Airfoil at δ=20° for α=0°, α=2° & α=4°

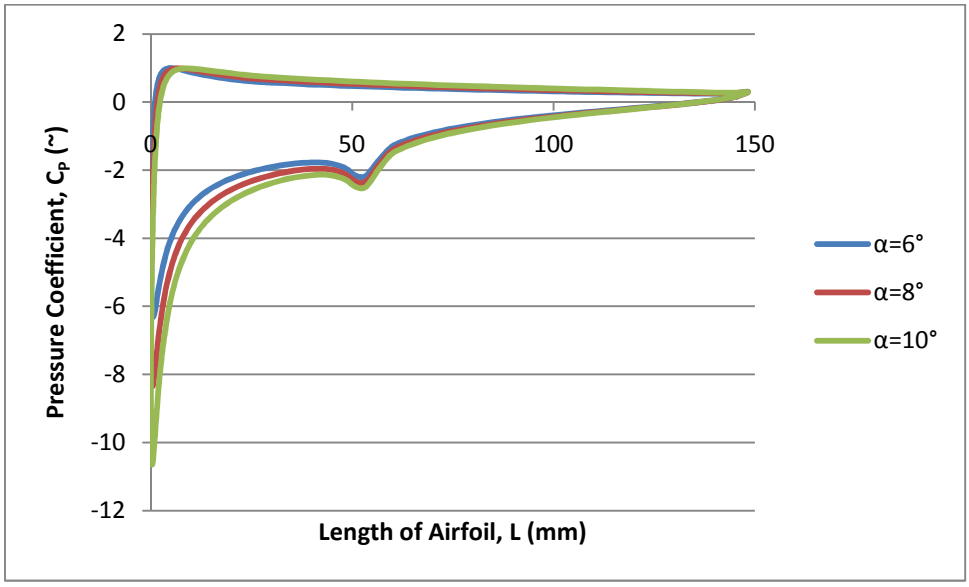

Figure 106: Pressure Coefficient Distribution over Airfoil at δ=20° for α=6°, α=8° & α=10°

Actuator Tip Rotation Angle δ=25°:

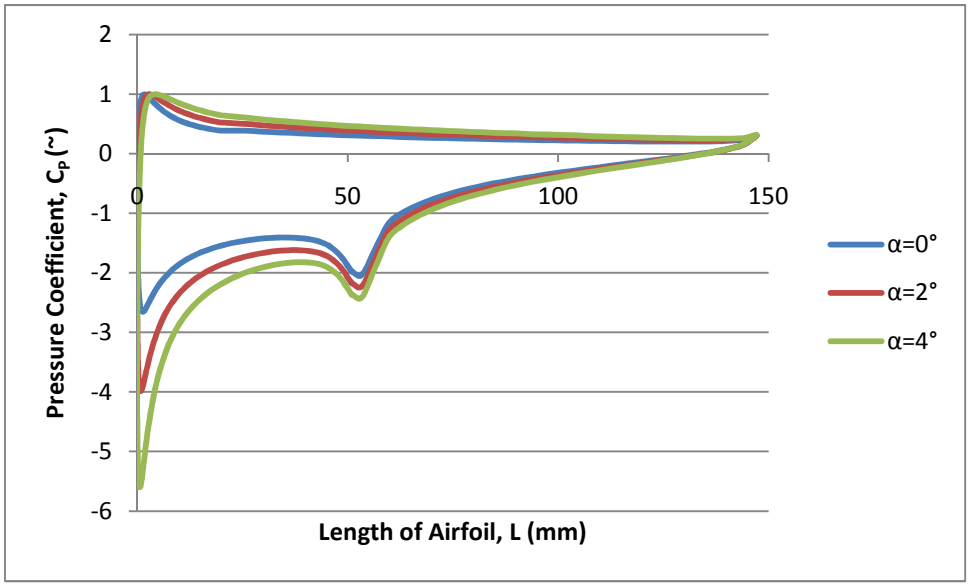

Figure 107: Pressure Coefficient Distribution over Airfoil at δ=25° for α=0°, α=2° & α=4°

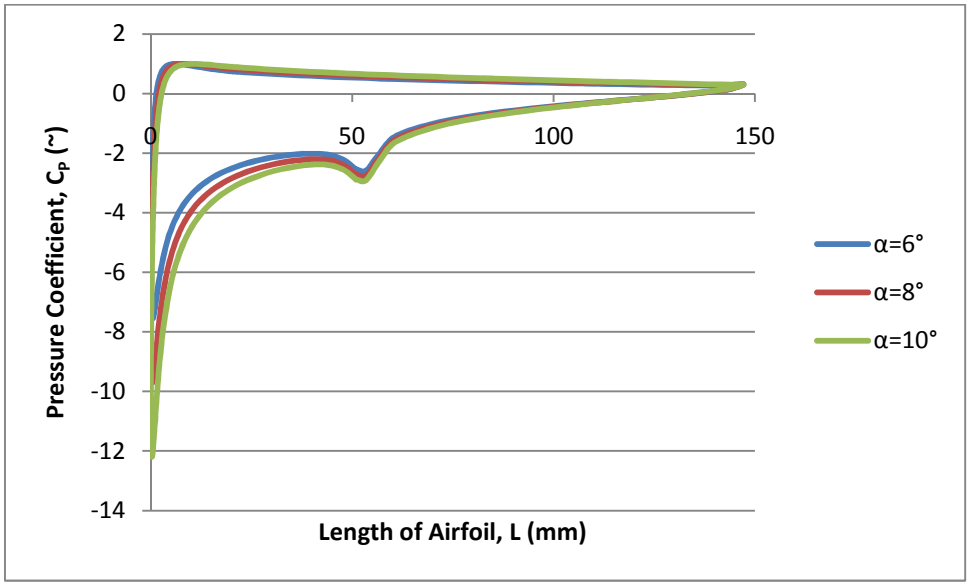

Figure 108: Pressure Coefficient Distribution over Airfoil at δ=25° for α=6°, α=8° & α=10°

Actuator Tip Rotation Angle δ=30°:

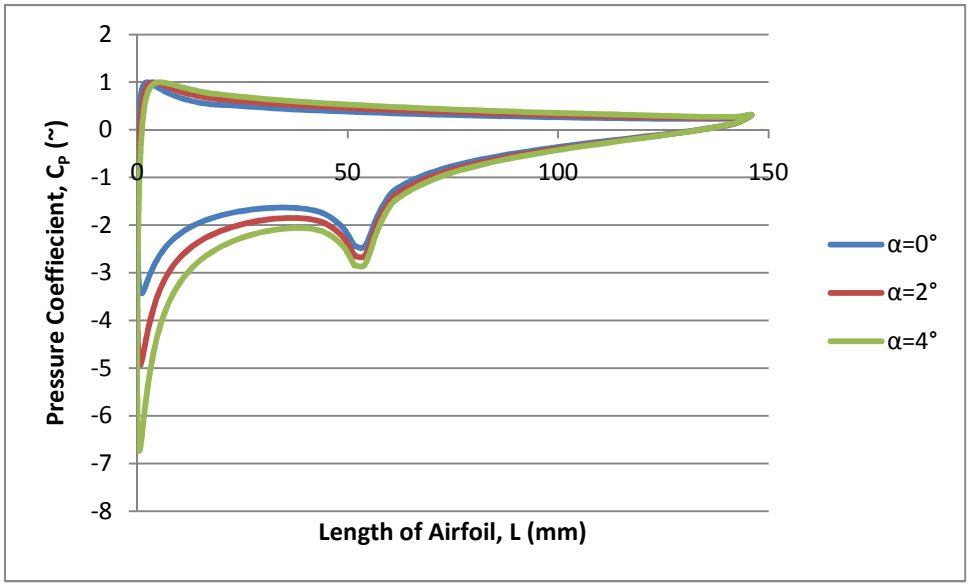

Figure 109: Pressure Coefficient Distribution over Airfoil at δ=30° for α=0°, α=2° & α=4°

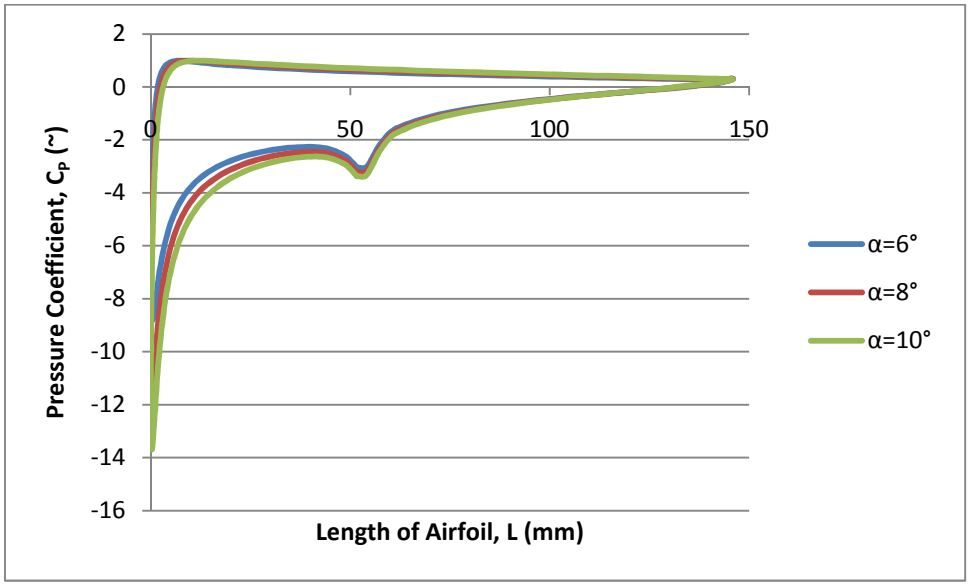

Figure 110: Pressure Coefficient Distribution over Airfoil at δ=30° for α=6°, α=8° & α=10°